Mohamed Boudiaf University - M'sila

FACULTY OF SCIENCES

PHYSICS DEPARTEMENT

Order N°:

Thesis

To obtain the degree of

DOCTORATE 3rd cycle

Field: Physics

Option: Physics of materials

Presented by:

AMARI Fouzi

Theme

First principles study of the fundamental properties of transition metal Selenides

At **12/02/2026** with the board of examiners:

BAADJI Nadjib	Professor	M'sila university	President
SAIB Salima	Professor	M'sila university	Supervisor
FERAHTIA Samia	Professor	M'sila university	Examiner
GUEDDIM Ahmed	Professor	Djelfa university	Examiner
BOUSSENDEL Abdelmadjid	MCA	M'sila university	Examiner

Academic year: 2025/2026

Acknowledgements

First and foremost, thanks to Allah who gives me the power to move forward in a path illuminated by His merciful guidance.

We would like to express our sincere gratitude to our supervisor, Professor **SAIB Salima**, for the attention she devoted to us, the research framework she provided, as well as her rigorous methodology and invaluable guidance.

I warmly thank Professor **BAADJI Nadjib** from the University of M'sila, who did me the honor of presiding over my jury.

I also want to sincerely thank Professor **FERAHTIA Samia** from the University of M'sila, Professor **GUEDDIM Ahmed** from the University of Djelfa, and Dr. **BOUSSENDEL Abd Elmadjid** from the University of M'sila for kindly agreeing to review my work. Their valuable time, careful evaluation, and constructive feedback are greatly appreciated.

My heartfelt thanks go to my family, colleagues, and friends for their constant support, presence, and encouragement throughout this work. Finally, I express my gratitude to all those who, in one way or another, contributed to the completion of this thesis.

Dedications

I dedicate this work to:

To my father, who suffered greatly for us so that our lives may be better.

Thank you, my Father!

To my mother, who gave so much and sacrificed greatly for me to reach the good part.

Thank you, my Mother!

To all my family, brothers, sisters, and friends.

Contents

Chapter III: Results and discussion

List of Figures

List of Tables

General Introduction

Physical modelling through numerical simulation is becoming an increasingly important tool in scientific disciplines, including solid-state physics and molecular chemistry, because of its exceptional success in describing and predicting material properties. The advent of high-performance computing and advanced processors has enabled the implementation of highly sophisticated computational methods, allowing researchers to reproduce and interpret experimental observations with ever-greater accuracy. These developments have transformed computational modelling into a fundamental complement to experimental techniques, providing valuable insights into the microscopic mechanisms governing material behavior and facilitating the design of new materials with tailored properties.

Among the various computational approaches, Density Functional Theory (DFT) has emerged as one of the most powerful and widely used methods for investigating the structural, electronic, and mechanical properties of materials at the atomic scale. Based on the fundamental principles of quantum mechanics, DFT provides an efficient framework for solving the many-body problem of interacting electrons by expressing the total energy of a system as a functional of its electron density. Its balance between accuracy and computational efficiency has made it an indispensable tool in modern materials science. In particular, DFT enables the prediction of a wide range of physical properties such as lattice parameters, band structures, elastic constants, and thermodynamic behavior with remarkable precision.

Transition metal selenides (TMSe) represent an important class of materials that have been extensively studied because of their intriguing physical properties and wide range of technological applications. These compounds exhibit a unique combination of structural flexibility, electronic tunability, and chemical stability, which make them attractive for applications in optoelectronics, spintronic, photovoltaics, thermoelectric devices, and magnetic storage technologies [1–11]. In particular, the II–VI and transition metal selenides, such as cadmium selenide (CdSe), mercury selenide (HgSe), scandium selenide (ScSe), and manganese selenide (MnSe), have received significant attention owing to their diverse electronic and structural characteristics.

CdSe and HgSe are typical II–VI semiconductors that have been widely utilized in optical and electronic devices because of their tunable direct band gaps, high optical absorption, and excellent luminescent properties. Cadmium selenide (CdSe), in particular, has attracted significant attention in both fundamental research and technological applications. Due to its infrared radiation transparency, CdSe has found specialized use in infrared windows [12–16].

Moreover, its tunable morphology and size at the nanoscale have expanded its range of applications to include bio imaging, photovoltaics, lasers, transistors, LEDs, and catalysis [17]. Interestingly, CdSe also serves as a promising thin-film material for detectors, lasers, optoelectronic devices, and photo electrochemical cells [18] and is regarded as a leading candidate for room-temperature nuclear radiation detectors [19]. High-quality CdSe single crystals are commonly produced using vapor phase methods, such as vertical unseeded vapor growth or the horizontal Bridgman technique [19]. The optical, thermodynamic, structural, electrical, and compositional characteristics of CdSe in bulk and thin-film forms have been the subject of several investigations [20–29]. Another significant member of the II–VI semiconductor family is mercury selenide (HgSe). That show intricate pressure-induced phase transitions, narrow-gap semiconducting properties, and relativistic effects in a rich interplay. Because of their particular band structures, topological properties, and quantum phase behavior, these materials are gaining attention as viable options for use in thermoelectrics, spintronics, infrared optoelectronics, and topological insulator devices [1–3,6].

MnSe and ScSe represent another category of transition metal selenides that display complex magnetic and electronic behavior. Rare-earth compounds are a subject of intense research focus, driven by the highly interactive and strongly correlated nature of their f-electrons. This interaction makes their physical and chemical properties exceptionally responsive to external parameters such as pressure and temperature [30–33]. These materials exhibit remarkable magnetic, optical, and electronic characteristics, enabling their integration into diverse applications, including optical glasses, magneto-optical devices, and advanced electronic components [34–40], Among these materials, Scandium monochalcogenides (ScS, ScSe, ScTe) are a key class of materials within this family, prized not only for their fundamental scientific interest but also for their promising technological applications. Owing to their high melting point and excellent thermal stability, these compounds are widely investigated for use in electronic devices, laser systems, non-linear optics, and various industrial processes [41–43]. Moreover, manganese selenide (MnSe) is a transition metal chalcogenide that has garnered significant interest because of its distinctive magnetic, electronic, and structural characteristics [44,45]. As magnetic semiconductors, manganese-based chalcogenides stand out for their intrinsic magnetism and variety of optical functions. These developments offer significant potential benefits for solar cells, spintronic devices, and infrared detectors [5,46].

A detailed understanding of the structural, electronic, optical, elastic, dynamical, and thermodynamic properties of these materials under varying external conditions (pressures and

temperatures) is essential for their potential technological implementation. This work is organized into three chapters. In the first chapter, we will discuss the general concepts of transition metal selenides, focusing on cadmium selenides (CdSe), mercury selenides (HgSe), scandium selenides (ScSe) and manganese selenides (MnSe) and some of their applications. The second chapter will present the theoretical framework of ab initio calculations in which this work will be carried out. We will recall the development of electronic structure calculation methods and explain the foundations of DFT. We will also remember the approximations used to treat the energy-exchange and correlation part, and present other approximations related to pseudopotentials and flat-wave development. Next, we will describe the CASTEP calculation codes [47] used in this work, with the input parameters of the code used to simulate. In the third chapter, it seems natural that in a work of this kind, we end up with the study of concrete cases, the different results obtained from our ab initio calculations of the structural, optical, electronic and mechanical properties, and thermal dynamics of the CdSe and MnSe in both zinc-blende (B3) and rock-salt (B1) structures, HgSe in both zinc-blende (B3) and cinnabar phases (B9) and ScSe in both NaCl type (B1) and CsCl type (B2) structures at zero and under applied pressures, their interpretations and comparisons to theoretical and experimental work. The conclusion will outline this study's principal findings.

References

[1] K.-U. Gawlik, L. Kipp, M. Skibowski, N. Orłowski, and R. Manzke, Phys. Rev. Lett. **78**, 3165 (1997).

[2] A. N. Chantis, M. Van Schilfgaarde, and T. Kotani, Phys. Rev. Lett. **96**, 086405 (2006).

[3] F. Virot, R. Hayn, M. Richter, and J. Van Den Brink, Phys. Rev. Lett. **111**, 146803 (2013).

[4] S. Palchoudhury, K. Ramasamy, J. Han, P. Chen, and A. Gupta, Nanoscale Adv. **5**, 2724 (2023).

[5] K. Ozawa, S. Anzai, and Y. Hamaguchi, Phys. Lett. **20**, 132 (1966).

[6] Y. Selmani, H. Labrim, A. Jabar, and L. Bahmad, Int. J. Mod. Phys. B **38**, 2450334 (2024).

[7] S. Ferahtia, S. Saib, N. Bouarissa, and S. Benyettou, Superlattices Microstruct. **67**, 88 (2014).

[8] S. Mnasri, S. Abdi-Ben Nasrallah, N. Sfina, N. Bouarissa, and M. Said, Semicond. Sci. Technol. **24**, 095008 (2009).

[9] W. Zhou, S. Wu, and S. Li, J. Magn. Magn. Mater. **395**, 166 (2015).

[10] O. Kavcı and S. Cabuk, Comput. Mater. Sci. **95**, 99 (2014).

[11] Adachi S., *Properties of Group-IV, III-V and II-VI Semiconductors*, Wiley (2005).

[12] *CRC Handbook of Chemistry and Physics, 92nd Edition*, Vol. 4(1) (CRC Press, 2011).

[13] H. Zhang, B. Hu, L. Sun, R. Hovden, F. W. Wise, D. A. Muller, and R. D. Robinson, Nano Lett. **11**, 5356 (2011).

[14] R. C. Somers, M. G. Bawendi, and D. G. Nocera, Chem. Soc. Rev. **36**, 579 (2007).

[15] N. C. Anderson and J. S. Owen, Chem. Mater. **25**, 69 (2013).

[16] A. K. Nayak and N. K. Sahu, editors , *Nanostructured Materials for Visible Light Photocatalysis* (Elsevier, Amsterdam, Netherlands Oxford, United Kingdom Cambridge, MA, 2022).

[17] S. J. Dhoble, A. Nande, N. T. Kalyani, A. Tiwari, and A. K. Arof, editors , *Functional Materials from Carbon, Inorganic, and Organic Sources: Methods and Advances* (Woodhead Publishing, Cambridge, MA Kidlington, 2023).

[18] A. S. Khomane and P. P. Hankare, J. Alloys Compd. **489**, 605 (2010).

[19] M. Roth, Nucl. Instrum. Methods Phys. Res. Sect. Accel. Spectrometers Detect. Assoc. Equip. **283**, 291 (1989).

[20] H. H. Gürel and H. Ünlü, Mater. Sci. Semicond. Process. **16**, 1619 (2013).

[21] A. Burger, D. O. Henderson, S. H. Morgan, and E. Silberman, J. Cryst. Growth **109**, 304 (1991).

[22] S. Zhu, B. Zhao, Y. Jin, W. Yang, X. Chen, and Y. Den, J. Cryst. Growth **240**, 454 (2002).

[23] T. Zeng, B. Zhao, S. Zhu, Z. He, B. Chen, and Z. Tan, J. Cryst. Growth **316**, 15 (2011).

[24] H. M. Kotb, M. A. Dabban, A. Y. Abdel-latif, and M. M. Hafiz, J. Alloys Compd. **512**, 115 (2012).

[25] A. V. Kokate, U. B. Suryavanshi, and C. H. Bhosale, Sol. Energy **80**, 156 (2006).

[26] V. Swaminathan, V. Subramanian, and K. R. Murali, Thin Solid Films **359**, 113 (2000).

[27] O. Yamamoto, T. Sasamoto, and M. Inagaki, J. Mater. Res. **13**, 3394 (1998).

[28] I. Un Nabi Lone, S. S. M. Mohamed, I. B. Shameem Banu, and S. Sathik Basha, Mater. Chem. Phys. **192**, 291 (2017).

[29] B. Su and K. L. Choy, Thin Solid Films **361–362**, 102 (2000).

[30] G. Vaitheeswaran, V. Kanchana, and M. Rajagopalan, Phys. B Condens. Matter **315**, 64 (2002).

[31] A. Jayaraman, V. Narayanamurti, E. Bucher, and R. G. Maines, Phys. Rev. Lett. **25**, 1430 (1970).

[32] D. X. Li, Y. Haga, H. Shida, T. Suzuki, and Y. S. Kwon, Phys. Rev. B **54**, 10483 (1996).

[33] N. V. Shekar and P. Ch. Sahu, J. Mater. Sci. **41**, 3207 (2006).

[34] P. N. Kumta and S. H. Risbud, J. Mater. Sci. **29**, 1135 (1994).

[35] J. A. Savage, J. Non-Cryst. Solids **47**, 101 (1982).

[36] P. Bhardwaj and S. Singh, Phys. Solid State **58**, 2081 (2016).

[37] W. Reim, J. Magn. Magn. Mater. **58**, 1 (1986).

[38] R. Pittini, J. Schoenes, and P. Wachter, Phys. B Condens. Matter **206–207**, 92 (1995).

[39] R. M. Amos and W. L. Barnes, Phys. Rev. B **55**, 7249 (1997).

[40] R. Halabi and M. Korek, J. Mod. Phys. **06**, 546 (2015).

[41] A. Svane, P. Strange, W. M. Temmerman, Z. Szotek, H. Winter, and L. Petit, Phys. Status Solidi B **223**, 105 (2001).

[42] C. Çoban, K. Çolakoğlu, and Y. Ö. Çiftçi, Mater. Chem. Phys. **125**, 887 (2011).

[43] C.-G. Duan, R. F. Sabirianov, W. N. Mei, P. A. Dowben, S. S. Jaswal, and E. Y. Tsymbal, J. Phys. Condens. Matter **19**, 315220 (2007).

[44] A. Ennaoui, S. Fiechter, W. Jaegermann, and H. Tributsch, J. Electrochem. Soc. **133**, 97 (1986).

[45] R. Masrour, E. K. Hlil, M. Hamedoun, A. Benyoussef, O. Mounkachi, and H. El Moussaoui, J. Magn. Magn. Mater. **361**, 197 (2014).

[46] S. Palchoudhury, K. Ramasamy, J. Han, P. Chen, and A. Gupta, Nanoscale Adv. **5**, 2724 (2023).

[47] M. D. Segall, P. J. D. Lindan, M. J. Probert, C. J. Pickard, P. J. Hasnip, S. J. Clark, and M. C. Payne, J. Phys. Condens. Matter **14**, 2717 (2002).

Chapter I: Transition Metal Selenides (TMSe)

I-1 Introduction

The physical characteristics of a solid are closely linked to the behavior of the electrons that make it up. The main aim of condensed matter theory is to study the electronic structure of solids. Electronic structure theory aids in interpreting experimental results and acts as a predictive tool. The examination of material properties is closely tied to advances in micro- and nano-electronics. A good understanding of material properties is essential, firstly, for managing the production of electronic devices and secondly, for discovering new materials with interesting features.

Transition metals have become a significant component of everyday life. These elements make up 90% of the periodic table. Their particularity lies in their d orbitals, which give them certain distinctive features. Color, magnetism, and conductivity.

The 38 chemical elements [1] with atomic numbers 21 to 30, 39 to 48, 72 to 80, and 104 to 112 are often known as transition metals. This term is derived from their positions on the periodic table of elements, which represent the successive addition of one electron to the d orbital as one moves from one atom to the next within a period. Table I-1 shows the periodic table.

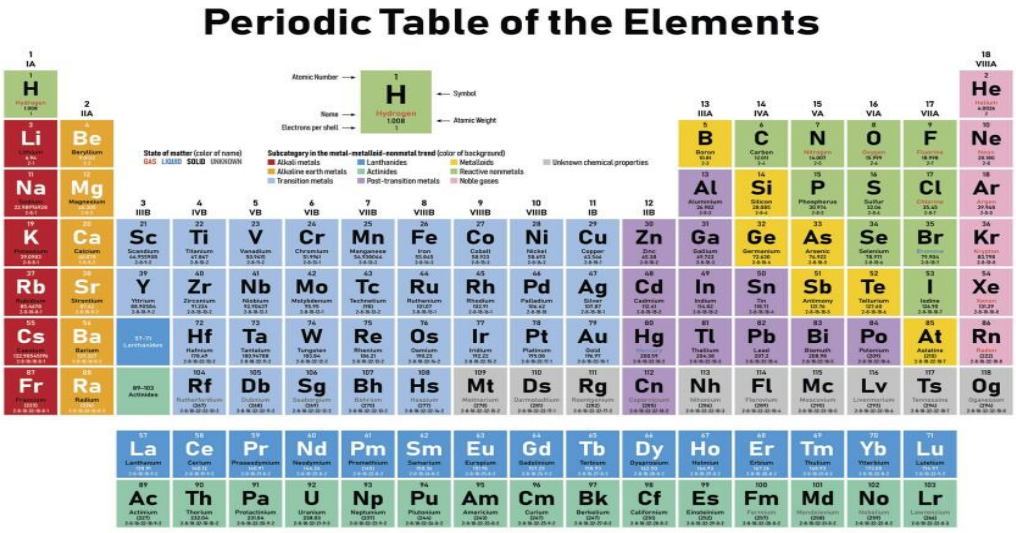

Table I- 1: Periodic table of elements showing transition metals.

In recent years, transition metal chalcogenides (TMCs) have garnered a lot of interest for technological uses in an array of fields, including photo catalysis, sensors, solar cells, supercapacitors, and electro catalysis because of their optical, electrical, and electrochemical properties [2]. Transition metal chalcogenides (TMCs) are materials composed of two species:

transition metals (groups I_B-$VIII_B$ such as Sc, Mn, Zn, Ta, Mo, W, Cd, Hg, etc) and from the VI_A group, especially, the group VI_A elements considered are sulfides (S), selenides (Se) and tellurides (Te). Generally, transition metal tellurides, sulfides and selenides have the general formula MX_n (M= transition metals, X= chalcogenide atom, with n is an integer). With exceptional properties, transition metal chalcogenides offer a wide range of physical systems for study. We chose manganese (Mn) and scandium (Sc) from the first row of transition metals for this investigation. We selected cadmium (Cd) and mercury (Hg) for Group II_B (or Group 12) and focused on selenides among the chalcogenides.

The following section will present the definition of transition metal selenides (TMSe). Moreover, information on cadmium selenides (CdSe), manganese selenides (MnSe), scandium selenides (ScSe) and mercury selenides (HgSe); in the last part of this chapter, we will present some applications of transition metal selenides (TMSe).

I-2 Transition metal selenides (TMSe)

Because of their fascinating physical characteristics and wide variety of uses, transition metal selenides (TMSe) are an important family of materials that have been thoroughly studied. These compounds are attractive for use in optoelectronics, spintronic, photovoltaics, thermoelectric devices, and magnetic storage technologies because of their unique combination of chemical stability, electrical tunability, and structural flexibility [3–13]. In addition, TMSe are highly sought-after materials for electrochemical energy conversion and storage systems, effective counter electrode materials for dye-sensitized solar cells, and an electrocatalyst for general water splitting. The electronic band structure, electrical characteristics, and magnetic properties are essential in determining their suitability for different device applications. For rapid development in this field, TMSe continues to attract interest for their adaptability in next-generation electrochemical technologies.

I-3 Cadmium selenide (CdSe)

Cadmium selenide (CdSe) is among the Group II-VI semiconductor materials necessary for its vast potential applications in various optoelectronic devices, specifically, laser diodes emitting visible light and in the blue region of the spectrum. They are also widely used for their high efficiencies in photovoltaic cells [14,15]. Due to their strong iconicity, these compounds are excellent candidates for high electro-optical and electromechanical coupling. It has n-type conductivity in bulk and thin-film form and has a bandgap of 1.74 eV at room temperature. CdSe has found specialized use in infrared windows [16–20]. Moreover, its tunable

morphology and size at the nanoscale have expanded its range of applications to include bio imaging, photovoltaics, lasers, transistors, LEDs, and catalysis [21]. Interestingly, CdSe also serves as a promising thin-film material for detectors, lasers, optoelectronic devices, and photo electrochemical cells [22] and is regarded as a leading candidate for room-temperature nuclear radiation detectors [23]. High-quality CdSe single crystals are commonly produced using vapor phase methods, such as vertical unseeded vapor growth or the horizontal Bridgman technique [23]. The optical, thermodynamic, structural, electrical, and compositional characteristics of CdSe in bulk and thin-film forms have been the subject of several investigations [24–33].

Three types of CdSe have been observed: wurtzite, sphalerite, and rock-salt. Their respective structures are hexagonal and cubic. Since Zn and Cd belong to the same periodic table group, their structures are similar. Because the sphalerite form is unstable, heating it transforms CdSe into the wurtzite form. This transition occurs between 130 and 700 °C and is finished at 700 °C. Complex structural changes in the high-pressure phases of several III–V and II–VI compounds have been identified using X-ray diffraction techniques. About 60 years ago, Edwards and Drickamer [34] conducted the first experimental study of pressure induced phase transitions in CdS and CdSe. Notably, the high-pressure phase sequence seen in sulfides and selenides is very different from that of tellurides. Later, angle-dispersive X-ray (ADX) analysis of CdSe was carried out by Nelmes and McMahon [35] up to 85 GPa. A continuous shift from the NaCl structure to the Cmcm structure was observed in their results at 27.0 GPa. At 36 GPa, there was also evidence of a further transformation into a deformed Cmcm structure.

I-4 Mercury selenide (HgSe)

Mercury chalcogenides are a particular class of semiconductors with a lot of interest due to their electrical and optical properties, making them a viable choice for modern optoelectronic and spintronic applications [3–5,8].These compounds are different from the other group II–VI semiconductors such as Cd and Zn chalcogenides, finding application in making various light-emitting devices and sensors. The electrical configuration (n-1) d^{10} ns^2 and the covalent bonding of Cadmium (Cd), Zinc (Zn) and mercury (Hg) chalcogenides are very similar across the group.

The bandgap is an essential parameter due to its effect on the semiconductor's electrical, optical, and magnetic properties. The Experimental examination further demonstrates that the chalcogenides of Cd and Zn indicate wide and direct bandgap (Γ–Γ) semiconductor

characteristics. However, some examinations of HgSe have a marginally positive fundamental band gap [3], a negative band gap [36], and a zero band gap [37]. The mercury chalcogenides are considered semimetal or zero-gap semiconductors. The chalcogenides of mercury differ from those of cadmium (Cd) and zinc (Zn). Under normal conditions, HgS is found in both metastable zinc-blende (B3) and trigonal (cinnabar -B9-) phases. HgSe and HgTe has similar qualities in B3 phases, and this pushes to the B9 structure at low pressure (P~ 2 GPa) [37,38], However, upon applying additional pressure to the B9 structure, it has been noticed that the structure has altered to the rock-salt phase [35,39,40]. Upon further increase in pressure, both compounds enter a distorted NaCl-type or $PbCl_2$-type polymorph [40–42]. Additionally, Through interdiffusion-driven cation-exchange mechanisms, nanoscale experiments have shown that HgSe nanocrystals have tunable infrared bandgaps [43], adding a new level of understanding to the links between structure and property. Changes in the electronic structure and phonon activity, including the potential appearance of topologically non-trivial phases under strain or pressure, are closely linked to this pressure-induced polymorphism [3–5].

I-5 Manganese selenide (MnSe)

The transport, optical, and magnetic features of transition metal chalcogenides like tellurides, selenides, and sulfides have garnered much attention. Manganese-based chalcogenides are particularly famous as magnetic semiconductors, giving intrinsic magnetism and varied optical features [44,45]. These advancements could all considerably benefit infrared detectors, spintronic devices, and solar cells [7,46] These materials display an assortment of magnetism, such as “ferromagnetic, paramagnetic, and antiferromagnetic,” which are identified by their large optical band gaps. Manganese is a crucial component in the first row of transition metals. Manganese compounds are valuable electrode materials because of their inexpensive cost, favorable environmental characteristics, good natural abundance, and high operating voltage.

The α-phase (NaCl type), γ-phase (wurtzite type), and β-phase (zinc-blende type) are the three different polymorphs of manganese selenide [47]. and is a p-type semiconductor (Eg = 2.0 eV) [48,49]. The phase α (rock salt) is the most thermodynamically stable due to its reduced band gap and electrical conductivity. In contrast to the metastable γ-phase, the β-phase is extremely unstable and only occurs as an impurity." The γ-phase is hexagonal in manganese selenide, whereas the α and β phases are cubic [50].

I-6 Scandium selenide (ScSe)

Because of their unique magnetic, optical, and acoustic properties that are sensitive to temperature and pressure, as well as their electrical structure, rare earth compounds have recently garnered a lot of attention [51–54]. These materials exhibit remarkable magnetic, optical, and electronic characteristics, enabling their integration into diverse applications, including optical glasses, magneto-optical devices, and advanced electronic components [55–61]. Metal, semiconductors and insulators characterize rare earth chalcogenides. Chalcogenides are known to have exceptional properties and are classified as a group VI element of the periodic table. Scandium is a group III element with rare-earth metal characteristics. Their f-shell electrons have a high connection, which means that a change in pressure can cause large changes in their chemical and physical properties. Because rare earth metals are used in low-carbon technology in particular, their demand has grown over time. Additionally, in electronic devices, laser systems, non-linear optics, various industrial processes [62–64], and glassware [65]. Under high pressure, these materials exhibit phase change and are useful in nonlinear optics. Few theoretical and experimental studies have been conducted on the structural characteristics of chalcogenides and rare earth compounds.

Scandium chalcogenides ScSe crystallize in a NaCl (B1) structure at ambient conditions, but at high pressure, their structural and electronic properties undergo notable change [67,68], Early work by Piers et al. [68] paved the way, with subsequent studies by Maachou et al. [69] and Purvee Bhardwaj et al. [70] Documenting a pressure-induced structural phase transition from the NaCl-type (B1) to the CsCl-type (B2) phase. More recent studies have suggested the potential stability of additional structures such as the NiAs-type for ScSe[71]. While there is consensus regarding the metallic character of these compounds [70–74], discrepancies remain concerning their structural phase transitions and pressure stability ranges. For example, Maachou et al [69] predicted a B1→B2 transition at 84.5 -86 GPa for ScS and 53-52 GPa for ScSe. Whereas, Ahmad et.al [75] explored additional high-pressure phases ZnS-type (B3) and their corresponding optical and thermodynamic properties. Complementary work by Guo et al [76] and Shrivastava et al. [72] highlighted significant variations in optical conductivity, band structure, and superconducting transition temperature.

I-7 Some Applications of transition metal selenides

I-7.1 Optoelectronics

A family of systems known as optoelectronic devices either uses electrical energy to create light or transforms light into electrical energy. Their operation is fundamentally based on the interaction between photons and the electronic structure of semiconductors. When photons with energy above a semiconductor's band gap are absorbed, electrons are promoted from the valence band to the conduction band, creating free charge carriers (electrons and holes). This photoexcitation process underlies the functionality of various optoelectronic components.

Optoelectronic devices have become indispensable in modern technology, with applications in solar energy conversion, telecommunication, sensing, automation and display technologies. Common examples include photodiodes, phototransistors, photothyristors, light-dependent resistors (LDRs), solar cells, laser diodes, and light-emitting diodes (LEDs) [3–13].

Transition metal selenides (TMSs), especially CdSe, HgSe, ScSe, and MnSe, have emerged as promising candidates for such applications due to their tunable direct band gaps, strong optical absorption, and excellent luminescent properties. CdSe and HgSe are widely used in photodetectors, solar cells, and light-emitting devices due to their direct optical transitions and remarkable their photoresponse across the visible to infrared spectrum [3–5,8]. At the same time, ScSe and MnSe show interesting electrical and magnetic properties, making them beneficial for spintronic and multifunctional optoelectronic applications [7,46]

I-7.2 Counter-electrode for Dye-sensitized solar cells

Because of its low cost, straightforward preparation process, low toxicity, and ease of manufacture, dye-sensitized solar cells (DSCs) are thin-film solar cells that have been the subject of intensive research for more than 20 years. However, given their high cost, scarcity, and long-term stability, current dye-sensitized solar cell materials have a lot of room for replacement. The counter-electrode (CE) is one of the key parts of DSCs; the kind of CE has a significant impact on how well DSCs operate photovoltaically. High electrocatalytic activity, strong electrical conductivity, and chemical stability are characteristics of superior CE catalysts.

The counter-electrode (CE) has two essential roles:

- To collect electrons from the external circuit.
- To transfer the electrons to recycle the redox species of the redox couple (I_3/I) through catalytic reduction.

Traditionally, platinum (Pt) was the ideal material for catalytic CE, but its limited reserves, high cost, and compromised stability impeded its further development. TMSs are appropriate for electrocatalyst application because they have distinctive electrical characteristics, intriguing chemical behavior, and strong chemical stability. These are suitable for use as electrocatalysts, despite being used for the oxygen reduction reaction in fuel cells [77]. TMS-CE and traditional Pt-CE are similar in terms of conversion efficiency for DSCs. The electrocatalytic behaviors of TMSs as CE in DSCs have only been theoretically investigated in a small number of papers, where Metal selenides are becoming more and more popular as a subject of research, as seen by the steadily rising number of recently published articles on electrode materials [78]. Due to their favorable electronic structures, tunable band gaps, and high electrical conductivity, transition metal selenides such as CdSe, HgSe, ScSe, and MnSe are particularly promising candidates for enhancing the performance of DSCs. Their unique combination of semiconducting and metallic characteristics allows for efficient charge transfer and catalytic activity at the electrode electrolyte interface, making them ideal for next-generation cost-effective and high-performance counter electrodes (CE).

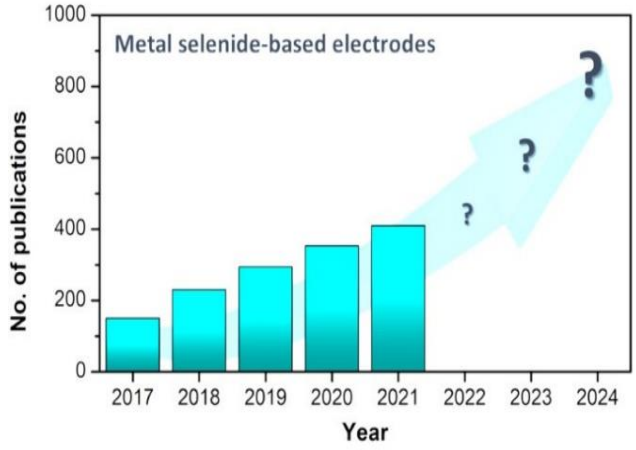

Figure I-1 : Plot for publication trend of metal selenide electrode materials (from Scopus) [79].

I-7.3 Electro catalyst for general water splitting

Electrochemical water splitting represents one of the most promising technologies for producing green hydrogen. It consists of two major parts: the hydrogen evolution reaction (HER) and the oxygen evolution reaction (OER). Developing efficient and affordable electrocatalysts is critical in enhancing electrochemical water splitting and simplifying the overall system design. Due to their reported good activity and low-cost properties, transition metal selenides are regarded as one of the most efficient electrocatalysts for hydrogen evolution.

The effective electro catalysts have more active sites to facilitate the flow of charge carriers, rich surface chemistry, lower internal voltage loss, lower Gibbs free energy, more excellent electrical conductivity, and higher specific and electrochemical surface area. Many electrocatalysts, including noble metals like ruthenium (Ru), rhodium (Rh), palladium (Pd), iridium (Ir), and platinum (Pt) [79], as well as their compounds have been produced and used; however, their high cost relative to production, low stability, and rare natural occurrence pose problems for commercial applications. Due to their semi-conductive behavior and large edge sites for the HER process, transition metal chalcogenides have received much attention. While the electrocatalytic feature of sulfides and selenides for the HER process is similar, some sulfides have poor electrocatalytic behavior, low density of active edge sites and a low charge transfer process due to their higher electronegativity and relatively stronger S-H bond than Se-H bond. In this context, transition metal selenides such as CdSe, HgSe, ScSe, and MnSe stand out as highly promising electrocatalysts, combining favorable electronic structures, chemical stability, and surface reactivity. Their tunable electronic and catalytic characteristics make them ideal for next-generation, efficient, cost-effective hydrogen evolution systems.

I-7.4 Electrochemical energy conversion and storage systems

A significant factor driving innovation in the energy storage sector and the search for materials with high specific energy at a reasonable price is the growing need for sustainable energy. The subject of energy technology known as electrochemical energy conversion deals with electrochemical energy conversion techniques, such as fuel cells and photoelectrochemical cells. Batteries, supercapacitors, and fuel cells are the three types of electrochemical energy conversion and storage technologies. Numerous portable electronics, such as laptop computers, cell phones, and cameras, need batteries. Electrochemical energy storage covers all types of secondary batteries. Batteries convert the chemical energy contained in their active materials into electric energy by an electrochemical oxidation-reduction reaction. Supercapacitors, also known as ultracapacitors, utilize the separation of charges on the electrode surfaces to store energy electrostatically. They have a long cycle life, quick charging and discharging rates, and a high power density. Applications requiring frequent, high-power energy bursts are best suited for supercapacitors.

Recent years have seen, transition metal chalcogenides (TMsCs), particularly transition metal selenides (TMSes), have been investigated have attracted considerable attention as promising electrode materials for supercapacitor applications. Compared with conventional

materials, selenide-based electrodes display enhanced electrochemical activity due to their large surface area, high intrinsic electronic conductivity 1×10^{-3} S m^{-1}, and unique physical, chemical, and electronic properties. These characteristics not only facilitate efficient charge transport but also contribute to their remarkable cycle stability, making CdSe, HgSe, ScSe, and MnSe highly appealing for the development of next-generation energy storage devices.

References

[1] M. Gerloch and E. C. Constable, *Transition Metal Chemistry: The Valence Shell in d-Block Chemistry*, 1st ed. (Wiley, 1994).

[2] W. Chen, Y. Qu, L. Yao, X. Hou, X. Shi, and H. Pan, J. Mater. Chem. A **6**, 8021 (2018).

[3] K.-U. Gawlik, L. Kipp, M. Skibowski, N. Orłowski, and R. Manzke, Phys. Rev. Lett. **78**, 3165 (1997).

[4] A. N. Chantis, M. Van Schilfgaarde, and T. Kotani, Phys. Rev. Lett. **96**, 086405 (2006).

[5] F. Virot, R. Hayn, M. Richter, and J. Van Den Brink, Phys. Rev. Lett. **111**, 146803 (2013).

[6] S. Palchoudhury, K. Ramasamy, J. Han, P. Chen, and A. Gupta, Nanoscale Adv. **5**, 2724 (2023).

[7] K. Ozawa, S. Anzai, and Y. Hamaguchi, Phys. Lett. **20**, 132 (1966).

[8] Y. Selmani, H. Labrim, A. Jabar, and L. Bahmad, Int. J. Mod. Phys. B **38**, 2450334 (2024).

[9] S. Ferahtia, S. Saib, N. Bouarissa, and S. Benyettou, Superlattices Microstruct. **67**, 88 (2014).

[10] S. Mnasri, S. Abdi-Ben Nasrallah, N. Sfina, N. Bouarissa, and M. Said, Semicond. Sci. Technol. **24**, 095008 (2009).

[11] W. Zhou, S. Wu, and S. Li, J. Magn. Magn. Mater. **395**, 166 (2015).

[12] O. Kavcı and S. Cabuk, Comput. Mater. Sci. **95**, 99 (2014).

[13] Adachi S., *Properties of Group-IV, III-V and II-VI Semiconductors*, Wiley (2005).

[14] D. B. Laks and C. G. Van De Walle, Phys. B Condens. Matter **185**, 118 (1993).

[15] S. O. Kasap and P. Capper, editors , *Springer Handbook of Electronic and Photonic Materials* (Springer, New York, 2006).

[16] *CRC Handbook of Chemistry and Physics, 92nd Edition* (CRC Press, 2011).

[17] H. Zhang, B. Hu, L. Sun, R. Hovden, F. W. Wise, D. A. Muller, and R. D. Robinson, Nano Lett. **11**, 5356 (2011).

[18] R. C. Somers, M. G. Bawendi, and D. G. Nocera, Chem. Soc. Rev. **36**, 579 (2007).

[19] N. C. Anderson and J. S. Owen, Chem. Mater. **25**, 69 (2013).

[20] A. K. Nayak and N. K. Sahu, editors , *Nanostructured Materials for Visible Light Photocatalysis* (Elsevier, Amsterdam, Netherlands Oxford, United Kingdom Cambridge, MA, 2022).

[21] S. J. Dhoble, A. Nande, N. T. Kalyani, A. Tiwari, and A. K. Arof, editors , *Functional Materials from Carbon, Inorganic, and Organic Sources: Methods and Advances* (Woodhead Publishing, Cambridge, MA Kidlington, 2023).

[22] A. S. Khomane and P. P. Hankare, J. Alloys Compd. **489**, 605 (2010).

[23] M. Roth, Nucl. Instrum. Methods Phys. Res. Sect. Accel. Spectrometers Detect. Assoc. Equip. **283**, 291 (1989).

[24] H. H. Gürel and H. Ünlü, Mater. Sci. Semicond. Process. **16**, 1619 (2013).

[25] A. Burger, D. O. Henderson, S. H. Morgan, and E. Silberman, J. Cryst. Growth **109**, 304 (1991).

[26] S. Zhu, B. Zhao, Y. Jin, W. Yang, X. Chen, and Y. Den, J. Cryst. Growth **240**, 454 (2002).

[27] T. Zeng, B. Zhao, S. Zhu, Z. He, B. Chen, and Z. Tan, J. Cryst. Growth **316**, 15 (2011).

[28] H. M. Kotb, M. A. Dabban, A. Y. Abdel-latif, and M. M. Hafiz, J. Alloys Compd. **512**, 115 (2012).

[29] A. V. Kokate, U. B. Suryavanshi, and C. H. Bhosale, Sol. Energy **80**, 156 (2006).

[30] V. Swaminathan, V. Subramanian, and K. R. Murali, Thin Solid Films **359**, 113 (2000).

[31] O. Yamamoto, T. Sasamoto, and M. Inagaki, J. Mater. Res. **13**, 3394 (1998).

[32] I. Un Nabi Lone, S. S. M. Mohamed, I. B. Shameem Banu, and S. Sathik Basha, Mater. Chem. Phys. **192**, 291 (2017).

[33] B. Su and K. L. Choy, Thin Solid Films **361–362**, 102 (2000).

[34] A. L. Edwards and H. G. Drickamer, Phys. Rev. **122**, 1149 (1961).

[35] R. J. Nelmes and M. I. McMahon, in *Semiconductors and Semimetals*, Vol. 54 (Elsevier, 1998), pp. 145–246.

[36] W. Szuszkiewicz, Phys. Status Solidi B **91**, 361 (1979).

[37] M. Von Truchseß, A. Pfeuffer-Jeschke, C. R. Becker, G. Landwehr, and E. Batke, Phys. Rev. B **61**, 1666 (2000).

[38] B. Al Shafaay, F. El Haj Hassan, and M. Korek, Comput. Mater. Sci. **83**, 107 (2014).

[39] M. I. McMahon, R. J. Nelmes, H. Liu, and S. A. Belmonte, Phys. Rev. Lett. **77**, 1781 (1996).

[40] T.-L. Huang and A. L. Ruoff, Phys. Rev. B **31**, 5976 (1985).

[41] M. I. McMahon and R. J. Nelmes, Phys. Status Solidi B **198**, 389 (1996).

[42] S. Radescu, A. Mujica, and R. J. Needs, Phys. Rev. B **80**, 144110 (2009).

[43] W. Lee and A. M. Smith, Nat. Synth. **3**, 1243 (2024).

[44] A. Ennaoui, S. Fiechter, W. Jaegermann, and H. Tributsch, J. Electrochem. Soc. **133**, 97 (1986).

[45] R. Masrour, E. K. Hlil, M. Hamedoun, A. Benyoussef, O. Mounkachi, and H. El Moussaoui, J. Magn. Magn. Mater. **361**, 197 (2014).

[46] S. Palchoudhury, K. Ramasamy, J. Han, P. Chen, and A. Gupta, Nanoscale Adv. **5**, 2724 (2023).

[47] A. Khaldi, N. Bouarissa, H. Ghodbane, and L. Tabourot, Phys. B Condens. Matter **553**, 6 (2019).

[48] N. Li, Y. Zhang, H. Zhao, Z. Liu, X. Zhang, and Y. Du, Inorg. Chem. **55**, 2765 (2016).

[49] M. Prasad, A. K. Pandit, T. H. Ansari, and R. A. Singh, Mater. Chem. Phys. **30**, 13 (1991).

[50] V. Thanigaimani and M. A. Angadi, Thin Solid Films **245**, 146 (1994).

[51] G. Vaitheeswaran, V. Kanchana, and M. Rajagopalan, Phys. B Condens. Matter **315**, 64 (2002).

[52] A. Jayaraman, V. Narayanamurti, E. Bucher, and R. G. Maines, Phys. Rev. Lett. **25**, 1430 (1970).

[53] D. X. Li, Y. Haga, H. Shida, T. Suzuki, and Y. S. Kwon, Phys. Rev. B **54**, 10483 (1996).

[54] N. V. Shekar and P. Ch. Sahu, J. Mater. Sci. **41**, 3207 (2006).

[55] P. N. Kumta and S. H. Risbud, J. Mater. Sci. **29**, 1135 (1994).

[56] J. A. Savage, J. Non-Cryst. Solids **47**, 101 (1982).

[57] P. Bhardwaj and S. Singh, Phys. Solid State **58**, 2081 (2016).

[58] W. Reim, J. Magn. Magn. Mater. **58**, 1 (1986).

[59] R. Pittini, J. Schoenes, and P. Wachter, Phys. B Condens. Matter **206–207**, 92 (1995).

[60] R. M. Amos and W. L. Barnes, Phys. Rev. B **55**, 7249 (1997).

[61] R. Halabi and M. Korek, J. Mod. Phys. **06**, 546 (2015).

[62] A. Svane, P. Strange, W. M. Temmerman, Z. Szotek, H. Winter, and L. Petit, Phys. Status Solidi B **223**, 105 (2001).

[63] C. Çoban, K. Çolakoğlu, and Y. Ö. Çiftçi, Mater. Chem. Phys. **125**, 887 (2011).

[64] C.-G. Duan, R. F. Sabirianov, W. N. Mei, P. A. Dowben, S. S. Jaswal, and E. Y. Tsymbal, J. Phys. Condens. Matter **19**, 315220 (2007).

[65] P. Bhardwaj and S. Singh, Procedia Comput. Sci. **57**, 160 (2015).

[66] J. P. Dismukes and J. G. White, Inorg. Chem. **3**, 1220 (1964).

[67] F. Hulliger and G. W. Hull, Solid State Commun. **8**, 1379 (1970).

[68] S. M. Peiris, M. T. Green, D. L. Heinz, and J. K. Burdett, Inorg. Chem. **35**, 6933 (1996).

[69] A. Maachou, H. Aboura, B. Amrani, R. Khenata, S. Bin Omran, and D. Varshney, Comput. Mater. Sci. **50**, 3123 (2011).

[70] P. Bhardwaj and S. Singh, Procedia Comput. Sci. **57**, 160 (2015).

[71] M. Abu-Jafar, R. Dayton-Oxland, R. Jaradat, A. A. Mousa, and R. Khenata, Phase Transit. **93**, 773 (2020).

[72] D. Shrivastava and S. P. Sanyal, Comput. Condens. Matter **21**, e00418 (2019).

[73] S. K. Yadav, S. Dahal, R. Khadka, B. Guragain, P. Pokharel, P. Oli, and D. Adhikari, Eng. Rep. **7**, e13115 (2025).

[74] C. Wang, L. Gao, R. Wang, B. Ming, G. Guo, and H. Yan, Phys. Lett. A **384**, 126373 (2020).

[75] A. A. Ahmad, S. Mahmoud, B. Alshafaay, R. Halabi, and F. El Haj Hassan, Indian J. Phys. **93**, 1129 (2019).

[76] H. Guo, J. Zhao, C. Chen, S. Li, W. Jiang, H. Fan, X. Tian, and S. A. Yang, J. Mater. Sci. **55**, 14883 (2020).

[77] B. T. Luk, C.-M. Jack Hu, R. H. Fang, D. Dehaini, C. Carpenter, W. Gao, and L. Zhang, Nanoscale **6**, 2730 (2013).

[78] I. Hussain, S. Sahoo, C. Lamiel, T. T. Nguyen, M. Ahmed, C. Xi, S. Iqbal, A. Ali, N. Abbas, M. S. Javed, and K. Zhang, Energy Storage Mater. **47**, 13 (2022).

[79] Y. Abghoui and E. Skúlason, J. Phys. Chem. C **121**, 24036 (2017).

Chapter II: Density Functional Theory (DFT)

II-1 Introduction

Erwin Schrödinger provided a wave equation for a collection of atoms and electrons at the start of the 20th century. Unfortunately, it only has an exact solution for atomic or molecular systems with a single electron. For this reason, in most cases, the equation is too complicated to admit an analytical solution, so its resolution is approached. Quantum physics aims to obtain a solution to the Schrödinger equation as close as possible to the real physical system. One of the problems of solid-state physics that presents a current challenge for physicists of matter is understanding and mastering the intimate organization of these particles that make up crystals.

This chapter will present an array of approximation techniques for determining the electrical characteristics of solids. Density functional theory (DFT), which is based on the Hohenberg-Kohn theorem and will provide a broad theoretical framework for this thesis, will be introduced after outlining the drawbacks of methods that are only based on the N-body wave function. Only advancements in condensed matter are covered, and the concepts are extremely broad. We will next describe the formalism that was employed, including the many forms of functional (LDA, GGA, etc.), as well as the relevance of the exchange-correlation functional and the explanation of the Kohn-Sham equations.

II-2 Schrödinger equation of a crystalline solid

Consideration is given to a material system with n electrons and N atomic nuclei. The wave function, which is controlled by the time-independent Schrödinger equation, incorporates all information [1]:

$$H|\Psi\rangle = E|\Psi\rangle \qquad II-1$$

With:

H: Hamiltonian operator that contains particles' kinetic energy and potential energy.

Ψ: The wave function of the system.

E: The total energy of the crystal.

Generally, the Hamiltonian operator is written:

$$H = T_e + T_n + V_{e-e} + V_{n-n} + V_{e-n} \qquad II-2$$

With:

T_e: The kinetic energy of electrons.

$$T_e = \sum_{i=1}^{N} \frac{P_i^2}{2m_e} = \sum_{i=1}^{N} \frac{-\hbar^2}{2m_e} \Delta_i \qquad \text{II} - 3$$

T_n: The kinetic energy of nuclei.

$$T_n = \sum_{i=1}^{n} \frac{P_i^2}{2M_n} = \sum_{i=1}^{n} \frac{-\hbar^2}{2M_n} \Delta_i \qquad \text{II} - 4$$

V_{e-e}: The electron-electron interaction potential.

$$V_{e-e} = \frac{1}{2} . \frac{1}{4\pi\varepsilon_0} \sum_{i \neq j} \frac{e^2}{|\vec{r_i} - \vec{r_j}|} \qquad \text{II} - 5$$

V_{n-n}: The potential for nuclei-nuclei interaction.

$$V_{n-n} = \frac{1}{2} . \frac{1}{4\pi\varepsilon_0} \sum_{\alpha \neq \beta} \frac{Z_\alpha Z_\beta e^2}{|\overrightarrow{R_\alpha} - \overrightarrow{R_\beta}|} \qquad \text{II} - 6$$

V_{e-n}: The electron potential-nuclei interaction.

$$V_{e-n} = -\frac{1}{4\pi\varepsilon_0} \sum_{i,\alpha} \frac{Z_\alpha e^2}{|\vec{r_i} - \overrightarrow{R_\alpha}|} \qquad \text{II} - 7$$

$\vec{r_i} = 1 \ldots N$ represents the coordinates of electrons.

$\overrightarrow{R_\alpha} = 1 \ldots . . n$ Are the coordinates of the nuclei.

The Ψ wave function depends on the coordinates of all particles, i.e.

$$(T_e + T_n + V_{e-e} + V_{n-n} + V_{e-n}) \Psi\left(\vec{r_1}, \vec{r_2}, \ldots . . \overrightarrow{R_1}, \overrightarrow{R_2} \ldots . .\right) = \mathrm{E}\Psi\left(\vec{r_1}, \vec{r_2}, \ldots . \overrightarrow{R_1}, \overrightarrow{R_2} \ldots .\right) \text{II-8}$$

Equation I-2 encompasses all the observable properties of the electron-nucleus system. To determine its physical and chemical characteristics, simply solve the equation. However, calculating the Schrödinger equation for an interacting (N-e + N-N) body system is complex. For poly-electronic systems, the equation involves 3n (z+1) variables, so it is necessary to use approximation methods to solve the Schrödinger equation approximately. The three main levels of simplification typically employed are:

1. Born-Oppenheimer approximation or adiabatic approximation.
2. The Hartree-Fock approximation or the formalism of functional density theory.
3. The approximations inherent in solving equations.

II-3 Born-Oppenheimer approximation

This approximation [2] is that any nucleus's mass is substantially greater than the electron's. For this reason, the motion of nuclei with electrons can be neglected. Therefore, electrons are considered to evolve in a potential created by fixed atoms. In this context, the nuclei's kinetic energy is zero ($T_n = 0$), and the Coulomb energy V_{n-n} due to repulsion between the nuclei becomes a constant. At this stage, we move from a problem for which we had to solve the Schrödinger equation of an N-electron + M-nucleus system, to the Schrödinger equation for an N-electron system sensing the potential of nuclei. Therefore, the Hamiltonian of electrons is given by:

$$H_e = T_e + V_{e-e} + V_{e-n} \qquad \text{II} - 9$$

$$H_e = \sum_{i=1}^{N} \frac{-\hbar^2}{2m_e}\Delta_i + \frac{1}{2}.\frac{1}{4\pi\varepsilon_0}\sum_{i\neq j}\frac{e^2}{|\vec{r_i}-\vec{r_j}|} - \frac{1}{4\pi\varepsilon_0}\sum_{i,\alpha}^{n}\frac{Z_\alpha e^2}{|\vec{r_i}-\vec{R_\alpha}|} \qquad \text{II} - 10$$

The electronic Schrödinger equation can be written in the following manner:

$$H_e\psi = E_e\psi \qquad \text{II} - 11$$

E_e: Fixed nuclei create the energy of electrons travelling in the field.

Although these simplifications have been made, the resolution of this equation is still highly challenging due to the requirement of 3n coordinates of space for a system with n electrons. This is why it is often associated with the Hartree approximation [3].

II-4 Hartree-Fock approximation

A method for computing approximate poly-electronic wave functions by expressing them as products of mono-electronic wave functions was proposed by Hartree in 1927 [3]. Each electron has an orbital, and the total wave function is expressed as the product of the particle's orthogonal wave functions:

$$\Psi(\vec{r_i}) = \Psi_1(\vec{r_1}).\Psi_2(\vec{r_2}).\Psi_3(\vec{r_3}) \ldots\ldots \Psi_N(\vec{r_N}) \qquad \text{II} - 12$$

Fock corrected the Hartree method in 1930, which did not follow the antisymmetric principle of the wave function [4]. Indeed, the Pauli Exclusion Principle [5], states that two electrons cannot be in the same quantum state at the same time.

The Schrödinger equation of a quantum system with n electrons and N nuclei can be approximated using the Hartree-Fock method [4] where the poly-electronic wave function Ψ_{HF} is written as a Slater determinant [6] formed of spin mono-electronic orbitals that respect the wave function's antisymmetric:

$$\Psi(\vec{r_i}) = \frac{1}{\sqrt{N!}} \begin{vmatrix} \psi_1(\vec{r}_1)\psi_1(\vec{r}_1)\cdots\psi_1(\vec{r}_1) \\ \psi_1(\vec{r}_1)\psi_1(\vec{r}_1)\cdots\psi_1(\vec{r}_1) \\ \vdots \quad \vdots \quad \ddots \quad \vdots \\ \psi_1(\vec{r}_1)\psi_1(\vec{r}_1)\psi_1(\vec{r}_1) \end{vmatrix} \qquad \text{II} - 13$$

N: is a normalization factor [7].

In relation to the single electron wave functionsΨ_i, this establishes the wave functions and minimizes the total energy. A single electron wave equation, a generalization of the Hartree equation, results from this:

$$\left[-\frac{\hbar^2}{2m_e}\nabla^2 + V_{ext}(\vec{r}) + V_H(\vec{r}) + V_X(\vec{r})\right]\psi_i(\vec{r}) = E\psi_i(\vec{r}) \qquad \text{II} - 14$$

$V_x(\vec{r})$ Is the effect of the Fock term on a wave function that defines it $\psi_i(\vec{r})$:

$$V_x(\vec{r})\psi_i(\vec{r}) = -\sum \delta_{\sigma_i\sigma_j}\psi_j(\vec{r}) \int \frac{\psi_j^*(\vec{r})\psi_i(\vec{r})}{|\vec{r}-\vec{r}'|} d^3\overrightarrow{r'} \qquad \text{II} - 15$$

II-5 Density Functional Theory (DFT)

II-5.1 Origins of DFT

Thomas and Fermi first suggested using density as a variable instead of the wave function in 1927 [8,9]. They proposed modeling the kinetic term of the Schrödinger equation using a particular explicit density functional. The weak point of this approach lay in the expression of the kinetic energy, which did not consider atomic orbitals and the precision obtained was inferior to that of Hartree-Fock due to the absence of the exchange term. Dirac improved this theory by adding an exchange energy functional of the electron density, but the electron correlation term was still absent in this new approach. Nevertheless, using the density leads to more straightforward resolutions than in the case of the wave function. Hohenberg and Kohn's approach provided a rigorous framework that allowed us to dispense with all approximations.

II-5.2 Thomas-Fermi approximation

The Thomas-Fermi model is where density functional theory first originated. Shortly after the formulation of the laws of quantum mechanics, Thomas and Fermi (1927) [8,9] attempted to express the kinetic energy, exchange, and correlation energy of the homogeneous electron gas shortly after the rules of quantum mechanics were formulated. They also constructed the precise quantities for the inhomogeneous system as follows:

$$E_\alpha = \int E_\alpha [\rho(r)] dr \qquad \text{II} - 16$$

This approach estimates the electron distribution around an atom using a statistical model, where (r) denotes the energy density related with the segment of the homogeneous electron flow. The mathematical foundation employed was to assert that electrons are equally dispersed in phase space; within each volume $V = l^3$, there exists a constant quantity of electrons N, and it is assumed that the electrons in each cell are independent fermions at a temperature of 0 K [10].

For each volume element d^3r, a sphere of momentum space can be filled up to the Fermi radius P_f [11]:

$$\mathrm{V} = \frac{4}{3}\pi \mathrm{P_f^3(r)} \qquad \text{II} - 17$$

The quantity of electrons in spatial coordinates within this phase space yields:

$$\mathrm{n(r)} = \frac{8}{3l^3}\pi \mathrm{P_f^3} \qquad \text{II} - 18$$

The following formula gives the kinetic energy of a homogeneous gas:

$$\mathrm{T} = \frac{3}{5}\rho \mathrm{E_f} \qquad \text{II} - 19$$

This means that the kinetic energy density is given as follows:

$$\mathrm{E(\rho)} = \frac{3}{5} * \frac{\hbar}{2\mathrm{m}}(3\pi^2)\rho^{\frac{5}{3}} \qquad \text{II} - 20$$

So kinetic energy is written as:

$$\mathrm{T_{TF}} = \mathrm{C_K} \int \rho\,(\mathrm{r})^{\frac{5}{3}}\,\mathrm{dr} \qquad \text{II} - 21$$

With $C_K = 3(3\pi^2)^{2/3}/10 = 2.871\, u.a,$ this is the exact approximation used in DFT. However, the weakness of this approach lies in the expression of the kinetic energy in the absence of orbitals, which prevents it from achieving satisfactory accuracy.

A little later, Dirac [12] proposed taking exchange effects into account by incorporating a term corresponding to the exchange energy density in a homogeneous gas of electrons. All these earlier approximations contributed to the development of DFT.

II-5.3 Hohenberg-Kohn theorem

Once the electron density has been determined, the DFT needs to be established. Hohenberg and Kohn [10] initially articulated this in 1964. It serves as the foundation for the entire DFT, which can be summed up in two theorems.

According to the first theorem: «Any physical property of a submitted N-electron system, the effect of a static external potential V_{ext} can be written, in its ground state, as a function of electronic density$\rho(r)$**».**

This theorem establishes a specific correlation between the electron density and the external potential. The latter determines the number of electrons, so defining the wave function and, consequently, the system's electrical properties. Thus, the following is how the energy of a particular system is expressed:

$$E[\rho(r)] = F_{HK}[\rho(r)] + \int \rho(r)\, V_{ext}(r) d(r) \qquad \text{II} - 22$$

With: $F_{HK} = T_e[\rho(r)] + V_{ee}[\rho(r)]$, This is the Hohenberg-Kohn functional, which is responsible for the repulsive electron-electron interaction's kinetic and potential energy.

Similar to the variation principle first put forward in the Hartree-Fock method for a wave function functional, the second theorem of Hohenberg and Kohn [11]:

$$\frac{\partial E(\psi)}{\partial(\psi)} = 0 \qquad \text{II} - 23$$

However, this time applied to an electron density functional:

$$\left(\frac{\partial E[\rho(\vec{r})]}{\partial \rho(\vec{r})}\right)_{\rho_0(\vec{r})} = 0 \qquad \text{II} - 24$$

The ground state electron density is represented by $\rho_0(\vec{r})$. Every multi−electronic system with an electron number N and an external potential V_{ext} is covered by this second

theorem. When the density $\rho(\vec{r})$ matches the precise density of the ground state$\rho_0(\vec{r})$, the total energy of the system $E[\rho(\vec{r})]$ drops to its lowest value.

$$E(\rho_0) = minE(\rho) \qquad \text{II} - 25$$

The demonstration of the fact that the total energy of a ground state system is a functional of the electronic density, Hohenberg and Kohn expressed this functional $E[\rho(\vec{r})]$ according to the following expression:

$$E[\rho(\vec{r})] = F_{HK}[\rho(\vec{r})] + \int V_{ext}(\vec{r})\rho(\vec{r})d^3\vec{r} \qquad \text{II} - 26$$

In which $V_{ext}(\vec{r})\rho(\vec{r})$ represents the external potential operating on these particles and $F_{HK}[\rho(\vec{r})]$ represents the universal functional of Hohenberg and Kohn. Unfortunately, Hohenberg and Kohn's theorem does not indicate the form of $F_{HK}[\rho(\vec{r})]$. There is no correct formulation for expressing kinetic energy as a functional electron density. The equations of Khon and Sham [13,14] give the only solution to this problem, which is constructed to provide a foundation sufficient to successfully exploit the theorems of Hohenberg and Khon [10].

II-5.6 Khon and Sham equations

Kohn and Sham came up with the concept of thinking about a hypothetical system of N independent electrons in 1965 [13]. Its electron density is the same as that of the actual system of interacting electrons, and its ground state is the Slater determinant created by N ψi orbitals of electrons.

Schrödinger's equation is therefore reformulated in terms of the so-called Kohn-Sham equation [14], a Schrödinger equation with an effective potential in which quasiparticles move. The Kohn-Sham equations are coupled by the electron density $\rho(r) = \sum_i \psi_i(r)^* \psi_i(r)$ coupling included in the solution obtained iteratively. Different bases can be used for orbital expansion in terms of a wave function basis. Once this choice has been made, the orbitals are used to find a better ρ density through a self-coherent cycle. Kohn and Sham have shown that the true density is given by the self-consistent solution of the set of one particle Schrödinger type equations, known as the Kohn and Sham equations:

$$-\left\{\frac{1}{2}\nabla^2 + V_{KS}(r)\right\}\psi_i(r) = \varepsilon_i\psi_i(r) \qquad \text{II} - 27$$

$$\rho(r) = \sum_{occup} |\psi_i(r)|^2 \qquad \text{II} - 28$$

$$V_{KS} = V_{ext}(r) + V_H(r) + V_{XC}(r) \qquad II-29$$

With:

V_{XC}: The exchange and correlation potential given by:

$$V_{XC}(r) = \frac{\partial E_{XC}[\rho(r)]}{\partial \rho(r)} \qquad II-30$$

$V_{ext}(r)$: Represents ionic potential.

$V_H(r)$: Represents the Hartree term given by:

$$V_H(r) = \int \frac{\rho(\vec{r}')}{|\vec{r}-\vec{r}'|} d^3\vec{r} \qquad II-31$$

The following equation is used to solve the Kohn and Sham equations and determine total energy:

$$E(\rho) = \sum_{ioccup} \varepsilon_i - \int \frac{\rho(r)\rho(r\prime)}{|r-r\prime|} dr dr' + E_{XC}(\rho) - \int V_{XC}(r)\,\rho(r)\,dr \qquad II-32$$

II-6 Different types of functional

II-6.1 Generalized gradient approximation (GGA)

Each volume unit's contribution to the system's exchange correlation energy under GGA [15] is determined by both the local density inside that volume and the density within the other nearby volumes. Thus, both the electron density and its gradient will be used to express the exchange-correlation energy.

$$E_{XC}^{GGA}[\rho(r)] = \int f_{XC}^{GGA}[\rho(r), \nabla\rho(r)] d^3r \qquad II-33$$

Where f_{XC}^{GGA} is a functional of the local density and its gradient, dependent on the electron density and its gradient.

II-6.2 B3LYP hybrid functional

In order to better represent the ground state energetics of tiny molecules, the B3LYP hybrid density functional [16,17] was developed. For calculating atomization enthalpies, geometries, and vibrational frequencies, it has now been shown to be significantly more reliable than the local density approximation (LDA) and generalized gradient approximation (GGA)

functionals [18,19]. LDA and GGA computations on solids, primarily transition metal oxides, which are prototypes of Mott insulators, are unable to accurately recreate some particular features due to the significant Coulomb barrier between the two 3d electrons on the transition metal ions [20]. For strongly correlated insulators, the appropriate ground states can be predicted by the straightforward Hartree-Fock (HF) approximation since there is no self-interaction. However, because correlations are not properly treated, the energy gaps and magnetic moments are consistently overestimated. The B3LYP hybrid functional combines the GGA energy functional with the nonlocal Hartree-Fock (HF) exchange. Here, the Lee-Yang-Parr correlation energy [16] is used in place of the Perdew-Wan [21] gradient-corrected correlation energy that was used in Becke's initial work [17]. One way to express the exchange-correlation energy functional is:

$$E_{xc} = (1 - A)(E_x^{LDA} + BE_x^{Becke}) + AE_x^{HF} + (1 - C)E_c^{VWN} + CE_c^{LYP} \qquad \text{II} - 34$$

Where E_x^{HF} is the precise nonlocal HF exchange energy and the local density functional of Vosko, Wilk, and Nusair is used for LDA Ex and Ec VWN [22]. LYP Ec and Becke Ex denote the Lee-Yang-Parr and Becke's gradient corrections for the correlation and local exchange energies, respectively. A linear least-squares fit of the thermochemical properties of chosen atoms and molecules to the trials was used to determine the weight coefficients for the gradient correlated correlation energy, local exchange energy, and the precise HF exchange components. Theoretical results are consistent with experiments when 20% of the exact HF exchange energy is included in the exchange correlation energy. B (exchange weight of the non-local half of the exchange), C (weight of the non-local correlation), and A (Fock exchange percentage) have optimal values of 0.20, 0.9, and 0.81, respectively.

II-7 Self-consistency in calculations

Calculations are made simpler by solving the Kohn-Sham equations for high-symmetry sites in the first Brillouin zone. Then, using a self-consistent iteration cycle shown in the flowchart in Figure II-1, these equations are solved iteratively. The first iteration begins with a test density ρ_{in}. A superposition of atomic densities is usually used, after which the matrix of (K-S) is calculated. The new density ρ_{out} is then calculated by solving the equations for the expansion coefficients to yield the orbitals of (K-S). We go back to the initial stage and combine the two charge densities, ρ_{in} and ρ_{out} as follows if the density or energy has changed substantially (convergence criterion):

$$\rho_{in}^{i+1} = (1-\alpha)\rho_{in}^{i} + \alpha\rho_{out}^{i} \qquad II-35$$

i: represents the iteration.

α: A mixing parameter.

In this way, the iterative procedure can be continued until convergence is achieved. The diagram below can represent this procedure.

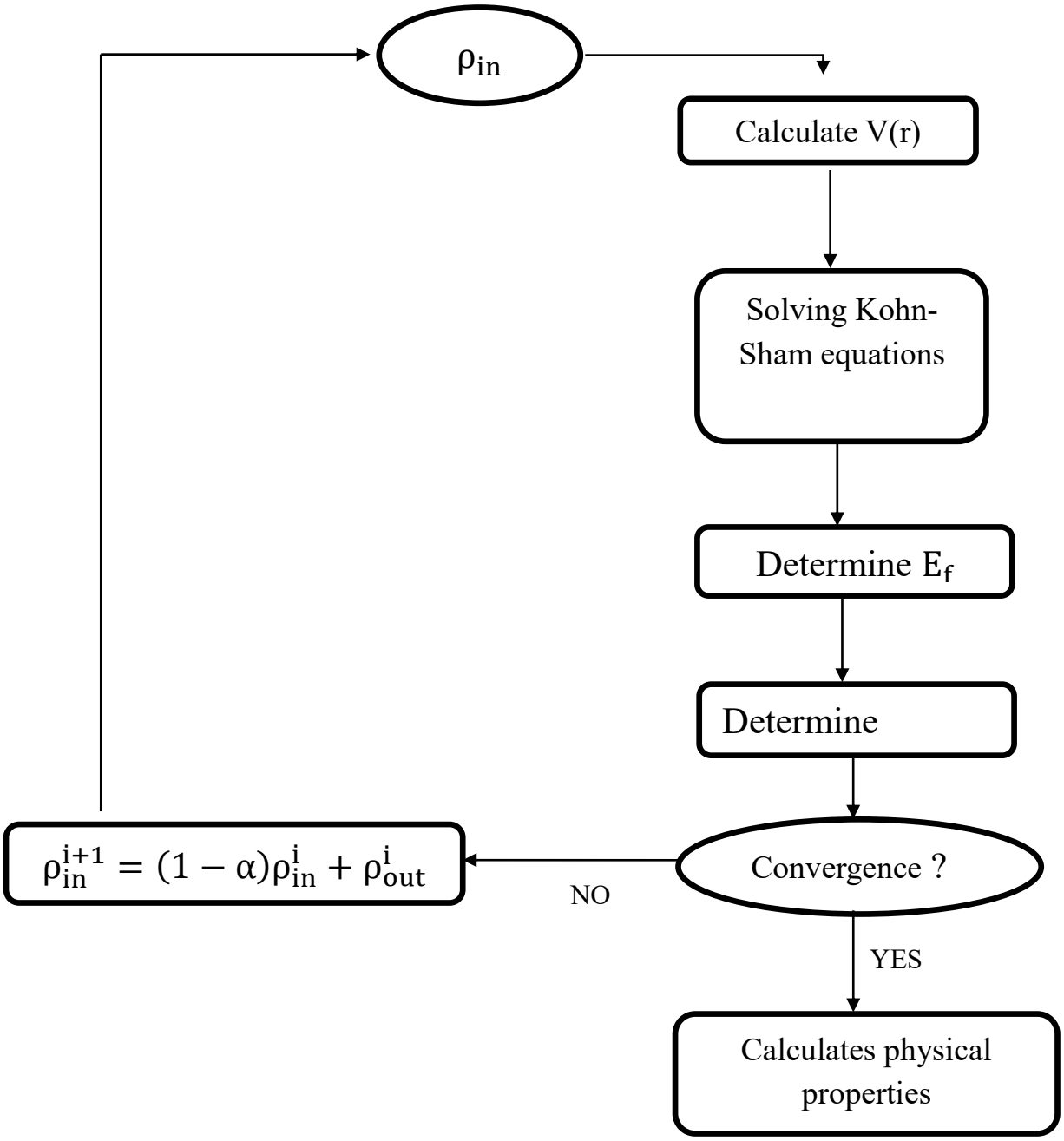

Figure II- 1: Self-consistency cycle of density functional theory (DFT).

II-8 Method of calculation

II-8.1 Pseudopotential method

Many electrical layers surround the atoms that make up a crystal or a molecule. The external environment has very little effect on the electrons in the layers closest to the nucleus. On the other hand, the outer-layer electrons are especially sensitive. Since the environment has no effect on the electrons in the inner layers, simulating the behavior of the external electrons is sufficient to represent the behavior of an atom.

This concept of pseudopotentials is understood [23,24]. We then designate as "valence" electrons, the electrons in the outer layers that will be explicitly simulated in the calculation, and as "core" electrons, the electrons trapped in the pseudopotential. Although it doesn't directly affect them, the environment influences these core electrons. They mainly have two effects: to filter the charge of the nucleus the sum of the charges of the protons and core electrons in the outer layers, far from the nucleus, represents the apparent charge of the nucleus, and to produce elevated oscillations in the electron wave functions of the upper layers. The electronic wave functions must be orthogonal to each other to satisfy the Pauli Exclusion Principle.

The number of nodes in their wave functions increases with the number of electrons in higher layers. Their wave functions will have a huge number of nodes, the higher the electrons are in the layers. As can be observed in Figure II-2, the pseudopotentials must thus have the softest feasible effective potential while simulating the effects of the core electrons (eigenstate energies, scattering qualities). Moreover, the numbers "all electrons" and "pseudo" must be the same beyond a cut-off radius r_c specified during the pseudopotential's formation. The computation will be completed more quickly because of the use of pseudopotentials, since:

- Due to there are fewer electrons to process, the computation is completed more quickly.
- Due to there are fewer degrees of mobility (the core electrons are "frozen"), the convergence process proceeds more quickly and efficiently.

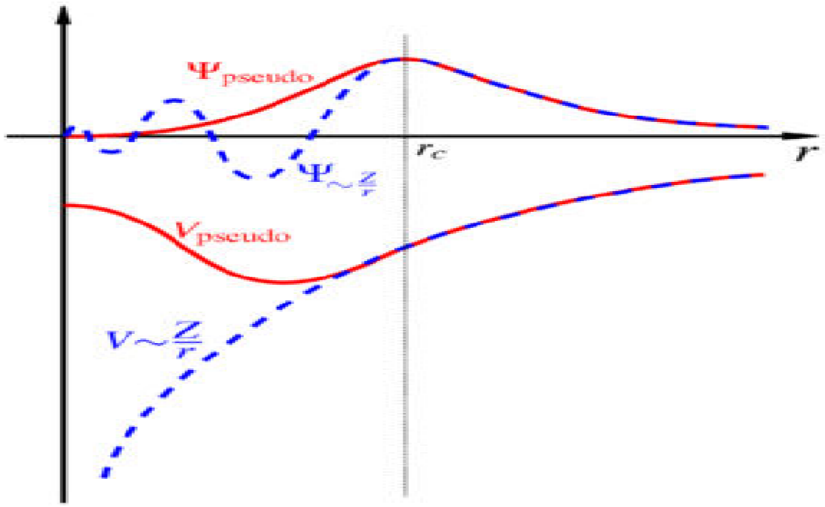

Figure II- 2: Schematic illustration of the formation of the pseudopotential [23].

There are four basic categories of pseudopotentials, and each has its own advantages and disadvantages:

- Conserved norm pseudopotentials introduced by Hamann et al [25].

- The ultra-soft pseudopotentials introduced by Vanderbilt [26].

- Dual-space Gaussian pseudopotentials were introduced by Geodecker et al [27].

- The projected pseudopotentials PAW, an acronym of the English, which does not conserve the norm [28].

The CASTEP computational code was utilized to implement norm-conserving pseudopotentials due to its numerical implementation and ease of use. We will discuss this kind of pseudopotential in the next section.

II-8.2 Conserved norm pseudopotentials

There has been a significant evolution in the effectiveness of pseudo potential, driven by the objectives that follow:

- For the pseudopotential to represent the pseudo wave function with the least amount of plane waves, it must be as soft as feasible.
- The pseudopotential generated for a particular atomic configuration must precisely replicate other configurations to be considered transferrable. This guarantees that the final product, a solid whose crystalline potential differs from that of a single atom, will be acceptable.

- The charge density created using the pseudo-function must extremely precisely replicate the valence charge density created with the genuine wave function.

The pseudopotential from the fundamentals of atomic calculation, Hamann, Schluter, and Chiang (H-S-C) [8], started a revolution in this subject. The H-S-C method requires that the charge contained in the core region converge identically to the actual charge in this region; for this reason, this type of pseudopotential is called norm conserving. Additionally, the results provided by the method must agree with those of the calculation involving all electrons, not only for the valence eigenvalues but also for the valence wave functions beyond the core region. This final need appears to be necessary to get a high quality [29] pseudopotential.

The pseudopotential and pseudo wave functions are produced using the idea of norm conservation to equalize the potential outside of the r_c radius around the atom and the wave function, respectively. Equivalent to the potential surrounding the atom outside of the r_c radius. The valence wave function and the pseudo-function are distinct inside r_c, but their norms are conditioned to be the same.

II-8.3 Plan waves method (PW)

Since plane wave bases provide the opportunity to increase the dimensions of the calculations and thus improve the convergence of the structural calculations, they are heavily utilized in electronic structure calculations. Because of its total independence from atomic locations, the plane wave foundation is especially well suited for periodic systems. The dimension of the systems under study is, in fact, one of the primary issues with numerical computation. The systems under study in most physical problems have one or more dimensions (wire, surface, solid) that can be considered limitless. The problem is statistically unsolvable due to the unlimited quantity of electrons present in the system. To solve this issue, we need to revisit periodic systems and, consequently, Bloch's theorem, which is essential to solid-state physics.

II-8.4 Bloch's theorem and plane wave basis

A thorough foundation of Fourier coefficients can be obtained by deconstructing any periodic function. Bloch's theorem allows the wave function to be stated as follows:

$$\Psi_{nk}(\mathrm{r}) = u_{nk} e^{ikr} \qquad \mathrm{II}-36$$

Where n is the band index and u_{nk} is a lattice periodic function. The kinetic energy term is diagonal in the Hamiltonian matrix, whereas the potentials are non-diagonal terms. The Fourier coefficients of the potentials are used to express them. Nevertheless, there is no way to determine the eigenvalues. The Hamiltonian matrix is known as a "dominant diagonal" when it is constructed so that, at a given point, the potential may be roughly reduced to zero, with diagonal terms rising and non-diagonal terms falling. Then, by reducing the infinite matrix to a finite matrix and computing the eigenvalues, the first electronic energy bands are identified. Finite sums over all vectors are obtained by trimming the expansion, where k is any vector in the first Brillouin zone.

II-9 CASTEP calculation code

Many computational codes, like Dmol3 [30], VASP [31], ABINIT [32], CRYSTAL [33], and BigDFT [34], are based on DFT. The numerical modeling program CASTEP (Cambridge Serial Total Energy Package) was developed in 1988 by Payne et al [35,36]. It will be used in this study. This code is an ab initio computation and part of the Material Studio numerical simulation package that Accelrys © sells.

Using supercells, integration across the Brillouin zone, a plane wave basis, and pseudopotentials, CASTEP uses DFT to solve the Schrödinger equation under periodic conditions in order to determine the total energy of a given system. Bloch's theorem and periodic boundary conditions are used to build the electron wave functions on a plane wave basis. The electron-ion potential is described by use of two kinds of ab initio pseudopotentials: ultra-soft and norm-conserving pseudopotentials. Direct energy minimization methods are used to obtain the electronic wave functions and the associated charge density. Only the Kohn-Sham orbitals with G vectors pertaining to the irreducible part of the Brillouin zone are determined since the electron density can only be produced from these states through a symmetrization step that uses the space group matrices. A symmetrisation step is also necessary for the pressure and stress computations. Consequently, the electron density exhibits unambiguous symmetry. Symmetrization greatly cuts down on computation time since CASTEP is efficiently parallelized based on k-points, particularly for tiny meshes with a large number of k-points. As stated earlier, the Monkhorst-Pack method is used by CASTEP to sample the Brillouin zone [37]. This method creates a uniform grid along reciprocal space's three axes. Utilizing the symmetry of the system, the primitive cell's k-point count is decreased. The underlying

symmetry of atomic forces and the stress tensor, which affect atomic displacements and modifications in crystal lattice properties, is evident.

II-9.1 Definition of some parameters

II-9.1.1 Cut-off energy

Represents a stopping criterion that is consistent with kinetic energy error minimization. A sphere in reciprocal space, which is defined in terms of the cutoff energy E_{cut}, bounds the plane wave set, bound the plane wave set. For example:

$$\frac{\hbar^2}{2m}\left|\vec{K}+\vec{G}\right|^2 \prec E_{cut} \qquad II-37$$

II-9.1.2 k points grids

It is postulated that the eigenvalues of the Hamiltonian must be calculated at an infinite number of k places in order to determine the total energy of the system. The symmetries can already simplify the situation. Since the regeneration of the entire BZ is made possible by symmetry methods, the problem can be limited to the irreducible Brillouin zone (IBZ). On the other hand, the points that are taken into account are always infinitely close to each other. Monkhorst and Pack [37] proposed a method to approximate the integral on a finite three-dimensional grid of k points. Since the wave functions do not change drastically around a k-point, the basic premise is that information over an entire region of the BZ may be reduced to a single location. As a result, the integrals will be reduced to discrete sums, necessitating the determination of the eigenvalue on a limited set of locations [22].

II-10 Conclusion

The techniques that will be applied during this investigation are included in this chapter. The DFT formalism serves as the foundation for this approach to computing electronic structures. We also demonstrated that the DFT theory was based on the basis of the potential in conjunction with plane waves (PP-PW). Several approximations are necessary for the DFT to be feasible in atomistic simulations, such as the size of the wave base and the mesh of the initial Brillouin zone, which are difficult to alter throughout computations. The CASTEP calculation code facilitates the implementation process.

References

[1] C. Dupas, *Physique de l'état solide*, 5e éd., [nouveau tirage] (Dunod, Paris, 1990).

[2] M. Born and R. Oppenheimer, Ann. Phys. **389**, 457 (1927).

[3] D. R. Hartree, Math. Proc. Camb. Philos. Soc. **24**, 89 (1928).

[4] V. Fock, Z. F�r Phys. **61**, 126 (1930).

[5] W. Pauli, in *Quantentheorie* (De Gruyter, 1969), pp. 229–253.

[6] J. C. Slater, Phys. Rev. **81**, 385 (1951).

[7] J. C. Slater, Phys. Rev. **34**, 1293 (1929).

[8] L. H. Thomas, Math. Proc. Camb. Philos. Soc. **23**, 542 (1927).

[9] E. Fermi, Z. F�r Phys. **48**, 73 (1928).

[10] P. Hohenberg and W. Kohn, Phys. Rev. **136**, B864 (1964).

[11] N. H. March, *Electron Density Theory of Atoms and Molecules* (Academic Press, London, 1992).

[12] P. A. M. Dirac, Phys. Rev. **139**, B684 (1965).

[13] W. Kohn and L. J. Sham, Phys. Rev. **140**, A1133 (1965).

[14] W. Kohn, Rev. Mod. Phys. **71**, 1253 (1999).

[15] J. P. Perdew and Y. Wang, Phys. Rev. B **45**, 13244 (1992).

[16] C. Lee, W. Yang, and R. G. Parr, Phys. Rev. B **37**, 785 (1988).

[17] A. D. Becke, J. Chem. Phys. **96**, 2155 (1992).

[18] L. A. Curtiss, K. Raghavachari, P. C. Redfern, and J. A. Pople, J. Chem. Phys. **106**, 1063 (1997).

[19] L. A. Curtiss, K. Raghavachari, P. C. Redfern, and J. A. Pople, Chem. Phys. Lett. **270**, 419 (1997).

[20] H. Wich, Krist. Tech. **10**, (1975).

[21] P. Ziesche and Technische Universität Dresden, editors , *Electronic Structure of Solids '91: Proceedings of the 75. WE-Heraeus-Seminar and 21st Annual International Symposium on Electronic Structure of Solids Held in Gaussig (Germany), March 11 - 15, 1991 ; with 19 Tables*, 1. ed (Akad.-Verl, Berlin, 1991).

[22] S. H. Vosko, L. Wilk, and M. Nusair, Can. J. Phys. **58**, 1200 (1980).

[23] D. R. Hamann, M. Schlüter, and C. Chiang, Phys. Rev. Lett. **43**, 1494 (1979).

[24] M. T. Yin and M. L. Cohen, Phys. Rev. B **25**, 7403 (1982).

[25] P. E. Blöchl, Phys. Rev. B **50**, 17953 (1994).

[26] D. Vanderbilt, Phys. Rev. B **41**, 7892 (1990).

[27] N. Troullier and J. L. Martins, Phys. Rev. B **43**, 1993 (1991).

[28] E. Anderson, editor , *LAPACK Users' Guide*, 3rd ed (Society for Industrial and Applied Mathematics, Philadelphia, 1999).

[29] E. O. Kane, J. Phys. Chem. Solids **1**, 249 (1957).

[30] B. Delley, J. Chem. Phys. **92**, 508 (1990).

[31] G. Kresse and J. Furthmüller, Comput. Mater. Sci. **6**, 15 (1996).

[32] X. Gonze, J.-M. Beuken, R. Caracas, F. Detraux, M. Fuchs, G.-M. Rignanese, L. Sindic, M. Verstraete, G. Zerah, F. Jollet, M. Torrent, A. Roy, M. Mikami, Ph. Ghosez, J.-Y. Raty, and D. C. Allan, Comput. Mater. Sci. **25**, 478 (2002).

[33] R. Dovesi, F. Pascale, B. Civalleri, K. Doll, N. M. Harrison, I. Bush, P. D'Arco, Y. Noël, M. Rérat, P. Carbonnière, M. Causà, S. Salustro, V. Lacivita, B. Kirtman, A. M. Ferrari, F. S. Gentile, J. Baima, M. Ferrero, R. Demichelis, and M. De La Pierre, J. Chem. Phys. **152**, 204111 (2020).

[34] L. Genovese, M. Ospici, T. Deutsch, J.-F. Méhaut, A. Neelov, and S. Goedecker, J. Chem. Phys. **131**, 034103 (2009).

[35] M. D. Segall, P. J. D. Lindan, M. J. Probert, C. J. Pickard, P. J. Hasnip, S. J. Clark, and M. C. Payne, J. Phys. Condens. Matter **14**, 2717 (2002).

[36] V. V. Pogodina, Acta Virol. **19**, 509 (1975).

[37] H. J. Monkhorst and J. D. Pack, Phys. Rev. B **13**, 5188 (1976).

Chapter III: Results and discussion

III-1 Introduction

There are three known polymorphs of CdSe, which correspond to hexagonal and cubic structures: wurtzite, sphalerite, and rock salt. Because Zn and Cd belong to the same group in the periodic table, their chalcogenides have structural similarities. The zinc-blende or wurtzite structure is where cadmium and zinc chalcogenides crystallize under ambient conditions. Under pressure, they transform into the rock-salt phase and then the β-Sn phase. Complex structural changes in the high-pressure phases of several III–V and II–VI compounds have been identified using X-ray diffraction techniques. About 60 years ago, Edwards and Drickamer [1] conducted the first experimental study of pressure-induced phase transitions in CdS and CdSe. Notably, the high-pressure phase sequence seen in sulfides and selenides is very different from that of tellurides. Later, angle-dispersive X-ray (ADX) analysis of CdSe was carried out by Nelmes and McMahon [2] up to 85 GPa. A continuous shift from the NaCl structure to the Cmcm structure was observed in their results at 27.0 GPa. At 36 GPa, there was also evidence of a further transformation into a deformed Cmcm structure. Moreover, unlike the other two chalcogenides, mercury chalcogenides (HgSe) exhibit distinct behavior. The ground state structure of HgS is the cinnabar phase. Comes before the rock salt structure. The ambient pressure phase of HgS was initially identified as the cinnabar phase. The similar characteristics of HgSe and HgTe in the zinc-blende (B3) phases drive the cinnabar (B9) structure at low pressure (2 GPa) [3,4]. The cinnabar (B9) structure is driven by the similar characteristics of HgSe and HgTe in the zinc-blende (B3) phases. Furthermore, it is generally known that ScS and ScSe have a rock salt (B1) structure under ambient conditions [5,6]. The structural properties and high-pressure structural phase transition from NaCl (B1) to CsCl (B2) have been documented by Maachou et al. [7] and Purvee Bhardwaj et al. [8]. Moreover, Ahmad et.al [9] have identified the structural parameters and the structural phase transitions from NaCl type (B1) to CsCl type (B2) and ZnS type (B3) under high pressure, as well as the optical parameters, electrical properties, and thermal characteristics of scandium chalcogenides, namely ScX (X=S, Se, Te). Furthermore, manganese selenide also displays polymorphism with three known phases: rock salt (α), zinc-blende (β), and wurtzite (γ). Among these, the α phase (rock salt) is the most thermodynamically stable due to its reduced band gap and electrical conductivity. In contrast to the metastable γ-phase, the β-phase is extremely unstable and only occurs as an impurity." The γ-phase is hexagonal in manganese selenide, whereas the α and β phases are cubic [10].

The aim of this chapter is to examine the characteristics of the CdSe and MnSe in both rock salt and zinc-blende structures, the HgSe in both trigonal (cinnabar) and zinc-blende phases, and the ScSe in both NaCl and CsCl types. The study is divided into two sections. The first section investigates the ground-state properties, while the second section focuses on the high-pressure phases of the studied compounds. The study focuses on a comprehensive set of characteristics, including, the lattice parameters, electronic, dynamic, optical and thermodynamic properties, also elastic properties, such as the matrix of elastic constants, and some other variables, such as the shear modulus, Young's modulus, Poisson's ratio, Cauchy pressure and Pugh ratio. The study was conducted under hydrostatic pressure and at zero pressure.

III-2 Method of calculation

In this study, we used first principles pseudopotential plane waves, as implemented in the CASTEP code [11], to calculate the structural, electronic, optical, elastic, and dynamic properties of CdSe and MnSe in both zinc-blende and rock salt structures, HgSe in both zinc-blende and trigonal (cinnabar) phases, and ScSe in both NaCl and CsCl types of structure. The generalized gradient approximation for solids (GGA-PBEsol) functional [12] was used to characterize the exchange-correlation potential. Integrations within the Brillouin zone were performed over a 4×4×4 grid of k-points for CdSe, MnSe, and ScSe in both structures and an 8×8×8 and 8×8×4 grid of k-points for HgSe in the zinc blende structure and cinnabar phase, respectively. A plane-wave basis set with a kinetic energy cutoff of 1350, 800, 1160, and 1160 eV was used for CdSe, HgSe, MnSe, and ScSe, respectively. Norm-conserving pseudopotentials accounted for interactions between valence electrons and ion cores. To calculate the electronic structure, the B3LYP hybrid functional [13] was employed, with a 21×21×21 k-point grid and a 1159 eV energy cutoff for CdSe and MnSe in both structures, and a 19×19×19 k-point grid with an 800 eV energy cutoff for HgSe in the zinc-blende structure. A denser 30×30×30 k-point grid with the same energy cutoff was used for optical properties. Several precise procedures modeled the effect of pressure. First, the Murnaghan equation of state was used to calculate the lattice parameters at each pressure [14], enabling accurate determination of lattice parameters under different pressures. Using these parameters, structures were generated at the specified pressures and self-consistent calculations were performed to ensure convergence. After convergence, the derived properties were determined. The thermodynamic properties of the materials were calculated using the Gibbs2 code [15], within the framework of the quasi harmonic Debye model. This model allows for the calculation of temperature and pressure dependent thermodynamic properties, providing insights into the stability and phase transitions

of CdSe, HgSe, ScSe, and MnSe. This systematic approach offers a comprehensive understanding of the behavior of these materials under varying pressure conditions.

III-3 Ground state properties

III-3.1 Structural properties

In this part, we examine the ground state characteristics of CdSe and HgSe in the zinc-blende (B3) structures with space group F$\bar{4}$3m (216), shown in Figure III-1, In this configuration, Cd (Hg) atoms occupy the 4a (0, 0, 0) positions , while Se atoms occupy the 4c (1/4, 1/4, 1/4) sites. Furthermore, as shown in Figure III-2, ScSe and MnSe are investigate in the rock salt (B1) structure with space group Fm$\bar{3}$m (225), where Sc (Mn) atoms occupy the 4a (0, 0, 0) positions, and Se atoms occupy the 4b (1/2, 1/2, 1/2) sites.

The electronic configuration of atoms:

Se: $[Ar]^{18}$ $3d^{10}$ $4s^2$ $4p^4$.

Cd: $[Kr]^{36}$ $5s^2 4d^{10}$.

Hg: $[Xe]^{54}$ $4f^{14}$ $5d^{10}$ $6s^2$.

Mn: $[Ar]^{18}$ $4s^2$ $3d^5$.

Sc: $[Ar]^{18}$ $4s^2$ $3d^1$.

The schematic representation of this structure is as follows:

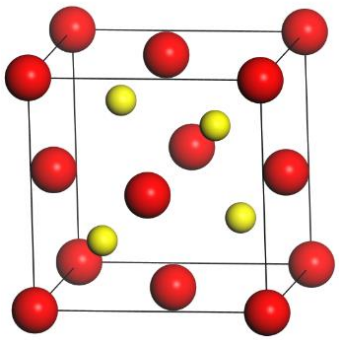

Figure III- 1: Crystalline structure of the zinc-blend (B3) of CdSe and HgSe.

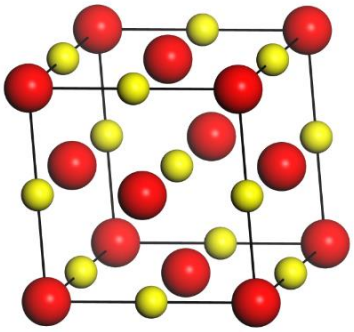

Figure III- 2: Crystalline structure of the rock salt (B1) of ScSe and MnSe.

Figures III-3 and III-4 display the total energy changes as a function of volume E (V) of CdSe and HgSe in the zinc-blende (B3) structure and ScSe and MnSe in the rock salt (B1) structure.

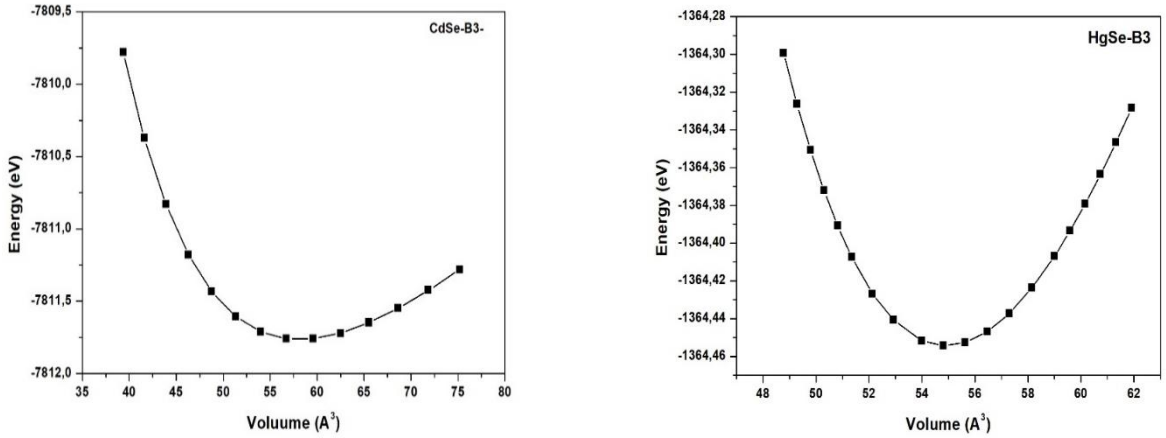

Figure III- 3: Total energy changes as a function of the volume of CdSe and HgSe in the zinc-blende structure.

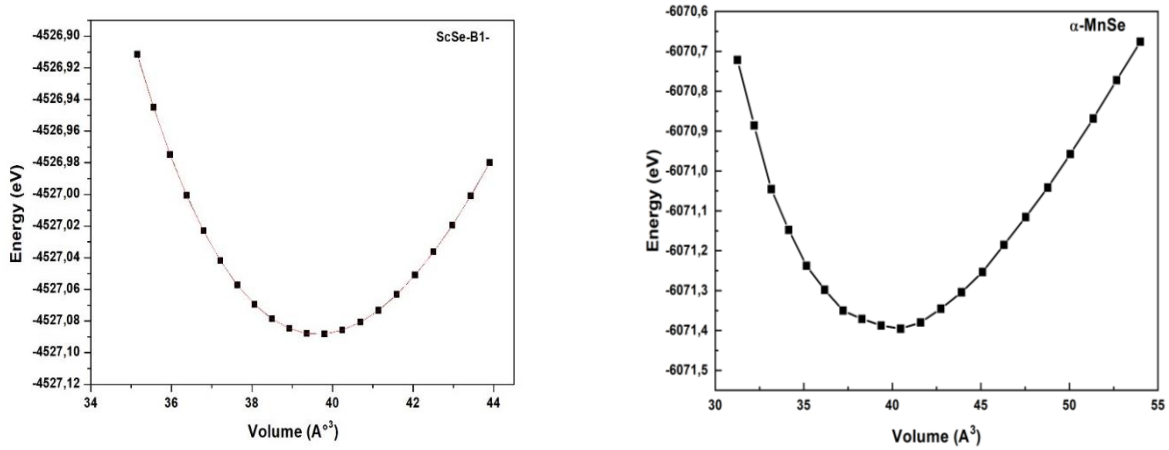

Figure III- 4: Total energy changes as a function of the volume of ScSe and MnSe in the rock salt structure.

Determining the material's structural characteristics is the initial step in a first-principles calculation. We can access attributes that are more physical by understanding this information.

The energy-volume E (V) curves were fitted by the Murnaghan equation of state by to determine the structural parameters of the material's equilibrium state [14], including the lattice parameters (a_0), bulk modulus (B_0), and its pressure derivative (B').

$$E(V) = E_0 + \frac{B}{B'(B'+1)}\left[V\left(\frac{V_0}{V}\right)^{B'} - V_0\right] + \frac{B}{B'}(V - V_0) \qquad \text{III} - 1$$

Where:

E: Total energy.

V: Equilibrium volume.

B: The bulk modulus is provided by the following formula:

$$B = V\frac{\partial^2 E}{\partial V^2} \qquad \text{III} - 2$$

B′: The derivative of modulus of compressibility.

$$B' = \frac{\partial B}{\partial P} \qquad \text{III} - 3$$

Tables III-1, III-2, III-3, and III-4 provide a detailed summary of the results obtained, including a comparison with experimental results from other studies For CdSe, HgSe, ScSe, and MnSe, respectively.

The calculated lattice parameters (a_0) of CdSe is slightly higher than the experimental results, with a deviation of less than 2% from the reported values [16]. However, the value of B_0 of CdSe is in consistent with experimental findings [17]. While the B' show no available experimental results, it agrees well with previous theoretical studies [18]. the computed a_0 for HgSe is an excellent match with experimental results, deviating by just under 1% from references [16,19,20]. The B_0 agrees with experimental findings [16,19]. and B' supports literature [21,22]. For ScSe, the calculated a_0 closely match both experimental results [17] and other ab initio calculations[8,9,23]. although no experimental data are available for the B_0 or its derivative (B'), the obtained values are in line with previous theoretical results[8,9,23]. Similarly, for MnSe, the calculated value a_0 deviate by less within 1% from experimental values [24]. No experimental results are

available for B_0, but the calculated values accord closely with those reported in the literature [25–27].

Table III- 1: Structural properties, including lattice parameters (a_0), bulk modulus (B_0), and its derivative (B′) of CdSe in the zinc-blende structure.

Compound	Parameters	This study	Other calculations	Experiments
CdSe	a_0 (A)	6.156	6.16 [18] 6.04 [18] 6.07 [28]	6.05 [16]
	B_0 (GPa)	49.207	52.4 [18] 46.3 [18] 54.41 [28] 4.2 [29]	53 [16]
	B'	4.238	5.1 [18] 4.5 [18] 4.6652 [30]	

Table III- 2: Structural properties, including lattice parameters (a_0), bulk modulus (B_0), and its derivative (B′) of HgSe in the zinc-blende structure.

Compound	Parameters	This study	Other calculations	Experiments
HgSe	a_0 (A)	6.033	6.115 [31] 6.276 [22] 6.103 [21] 6.287 [21] 6.069 [32] 6.22 [33]	6.074 [34] 6.085 [16] 6.084 [20]
	B_0 (GPa)	57.149	53.93 [31] 42.17 [22] 44.046 [21] 61.22 [21]	57.6 [34] 51.66 [16]
	B'	5.042	5.10 [21] 5.18 [21] 5.21 [22]	2.60 [16]

Table III- 3: Structural properties, including lattice parameters (a_0), bulk modulus (B_0), and its derivative (B′) of ScSe in the rock-salt structure.

Compound	Parameters	This study	Other calculations	Experiments
ScSe	a_0 (A)	5.412	5.4 [23] 5.404 [9] 5.392 [35] 5.510 [36] 5.2435 [37] 5.4759 [38]	5.398 [17]
	B_0 (GPa)	90.213	93.25 [23] 88.64 [9] 95.92 [7] 93.85 [35] 100.1 [37]	
	B'	4.245	3.84 [9] 3.302 [7] 4.18 [37]	

Table III- 4: Structural properties, including lattice parameters (a_0), bulk modulus (B_0), and its derivative (B′) of MnSe in the rock-salt structure.

Compound	Parameters	This study	Other calculations	Experiments
MnSe	a_0 (A)	5.413	5.398 [25] 5.2045 [26]	5.45 [24]
	B_0 (GPa)	76.064	66.8 [25] 65.7 [26] 86.18 [27]	
	B'	4.521	3.93 [25] 4.09 [27]	

III-3.2 Electronic properties

In solid-state physics, a band provides a fundamental framework for understanding the behavior of electrons in crystalline materials. It describes the distribution of allowed energy states, where the dispersion relation E(K) connects energy (E) to crystal momentum (K). This relationship governs the material's electronic properties that will, in turn, affect its transport, thermal, optical, and mechanical properties.

Investigating band structures is crucial because it indicates whether a material is metallic, semiconducting, or insulating. The presence of a band gap between the valence and conduction bands generally indicates semiconducting or insulating properties, whereas overlapping bands suggest metallic conductivity. The distinction between direct and indirect band gaps is crucial to a material's optical response.

The density of states (DOS) complements the band structure by quantifying the number of available electronic states at each energy level. This enables the identification of the dominant orbital contributions near the Fermi level and facilitates understanding of hybridization among atomic orbitals. Together, the band structure and DOS provide a complete

picture of the system's electrical characteristics, offering vital insight into the type of bonding, charge distribution, and potential functional applications.

In the current investigation, we examine the band structures of the considered materials. The first Brillouin zone of the FCC structure is displayed in Figure III-5, which defines the high symmetry directions along which the band structures.

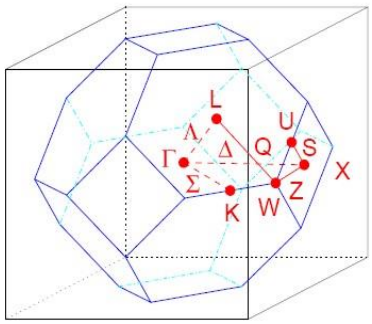

Figure III- 5: The first Brillouin zone of FCC structures represents the energy along high symmetry lines.

III-3.2.1 Band structure

To determine the energy band structures of CdSe and HgSe in the zinc-blende structure, as well as of ScSe and MnSe in the rock-salt structure, we used the GGA-PBEsol with previously optimized structural parameters. The high-symmetry directions of the first Brillouin zone were employed to calculate the band dispersions. Figure III-6 shows the resulting band structures.

The valence band maxima (VBM) and conduction band minima (CBM) for CdSe are both located near the Γ point, indicating a direct band gap (Γ-Γ). The estimated band gap of 1.1eV agrees well with previous theoretical predictions using the GGA and LDA approximations [39,40], although it is lower than the experimental values reported in [16,41,42]. Furthermore, for HgSe, the VBM and CBM also lie at the Γ point. However, the system exhibits semi-metallic behavior (0 eV) within GGA, in agreement with both theoretical and experimental findings [21,31,43]. Moreover, ScSe shows metallic behavior with no energy gap because the CBM are situated below the Fermi level; these results are similar to those found in other literature [35–37]. Furthermore, both spin channels (spin-up and spin-down) show metallic behavior for MnSe. In the spin-down channel, the CBM lies below the Fermi level, whereas in the spin-up channel, both the VBM and the CBM intersect the Fermi level. Table

III-5 presents the results comparing CdSe and HgSe in the zinc blende structure, as well as ScSe and MnSe in rock salt structures, calculated using the GGA-PBEsol approximation.

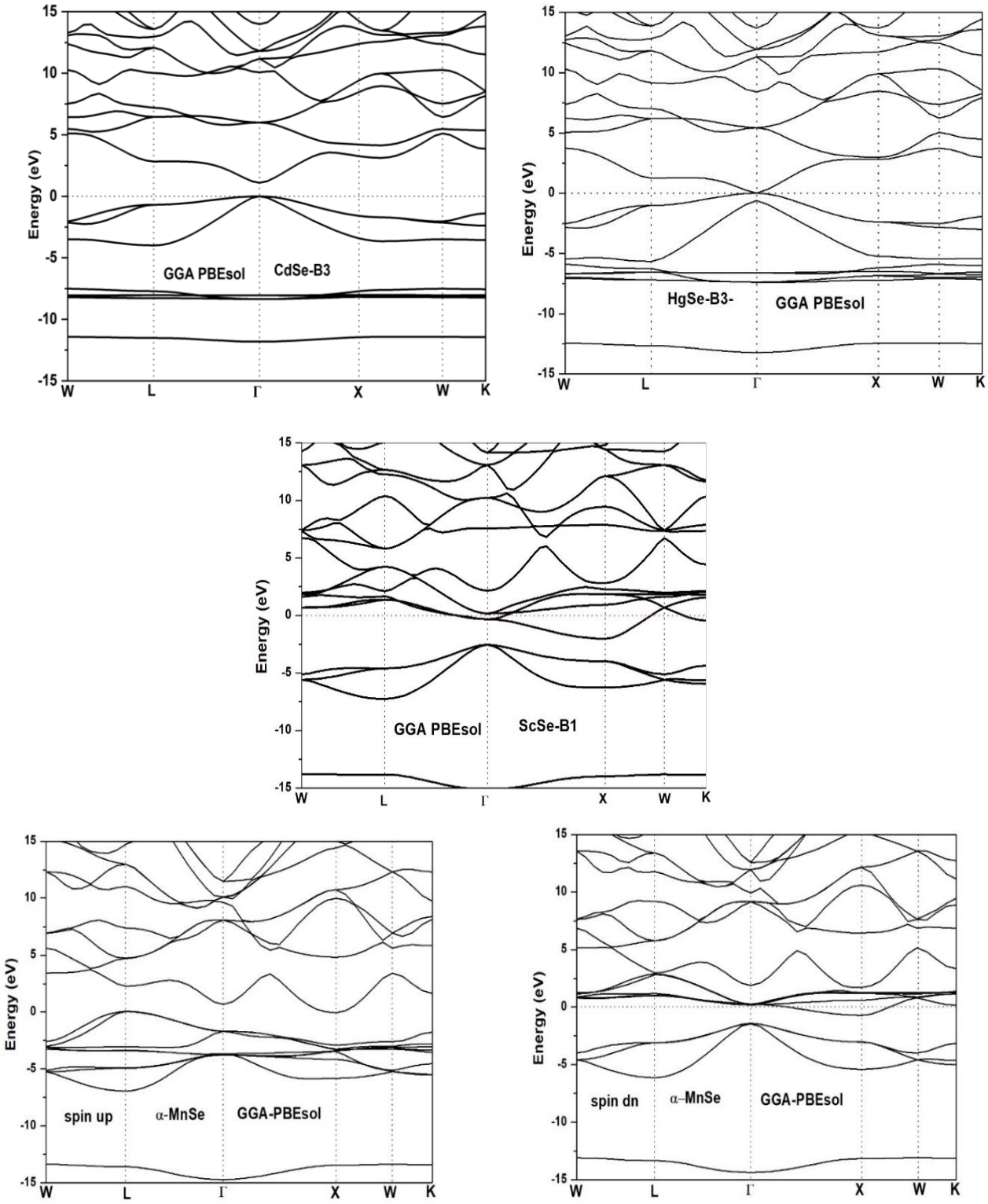

Figure III- 6: Band structure of CdSe, HgSe, ScSe and MnSe obtained by GGA-PBEsol.

Table III- 5: Fundamental gap energy of CdSe, HgSe, ScSe and MnSe obtained using GGA-PBEsol.

Compounds		This study (eV)	Other calculations	Experiments
CdSe		1.1	2.092 [18] 0.95 [39] 1.08 [40]	1.90 [16] 1.69 [41] 1.82 [42]
HgSe		0	0 [21,43,44]	0.024 [37]
ScSe		0	0 [7,35–38]	
MnSe	Spin up	0	0.03 [45]	2.0 [46]
	Spin dn	0		

III-3.2.2 Density of states

The electronic structures of CdSe and HgSe in the B3 structure, and of ScSe and MnSe in the B1 structure, are better understood using the density of states (DOS), which shows the number of electronic states per atom of energy. The contributions of each orbital PDOS (partial state densities) and atom TDOS (total state density) are shown by these curves. Therefore, we employed the GGA PBE-sol approximation for the method (PP-PW) to calculate the total and partial state densities for CdSe, HgSe in the zinc blende (B3) structure, as well as ScSe and MnSe in the rock salt (B1) structure. It is displayed in Figure III-7.

For CdSe, the valence band is divided into four distinct regions. Se-s states are the source of the first peak, which is situated -12.5 eV below the Fermi level. Cd-d orbitals dominate the second region, which is close to -7.5 eV. There is a mixed contribution from Cd-s and Se-p states in the third region, centered around -3.5 eV. Lastly, Se-p states are primarily responsible for the fourth peak at about -1.5 eV. Cd-p states made up the majority of the conduction band, with Cd-s orbitals contributing only slightly. In HgSe, four distinct bands are also evident. The first region at ~-13.5 eV corresponds to Se-s states, above which lies the Hg-d band, with a small contribution from Se-p around -7.5 eV. The third region, centered around -6 eV, is a hybrid of Se-p and Hg-s orbitals. The fourth region, located at -5 eV, is composed of Se-p states. The conduction band mainly comprises Se-p orbitals, with a small contribution from Se-s orbitals. Additionally, the lowest energy bands (~ –15 eV) arise from Se-s orbitals, while the valence region near –5 eV includes Se-p states, with slight mixing from Hg-d orbitals. These features are consistent with the observed semi-metallic nature of HgSe. Furthermore, for ScSe, the DOS reveals a pronounced metallic character, which originates from the Sc-d states crossing the Fermi level. Hybridization with Se-p states also contributes to the valence region,

but the dominant contribution near the Fermi level arises from Sc-d orbitals. Strong spin polarization is evident for MnSe. The lowest states in the spin-up channel are Se-s orbitals near –13.5 eV, followed by a region centered around –7.5 eV that is dominated by Mn-d orbitals with a small contribution from Se-p states. Conversely, Se-p orbitals make up the majority of the equivalent spin-down region. The Se-p states and a small contribution from spin-up Mn-d orbitals close to the Fermi level are the sources of MnSe's metallicity. In the spin-down channel, the conduction band is mainly made up of Mn-d states, whereas in the spin-up channel, it is dominated by Se-p orbitals with minor Se-s contributions.

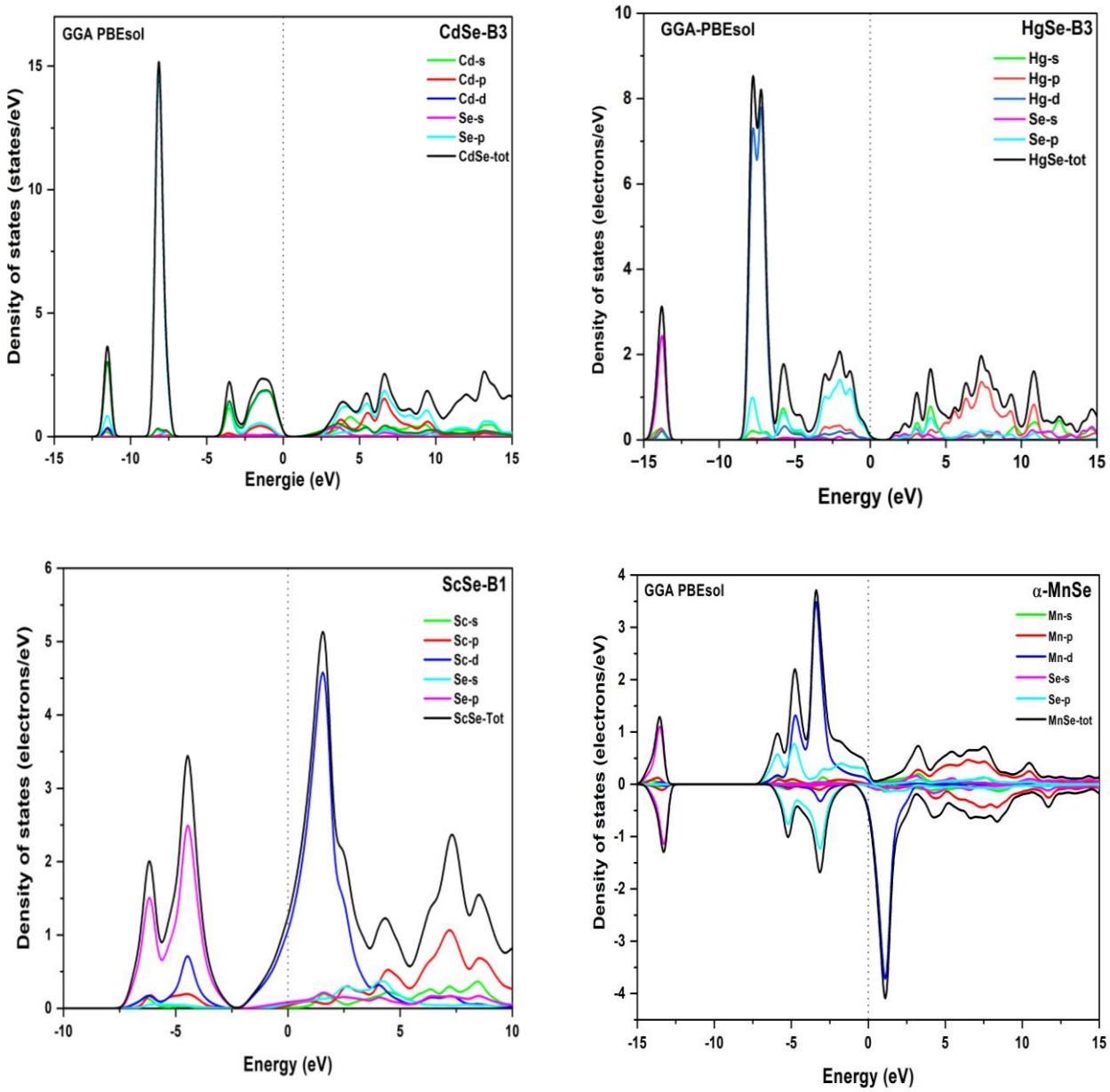

Figure III- 7: Total and partial density of states of CdSe, HgSe, ScSe and MnSe obtained by GGA-PBEsol.

III-3.3 Effect of exchange correlation

III-3.3.1 Band structure

Figure III-8 displays the electronic band structures of CdSe and HgSe in the zinc-blende (B3) structure, ScSe, and MnSe in the rock-salt (B1) structure generated by B3LYP.

For CdSe, both VBM and CBM occurs at the Γ point, yielding a direct band gap (Γ-Γ). The estimated band gap of 2.44 eV is larger than the experimental values reported in [16,41,42] and also exceeds previous hybrid functional results [18,47,48]. In addition, the B3LYP results for HgSe differ from the GGA PBE-sol, suggesting a semiconducting nature as opposed to a semi metallic one. Both the VBM and the CBM can be found at the Γ point, corresponding to a direct band gap of 0.14 eV. This gap is higher than the experimental value [49] and also higher than those of other ab initio studies [31,43,50]. Moreover, for ScSe, the B3LYP calculation confirms a metallic character, with no band gap since the CBM lies below the Fermi level. These findings are consistent with earlier theoretical studies [7,35–38]. Furthermore, a more complex behavior is observed due to spin polarization for MnSe. In the spin up channel, the system showing as indirect band gap (L-X) of 1.58 eV. Whereas a direct band gap (Γ-Γ) of 2.96 eV is seen in the spin-down channel.

Table III-6 lists the results comparing CdSe and HgSe in the B3 structure, as well as ScSe and MnSe in the B1 structure, calculated using the B3LYP hybrid functional.

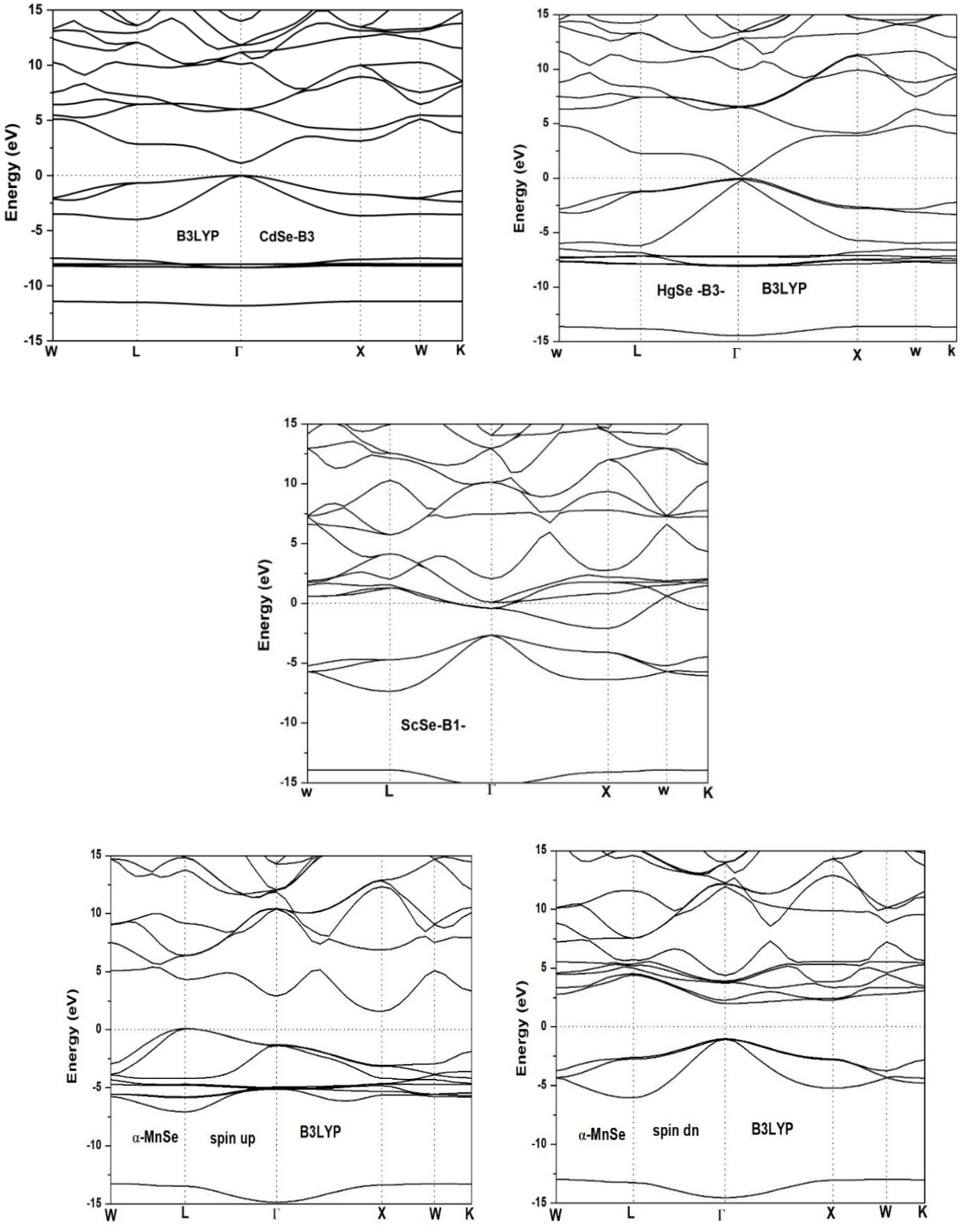

Figure III- 8: Band structure of CdSe, HgSe, ScSe and MnSe obtained by hybrid functional B3LYP.

Table III- 6: Fundamental gap energy of CdSe, HgSe, ScSe, and MnSe obtained using hybrid functional B3LYP.

Compounds		This study (eV)	Other calculations	Experiments
CdSe		2.400	1.8845 [48] 1.84 [47] 2.092 [18]	1.90 [16] 1.69 [41] 1.82 [42]
HgSe		0.140	0.035 [43] 0.07 [50] 0.01 [31]	0.024 [49]
ScSe		0	0 [7,35–38]	
MnSe	Spin up	1.580	0.03 [45]	2.0 [46]
	Spin dn	2.960		

III-3.3.2 Density of states

We computed both the total (TDOS) and partial (PDOS) densities for CdSe and HgSe in the B3 structure, as well as ScSe and MnSe in the B1 structure. The results are presented in Figure III-9. Four distinct peaks are clearly visible For CdSe. The first peak appears approximately -12.5 eV above the Fermi level and originates entirely from Se-s orbitals. The second feature, centered around -7.5 eV, corresponds to the Cd-d orbitals. The third peak is composed entirely of the Se-p and Cd-s orbitals located around -3.5 eV, the fourth peak is made up entirely of Se-p orbitals at -1.5 eV, and the conduction band is primarily made up of the Cd-p orbitals, with a minor contribution from the Cd-s orbitals. Moreover, for HgSe, the presence of four distinct regions is clearly visible. The Se-s states make up the first region, which is situated -13.5 eV below the HgSe Fermi level. The band of the Hg-d is located above this zone, with a small contribution from the Se-p, which is situated around -7.5 eV. The third region is made up of the Se-p and Hg-s, which are allocated in -6 eV, and the fourth region is made up of only Se-p orbitals, which are allocated around -5 eV with a minor contribution from the Se-s, the Se-p orbitals make up the majority of the conduction band. Furthermore, for the rock salt structure of ScSe, With significant hybridization with Sc-d orbitals, Se-p states predominate in the valence region (-6 eV to -2 eV). Sc-d states dominate the conduction region, with Sc-p orbitals playing a minor contribution. Crucially, Sc-d states are the primary source of the finite density of states at the Fermi level, which accounts for ScSe's metallic conductivity. Previous studies have anticipated the same characteristics [34–38]. For MnSe, the higher bands indicate the Se-s states, while the two lowest bands are the p-d hybridized bands. The energy of the spin down bands increases below the fermi level. The spin-up bands above the fermi level, on the

other bands shift to lower energy due to the strong p-d interaction. Consequently, spin-down states are less inhabited while spin-up states are more occupied. The spin up Mn-p bands make the main contribution at the Fermi level.

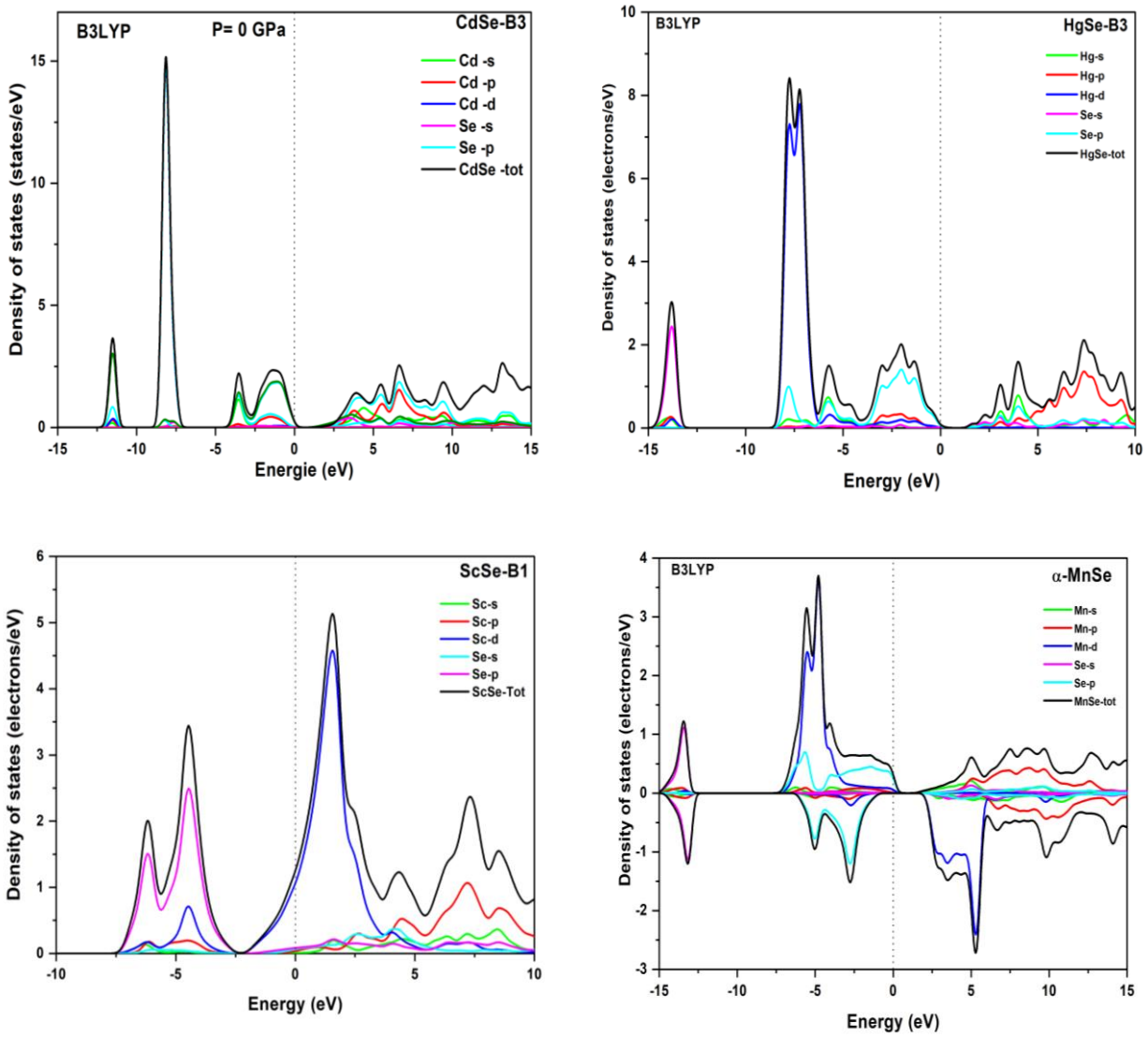

Figure III- 9: Total and partial density of states of CdSe, HgSe, ScSe and MnSe obtained by hybrid functional B3LYP.

III-3.4 Optical response

III-3.4.1 Dielectric function

The material's reaction to an applied electrical field, like an oscillating light wave, is described by the dielectric function [51]. When a material is exposed to an electric field, it becomes polarized due to the formation of electrical dipoles, which is represented by the quantity ε (ω). In this study, we used the Ehrenreich and Cohen equation [52] to calculate the complex dielectric function. The computed Re (ω) and Im (ω) components of the optical dielectric function for ScSe and MnSe in B1 structure, CdSe, and HgSe in the B3 structure are

displayed in Figure III-10. These figures demonstrate that the variation of ε (ω) reaches an acute peak for low values. Then, it is approached as a negative value in a region of medium energy. Continued by a low positive value in the region of high energies, however, the interband transition of electrons from the valence band to the conduction band is the cause of the major peak in each of the ε (ω) curves. A pronounced central peak is observed for all compounds, located at approximately 3.96 eV (CdSe), 1.70 eV (HgSe), 3.793 eV (ScSe) and 2.18 eV (MnSe). The Re (ω) of the dielectric function drops to zero at 7.98 eV, 6.97 eV, 7.503 eV and 6 eV for CdSe, HgSe, ScSe and MnSe, respectively. This behavior indicates that these materials primarily disperse the incident electromagnetic waves in this energy range. Such characteristics suggest that these materials could exhibit metallic-like responses and may be promising for radiation shielding applications. At higher energies, ε (ω) displays oscillations, turning negative before gradually approaching zero at 14.55 eV, 14.77 eV, 17.380 eV and 26.27 eV for CdSe, HgSe, ScSe and MnSe, respectively.

Absorption in a material is represented by the dielectric function's imaginary part (ε_{∞}). In transparent materials, $\varepsilon_{\infty}(\omega)$ is nearly zero, and absorption occurs once interband transitions are allowed. For CdSe and MnSe, $\varepsilon_{\infty}(\omega)$ remains zero at low energies before rising. Whereas HgSe and ScSe exhibit finite values even in this region. For CdSe and MnSe, the dielectric function's initial critical point is located at energies of 0.405 eV and 1.913 eV, respectively. These energies represent the threshold of optical transitions from the valence band's highest point to the conduction band's lowest point, this is known as the fundamental absorption threshold. Additionally, we observe a maximum primary peak, reflecting the highest absorption of these materials in the low-energy region. Consequently, the strong absorption in the infrared range and the upper limit of the visible spectrum make these materials promising candidates for optoelectronic device manufacturing.

The most desirable parameter is the static dielectric constant ε_0, which is the zero frequency limit of the actual part of the dielectric functions (ε_0), and is highly dependent on the energy of the band. The values of ε_0 and ε_∞ dielectric constants for CdSe, HgSe, ScSe and MnSe are shown in Table III-7. Our calculation of the ε_0 of CdSe is less than the experimental results reported in references [53,54]. However, the ε_∞ of CdSe closely matches the experimental results reported in references [55]. Moreover, the values of the Static dielectric constant ε_0 of HgSe, ScSe and MnSe have no comparable experimental results available; in addition, the value of the ε_∞ of HgSe closely matches the experimental results reported in references [56].corrections

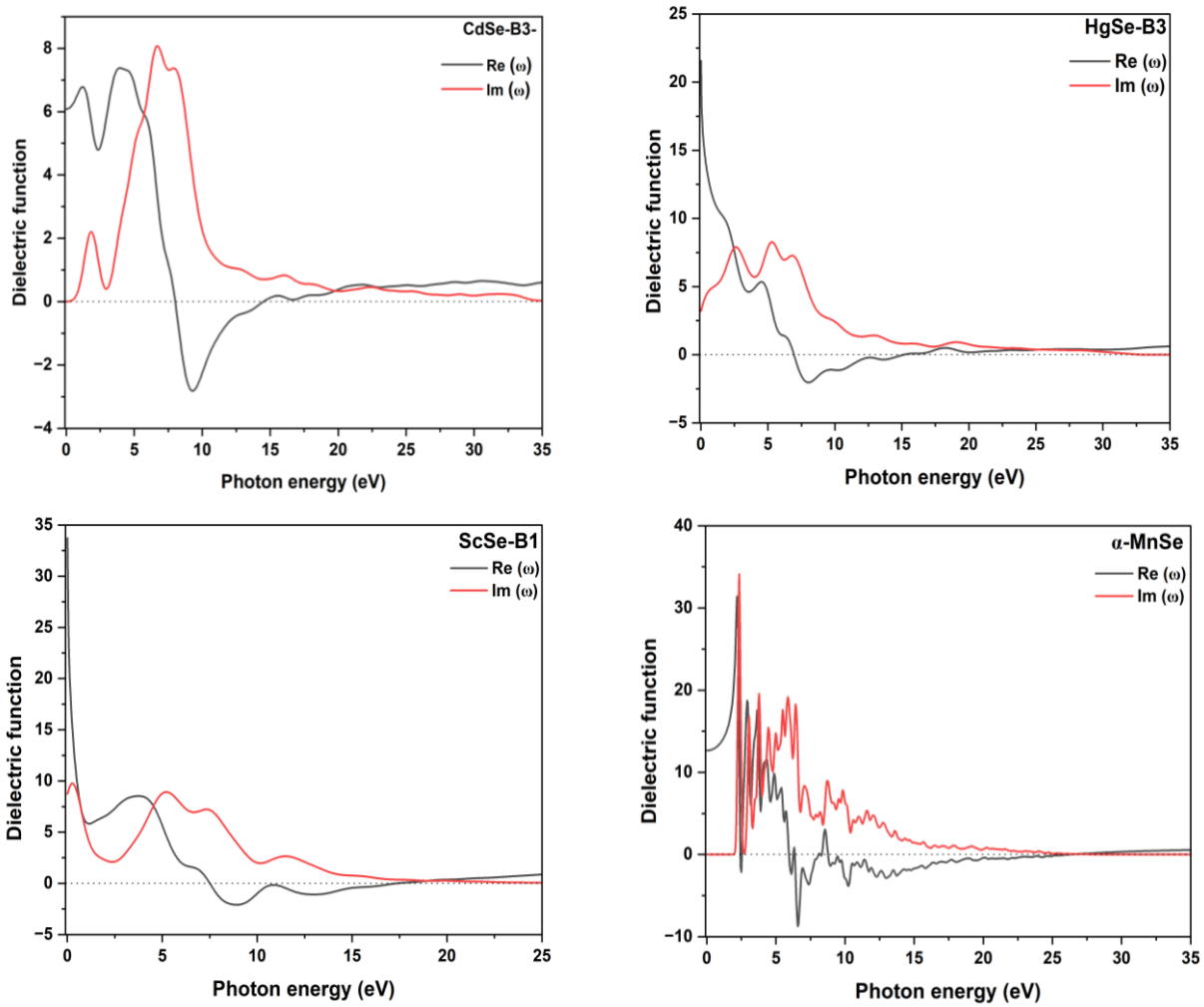

Figure III- 10: Real R $\boldsymbol{\varepsilon(\omega)}$ and imaginary Im $\boldsymbol{\varepsilon(\omega)}$ parts of the dielectric function as a function of photon energy of CdSe, HgSe, ScSe and MnSe.

Table III- 7: Static ($\boldsymbol{\varepsilon_0}$) and high frequency($\boldsymbol{\varepsilon_\infty}$) dielectric constant for CdSe and HgSe, ScSe and MnSe.

Compounds	parameters	This study	Other calculations	Experiments
CdSe	ε_0	6.080	6.75 [57] 9.23 [58]	9.4 [53] 9.53 [54]
	ε_∞	5.612	5.903 [59] 6.299 [18] 5.40 [60] 7.99 [58]	5.8 [55]
HgSe	ε_0	21.558	13.5 [61]	
	ε_∞	15.450	24.3 [32] 16.65 [62] 16.4 [63] 19 [63]	15.37 [56]
ScSe	ε_0	33.719	23.9 [9]	
	ε_∞	8.730		
MnSe	ε_0	12.660		
	ε_∞			

III-3.4.2 Refractive index

One important factor in the design and production of technological devices is the refractive index [64]. For B3 structure of CdSe and HgSe and B1 structure ScSe and MnSe, we calculated the refractive index spectra n (ω) and the extinction coefficient k (ω). The outcomes depicted in Figure III-11. For CdSe, the refractive index curve exhibits a primary incident energy range of 2.5-20 eV, while for HgSe, ScSe and MnSe, the dominant spectral feature appear in the range 0 eV to 15 eV. These peaks, which result from electrons moving from the valence band to the conduction band, occur near resonance frequencies. The refractive index n (ω) of an optical medium is a dimensionless quantity that characterizes the method in which light or any other radiation passes through the medium. The static refractive index is the value of n (ω) at the incident photon's zero-frequency limit.

Table III-8 represents the calculated values of n (ω) for CdSe, HgSe, ScSe and MnSe. Our result for the refractive index n(ω) of CdSe closely matches the experimental results reported in references [65] and shows better consistency to other theoretical works [57–59]. However, for HgSe, ScSe and MnSe have no comparable experimental results available. Our results are predictable and may serve as references that may guide future experimental investigations and technological applications.

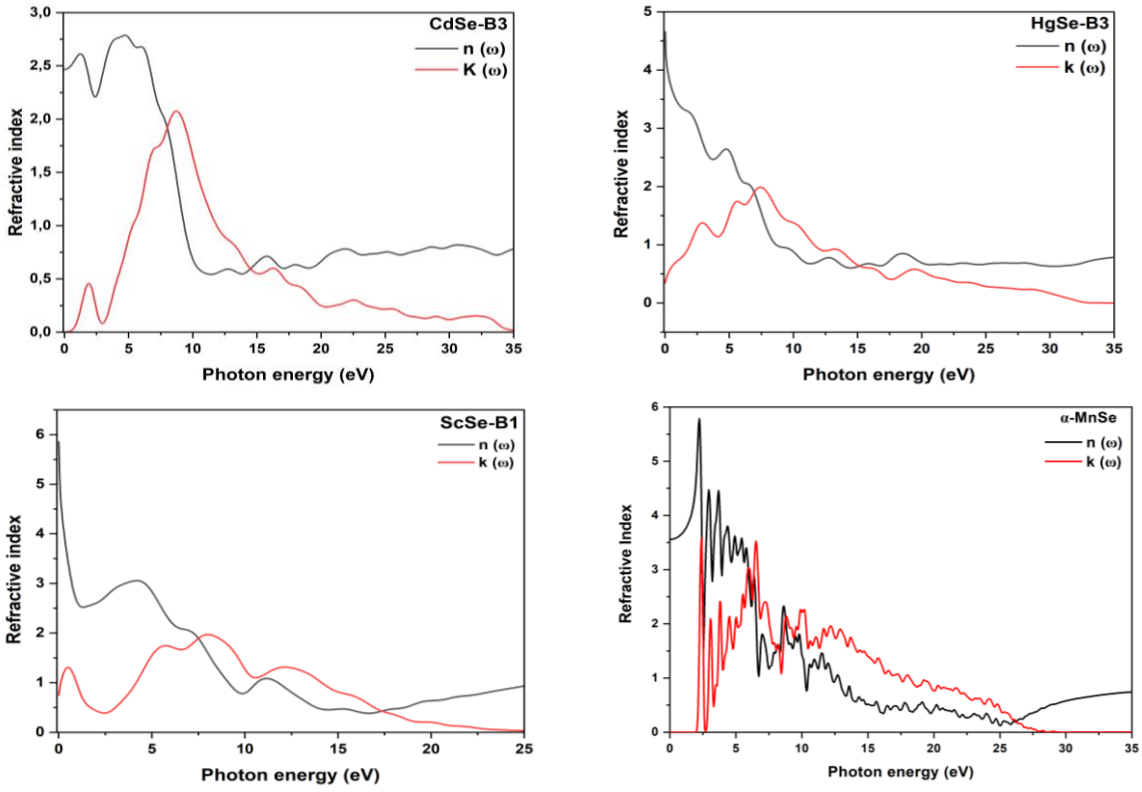

Figure III- 11: Real n(***ω***) and imaginary k(***ω***) parts of the refractive index for CdSe, HgSe, ScSe and MnSe as a function of photon energy.

Table III- 8: Static refractive index $n(0)$ for CdSe, HgSe, ScSe and MnSe.

Compound	This study	Other calculations	Experiments
CdSe	2.460	2.83 [58] 2.388 [59] 2.56 [57]	2.4-2.5 [65]
HgSe	4.650	3.654 [59]	
ScSe	5.850	4.89 [9]	
MnSe	3.550		

III-3.4.3 Reflectivity

Another crucial optical characteristic that may be obtained from the complex dielectric function ε (E) is the reflectivity spectrum. These parameters give important information about a material's electrical excitations and optical performance by describing the amount of incident electromagnetic radiation that is reflected from its surface. In this work, over the photon energy range of 0-35 eV, we computed the reflectivity spectra of CdSe, HgSe, ScSe, and MnSe. The reflectivity spectrum is displayed as a function of photon energy, taking into account light polarized along the key crystallographic directions, as shown in Figure III-12. Table III-9 represents the values of the reflectivity spectrum for CdSe, HgSe, ScSe and MnSe. Currently, no experimental reflectivity data are available for CdSe, HgSe, ScSe or MnSe for direct comparison. However, our results align with earlier theoretical estimates published in the literature [59], particularly for CdSe and MnSe.

Overall, the calculated reflectivity spectra reveal pronounced peaks in the low to mid energy range, which correspond to interband electronic transitions observed in the dielectric function and refractive index spectra. These results provide reliable reference data for future experimental validation and highlight the potential of these materials in optoelectronic and photonic applications, especially in energy ranges where high reflectivity is desirable (e.g., radiation shielding or optical coatings).

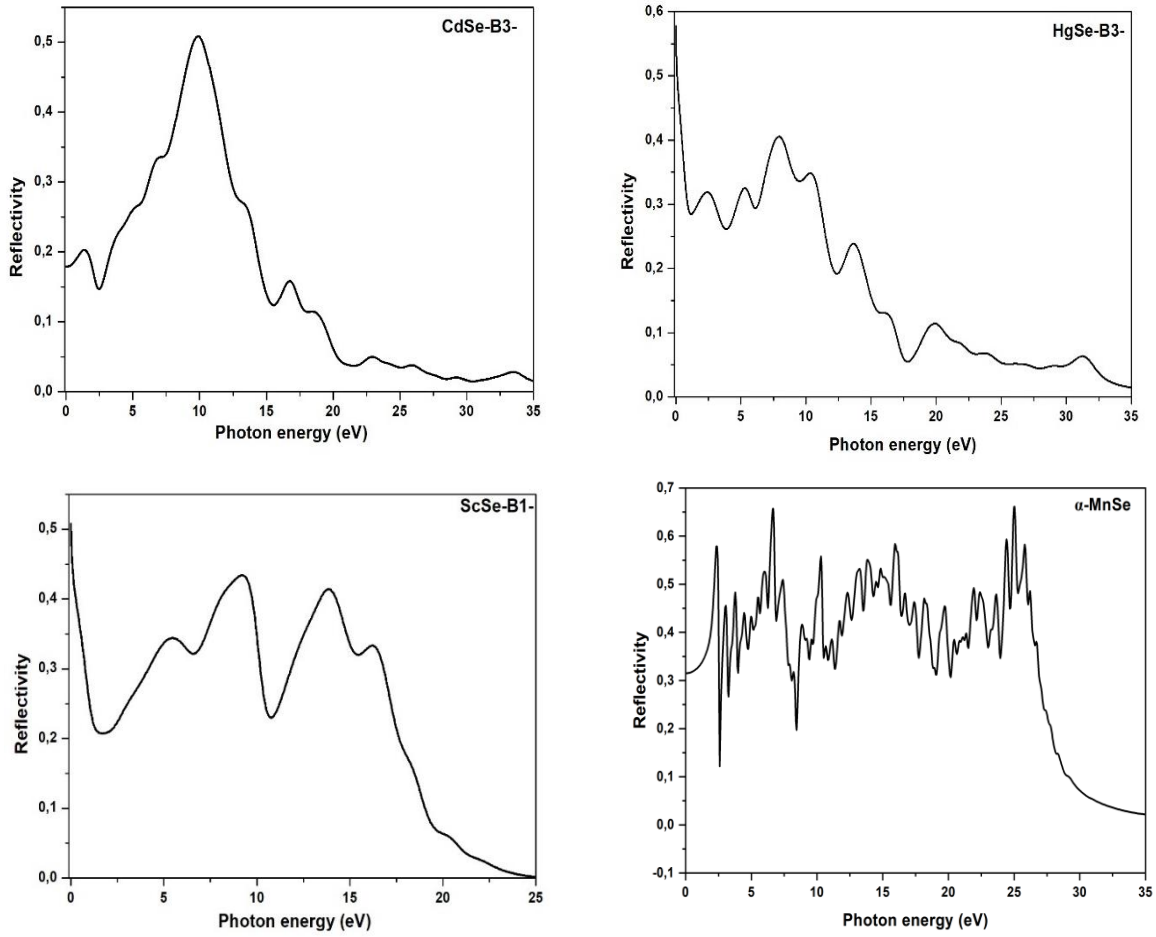

Figure III- 12: Reflectivity spectrum of CdSe, HgSe, ScSe and MnSe as a function of photon energy.

Table III- 9: Static reflectivity $R(0)$ for CdSe, HgSe, ScSe and MnSe.

Compounds	This study	Other calculations	Experiments
CdSe	0.178	0.177 [59] 0.209 [59] 0.195 [57]	
HgSe	0.419	0.316 [59] 0.272 [59]	
ScSe	0,507		
MnSe	0.310		

III-3.4.4 Absorption coefficient

The fundamental parameter known as the optical absorption coefficient determines the that distance that a particular wavelength of light may go through a substance before being absorbed. It provide critical insights into the interaction of photons with electronic states and is especially relevant for the design of optoelectronic and photonic devices.

The present study determined the optical absorption coefficient as a function of photon energy for CdSe and HgSe in the B3 structure, ScSe, and MnSe in the B1 structure. The results are shown in Figure III-13. Our calculation reveal that the onset of optical absorption occurs at approximately 0.81 eV and 1.87 eV for both CdSe and MnSe, corrresponding to their transitions. In contrast, absorption in HgSe and ScSe begin at 0 eV, consistent with their metallic or semi metallic character. The absorption coefficient increases steadly with increase photon energy, reaching about 9.08 eV, 7.75 eV, 12.77 eV, and 12.93 eV for CdSe, HgSe, ScSe, and MnSe, respectively. Beyond these maxima, the absorption coefficient gradually decreases and is eliminated at photon energies above 30 eV for all compounds.

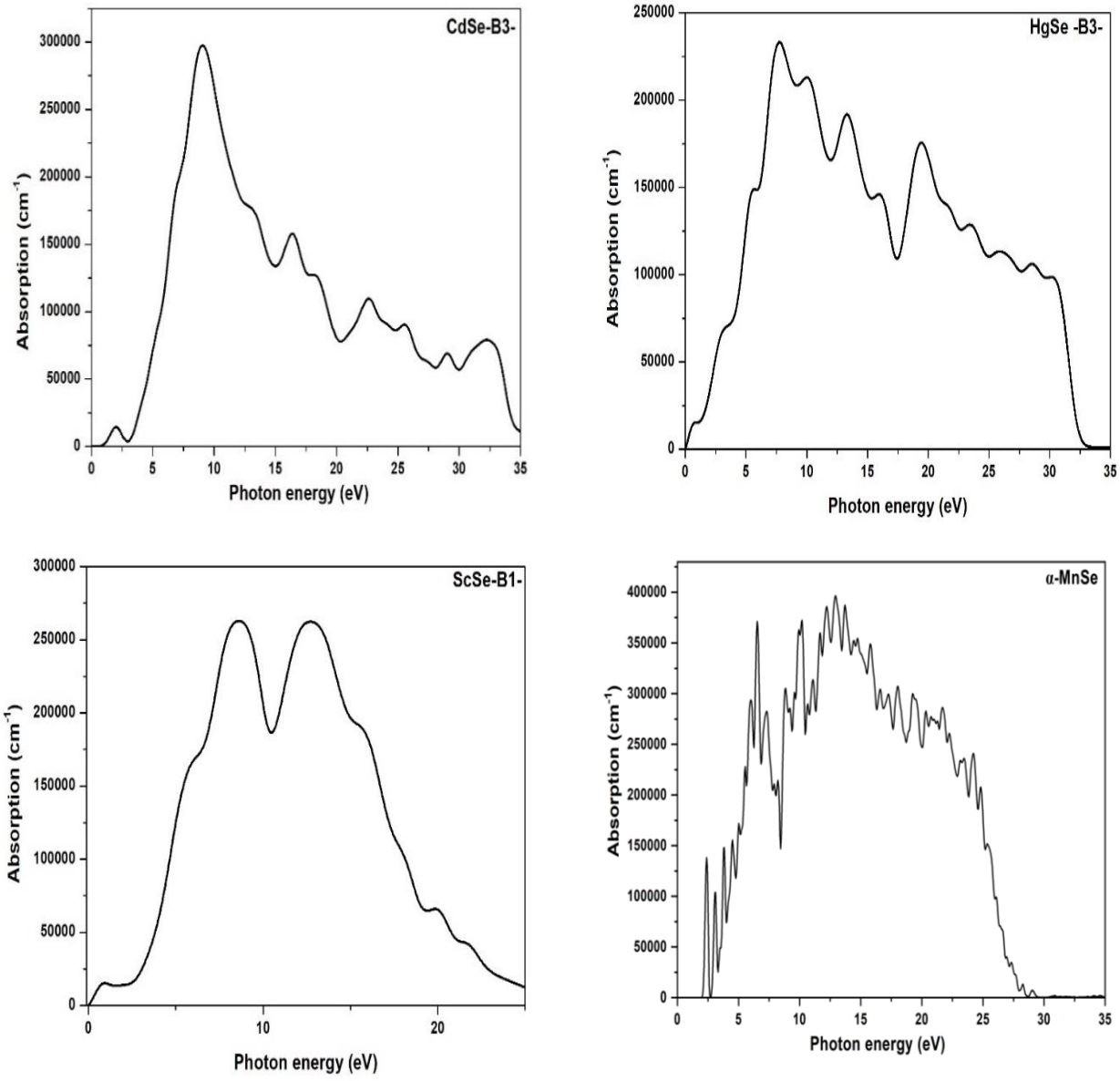

Figure III- 13: Optical absorption spectrum of CdSe, HgSe, ScSe and MnSe as a function of photon energy.

III-3.5 Elastic parameters and related mechanical properties

The elastic theory studies how materials can return to their original shapes and sizes after deformation forces are removed. Near the equilibrium position of atoms, we can consider the solid's energy as a quadratic function of its parameters. When a crystal is stressed, it deforms, changing the parameters that define it. These are the homogeneous deformations of the crystal. Near equilibrium, the quadratic energy expansion enables us to describe a linear relationship between stress and deformation, known as Hooke's law [66]. Elastic constants describe this relationship and determine the solid's mechanical stability against deformations. For the equilibrium point to be stable, the quadratic form of energy must be positive, which sets conditions on the elastic constants [67]. There are just three known elastic constants in cubic crystals: C_{11}, C_{12}, and C_{44}.

Poisson's ratio (v) and Young's modulus (E) are significant in some engineering and technical applications. As a ratio of stress to strain, Young's modulus was defined and is used to measure the stiffness of a solid. Poisson's ratio provides additional information about the characteristics of bonding forces, which are also calculated using the data in relation to the following formula [68] :

$$\nu = \frac{1}{2}\left[\frac{B-(2/3)G}{B+1/3G}\right] \qquad \text{III} - 4$$

$$E = \frac{9GB}{G+3B} \qquad \text{III} - 5$$

When G is the isotropic shear modulus in the form:

$$G = \frac{G_V+G_R}{2} \qquad \text{III} - 6$$

The upper bound of the G value is represented by G_V, or Voigt's shear modulus, and the lower bound by G_R or Reus's shear modulus, which can be written as follows [69] :

$$G_v = \frac{C_{11}+C_{12}+3C_{44}}{5} \qquad \text{III} - 7$$

$$\frac{5}{G_R} = \frac{4}{C_{11}-C_{12}} + \frac{3}{C_{44}} \qquad \text{III} - 8$$

The Pugh ratio (K) [71] and the Cauchy pressure (C″) [70] are frequently used in practice to assess a material's brittleness or ductility. They are calculated as follows:

$$C'' = C_{12} - C_{44} \qquad III - 9$$

$$K = \frac{B}{G} \qquad III - 10$$

Pettifor proposed that variations in C″ relate to the nature of the atomic bond. If the bond is metallic (C″ > 0) and the materials are ductile, while for brittle materials, the bond is directional (C″ < 0). The Pugh ratio (B/G) was initially introduced to distinguish between ductile and brittle behavior of a material. A low (B/G) value indicates brittleness, whereas a high value indicates ductility. The transition from brittle to ductile occurs at a critical value of K~1.75. Brittle materials typically have a Poisson's ratio below the critical value (ν < 0.26).

Tables III-10, III-11, III-12, and III-13 show the calculated elastic constants, shear modulus (G), Young's modulus (E), Poisson's ratio (v), Cauchy pressure (C″), and Pugh ratio (K) for CdSe and HgSe in the zinc-blende structure and ScSe and MnSe in the rock-salt structure.

The calculated C_{11}, C_{12}, and C_{44} for CdSe show no available experimental data for direct comparison. However, our results align well with previously reported theoretical studies [18,72,73]. Moreover, for HgSe the obtained results of C_{11}, C_{12}, and C_{44} closely match the experimental data [74,75], with the exception of C_{44}, which shows a slight deviation. Additionally, our findings closely match those of other ab initio computations reported in the literature [22,31,59]. In case of ScSe, experimental data for comparison are unavailable; however, our computed values agree with those found in the literature [7,9,35,38]. Similarly, for MnSe, no experimental elastic constant results are available for validation. However, our results are reliable, theoretically consistent and may serve data for future investigations.

There are no known experimental data to compare the Young's modulus (E) of CdSe, HgSe, ScSe, and MnSe. The calculated results of Young's modulus (E) closely match those reported in reference [18] for CdSe, reference [22,31] for HgSe, reference [9,38,76] for ScSe and reference [27] for MnSe. Similarly, experimental data for the shear modulus (G) of CdSe, ScSe, and MnSe are unavailable. However, our calculated shear modulus (G) for the zinc-blende structure of HgSe exceeds the experimental results [74], but aligns well with the theoretical values reported in [31]. Furthermore, our results can serve as reliable references.

Having obtained the requisite data, we can proceed to discuss the compounds' brittle or ductile properties. The ductility and brittleness of materials can be elucidated using a certain relationship. According to Frantsevich's rule [77], the critical value of Poisson's ratio (v) is 0.26, below which a material is considered brittle and beyond which it is considered ductile.

The calculated Poisson's ratio for all compounds is found to be above the critical threshold of 0.26. Indicating a ductile character. These values show excellent accord with previously reported theoretical results for CdSe [18] , [22,31] HgSe and [9,38,76] ScSe, No experimental data is available for comparison. The plastic characteristics of materials are empirically linked to their elastic modulus by the ratio B/G, according to a simple relationship suggested by Pugh [71]. A low B/G value indicates brittleness, whereas a high value signified ductility. The value of Pugh's criterion B/G is 3.370 for CdSe, 2.530 for HgSe, 2.003 for ScSe and 2.262 for MnSe. Since this value is greater than the critical value, it is evident that all compounds are ductile. This result is the same as that reported in the reference [38] for ScSe. The Cauchy pressure (C″) is another indication of the materials' brittle-ductile properties. The difference between the elastic constants C_{12}– C_{44} is the Cauchy pressure [70] for cubic crystals. However, Pettifor proposed that variation in Cauchy pressure relate to the nature of atomic bond. If the bond is metallic (C″ > 0) and the materials are ductile, while for brittle materials, the bond is directional (C″ < 0). The calculated Cauchy pressures 24.373 for CdSe, 19.927 for HgSe and 10.254 for MnSe indicate non directional bonding and ductility. These results are consistent with the Pugh's ratio and Poisson's ratio. Conversely, the slightly negative Cauchy pressure (-3.203) as obtained for ScSe typically reflects directional covalent bonding, which may induce local brittle tendencies along specific crystallographic planes, even though the material is globally ductile [78].

Understanding these elastic constants helps us verify mechanical stability of these studied compounds. A crystal must meet the Born stability criterion in terms of its elastic C_{ij} in order to be considered mechanically stable [79,80]. In addition to being positive. For cubic system the criteria are expressed as:

$$C_{11} - C_{12} > 0 \qquad C_{44} > 0 \qquad C_{11} + 2C_{12} > 0 \qquad \text{III} - 11$$

By substituting these calculated elastic constants into these relations, we confirm that all three conditions are satisfied. This demonstrates that B3 structure of CdSe and HgSe as well as B1 strcture of ScSe and MnSe are mechanically stable at equilibrium.

Table III- 10: The calculated elastic constants (C_{ij}), shear modulus (G), Young's modulus (E), Poisson's ratio (ν), Cauchy pressure and Pugh ratio of CdSe.

Compound	Parameters	This study	Other calculations	Experiments
CdSe	C_{11}(GPa)	60.488	58.8 [18] 55.4 [72] 65 [73]	
	C_{12}(GPa)	44.510	48.9 [18] 37.7 [72] 49 [73]	
	C_{44}(GPa)	20.137	25.2 [18] 18.9 [72]	
	G (GPa)	14.184	13.3 [18]	
	E	38.847	36.8 [18]	
	ν	0.369	0.383 [18]	
	C_{12}-C_{44}	24.373		
	B/G	3.470		

Table III- 11: The calculated elastic constants (C_{ij}), shear modulus (G), Young's modulus (E), Poisson's ratio (ν), Cauchy pressure and Pugh ratio of HgSe.

Compound	Parameters	This study	Other calculations	Experiments
HgSe	C_{11}(GPa)	69.932	74.05 [31] 69.14 [81] 52.69 [22]	69 [74] 62.16 [75]
	C_{12}(GPa)	51.321	50.7 [31] 44.27 [81] 37.99 [22]	51.05 [74] 46.41 [75]
	C_{44}(GPa)	31.394	44.1 [31] 23.92 [81] 33.69 [22]	23.07 [74] 22.68 [75]
	G (GPa)	22.558	18.56 [22] 23.10 [31]	16.50 [75]
	E	59.851	48.52 [22] 61.80 [31]	
	ν	0.327	0.311 [22] 0.337 [31]	
	C_{12}-C_{44}	19.927		
	B/G	2.530		

Table III- 12: The calculated elastic constants (C_{ij}), shear modulus (G), Young's modulus (E), Poisson's ratio (ν), Cauchy pressure and Pugh ratio of ScSe.

Compound	Parameters	This study	Other calculation	Experiments
ScSe	C_{11} (GPa)	227.390	239.76 [7] 238 [35] 200.442 [76] 228.28 [9] 193.23554 [38]	
	C_{12} (GPa)	19.924	23.99 [7] 25 [9] 21.55 [35] 25.059 [38] 26.649 [76]	
	C_{44} (GPa)	23.127	104.5 [7] 23.51 [9] 98.85 [35] 22.052 [38] 25.35 [76]	
	G (GPa)	44.463	116.65 [7] 44.35 [9] 42.670 [76] 39.0754 [38]	
	E	114.362	149 [7] 82.76 [9]	
	ν	0.286	0.07 [7] 0.71 [9] 0.286 [9] 0.284 [76] 0.28634 [38]	
	C_{12}-C_{44}	-3.203	-80.5 [7]	
	B/G	2.003	0.82 [7] 2.0759 [38]	

Table III- 13: The calculated elastic constants (C_{ij}), shear modulus (G), Young's modulus (E), Poisson's ratio (ν), Cauchy pressure and Pugh ratio of MnSe.

Compound	Parameters	This study	Other calculation	Experiments
MnSe	C_{11}(GPa)	113.454	191.1 [27]	
	C_{12}(GPa)	42.779	37.3 [27]	
	C_{44}(GPa)	32.525	15.4 [27]	
	G (GPa)	33.622	31.31 [27]	
	E	86.289	84.06 [27]	
	ν	0.283		
	C_{12}-C_{44}	10.254		
	B/G	2.262		

III-3.6 Lattice dynamics

The creation of novel materials requires an understanding of the dynamic behavior of solids, especially when evaluating their thermodynamic qualities. Phonons play a key role in this process. Figure III-14 shows the phonon dispersion scheme computed using the optimized lattice parameters along several high-symmetry directions in the Brillouin zone (BZ) for CdSe and HgSe in B3 structure and ScSe in B1 structure.

In cubic crystals containing two atoms per primitive cell. The phonon spectrum give rise to the three acoustic branches and three optical branches. Importantly, for CdSe and HgSe in the zinc-blende (B3) structure, as well as ScSe in the rock-salt (B1) structure, the dispersion curve show no negative frequencies throughout the Brillouin zone. This confirm that these compounds (CdSe), HgSe and ScSe) are dynamically stable in their respective crystal structures. Table III-14 presents our calculation of phonon frequencies at the high-symmetry point (Γ) for CdSe, HgSe and ScSe.

For CdSe, the values of 199.201 cm^{-1} and 165.497 cm^{-1} were obtained for longitudinal (ω_{LO}) and transverse optical (ω_{TO}) modes, respectively; although experimental data for comparison are unavailable, these result are in good accordance with previous ab initio calculations reported in the literature [18]. Furthermore, for of HgSe, we obtained ω_{LO}=164.176 cm^{-1} and ω_{TO}=132.518 cm^{-1}, which also show good consistency with earlier theoretical studies [32]. For ScSe, the calculated phonon frequencies are ω_{LO}=218.176 cm^{-1} and ω_{TO}=213.320 cm^{-1}.

Notably, polar semiconductors such as CdSe and HgSe show a clear LO–TO splitting close to the Γ point. The longitudinal optical (LO) and transverse optical (TO) modes are distinguished by the long-range Coulomb interactions between the macroscopic electric field and the lattice vibrations. The degree of this splitting directly influences the material's dielectric response and reveals the ionic nature of the bonding.

Conversely, for MnSe, we were unable to determine the dynamic phonon dispersion and related dynamic properties using the CASTEP code, which limits our analysis of its vibrational behavior.

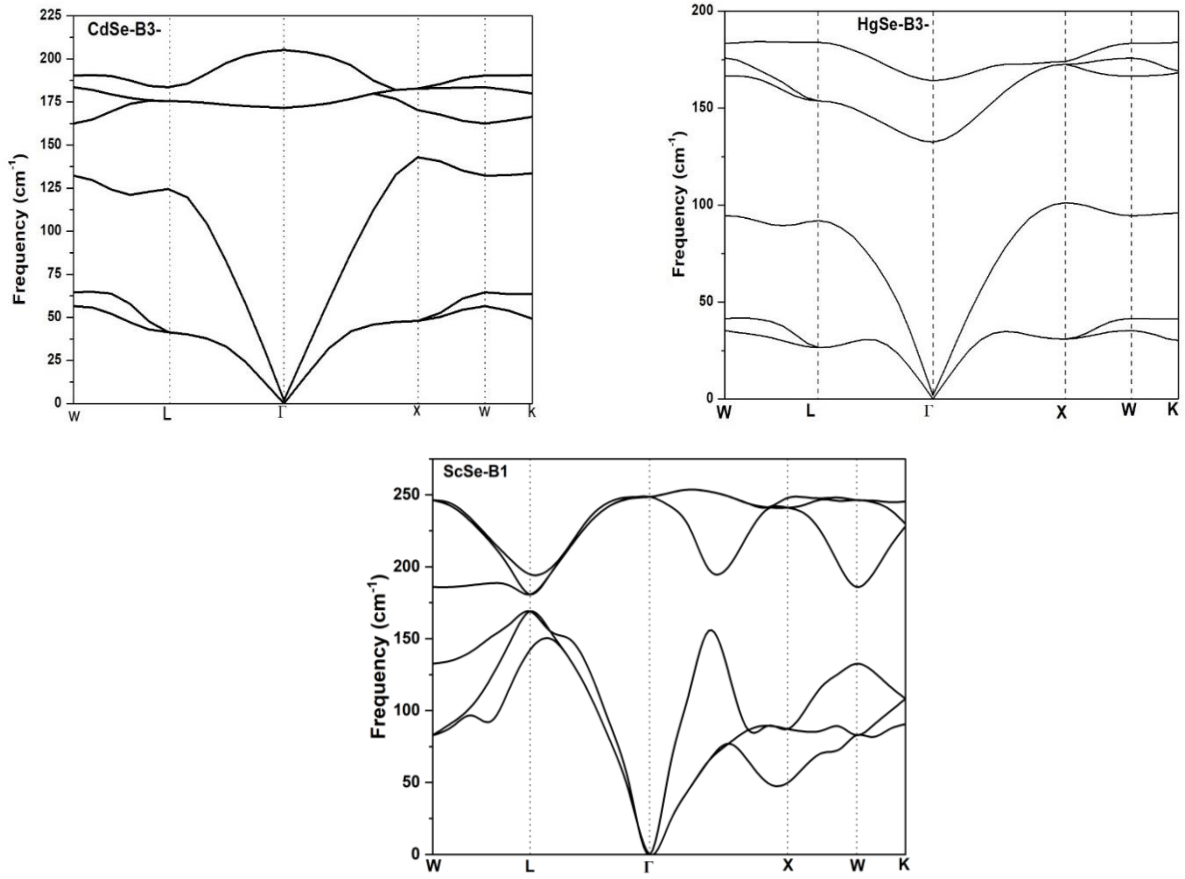

Figure III- 14: phonon dispersion curves of CdSe, HgSe and ScSe.

Table III- 14: Phonon frequencies at high-symmetry point for CdSe, HgSe and ScSe.

Compounds	Phonon frequencies (cm^{-1})	This study	Other calculations	Experiments
CdSe	ω_{Lo}	199.201	224 [18] 216 [18]	
	ω_{TO}	165.497	192 [18] 186 [18]	
HgSe	ω_{Lo}	164.176	160.66 [32]	
	ω_{TO}	132.518	132.23 [32]	
ScSe	ω_{Lo}	218.176	233 [38]	
	ω_{TO}	213.320	237 [38]	

III-3.7 Thermodynamic properties

The thermodynamic properties of a crystalline material are closely linked to the vibrations of the lattice, which are governed by phonons. These vibrational modes play a central role in determining the heat capacity, entropy, free energy, and related thermal behaviors of solid. A fundamental framework for studying is the equation of state (EOS). The EOS, a crystalline phase, describe its response to variation in macroscopic parameters such as pressure

and temperature. Experimentally, EOS parameters are obtained by fitting measured pressure-volume (P-V) data to empirical relations, such as the Birch-Murnaghan or Murnaghan equations of state. From a theoretical perspective, however, these quantities can be derived directly from first-principles calculations, which provide a microscopic description of the system's energetics under different thermodynamic conditions.

When a system is subjected to a particular temperature (T) and hydrostatic pressure (P), its equilibrium properties, such as equilibrium volume, bulk modulus, and thermal expansion, can be correctly derived from the EOS. Therefore, the EOS serves as a key link between microscopic lattice dynamics and macroscopic thermodynamic behavior, enabling predictive insights into the stability and performance of materials under diverse conditions.

The thermodynamic properties of CdSe and HgSe, along with ScSe and MnSe, have been examined using the quasi-harmonic Debye model implemented in the Gibbs code [15]. The calculation of thermodynamic properties with Gibbs begins with a set of values for the total energy of the system as a function of unit cell volume, E(V), obtained through an ab initio calculation. We studied the effects of temperature on the bulk modulus (B), the coefficient of thermal expansion (α), and specific heat (C_v).

III-3.7.1 Bulk modulus (B)

The bulk modulus (B) is a fundamental mechanical property that reflects a material's resistance to uniform compression. In general, B decreases with increasing temperature. Figure III-15 illustrates the temperature dependence of the bulk modulus (B) for CdSe, HgSe, ScSe and MnSe. As observed, B decreases gradually with increasing temperature, making the crystal more compressible at higher temperatures. Typically, an increase in temperature causes the material to expand, thereby increasing interatomic distances. This expansion weakens interatomic bonding forces and reduces the material's stiffness. Consequently, the bulk modulus (B) decreases as temperature rises. Table III-15 gives the calculated of B of CdSe, HgSe, ScSe, and MnSe at 300 K. B is calculated to be 49.623 GPa (CdSe), 57.700 GPa (HgSe), 89.134 GPa (ScSe) and 77.057 GPa (MnSe) at ambient temperature. Thes values decrease slightly to 45.275 GPa, 51.239 GPa, 85.092 GPa and 70.369 GPa at 300 K for CdSe, HgSe, ScSe and MnSe, at 300 K, respectively.

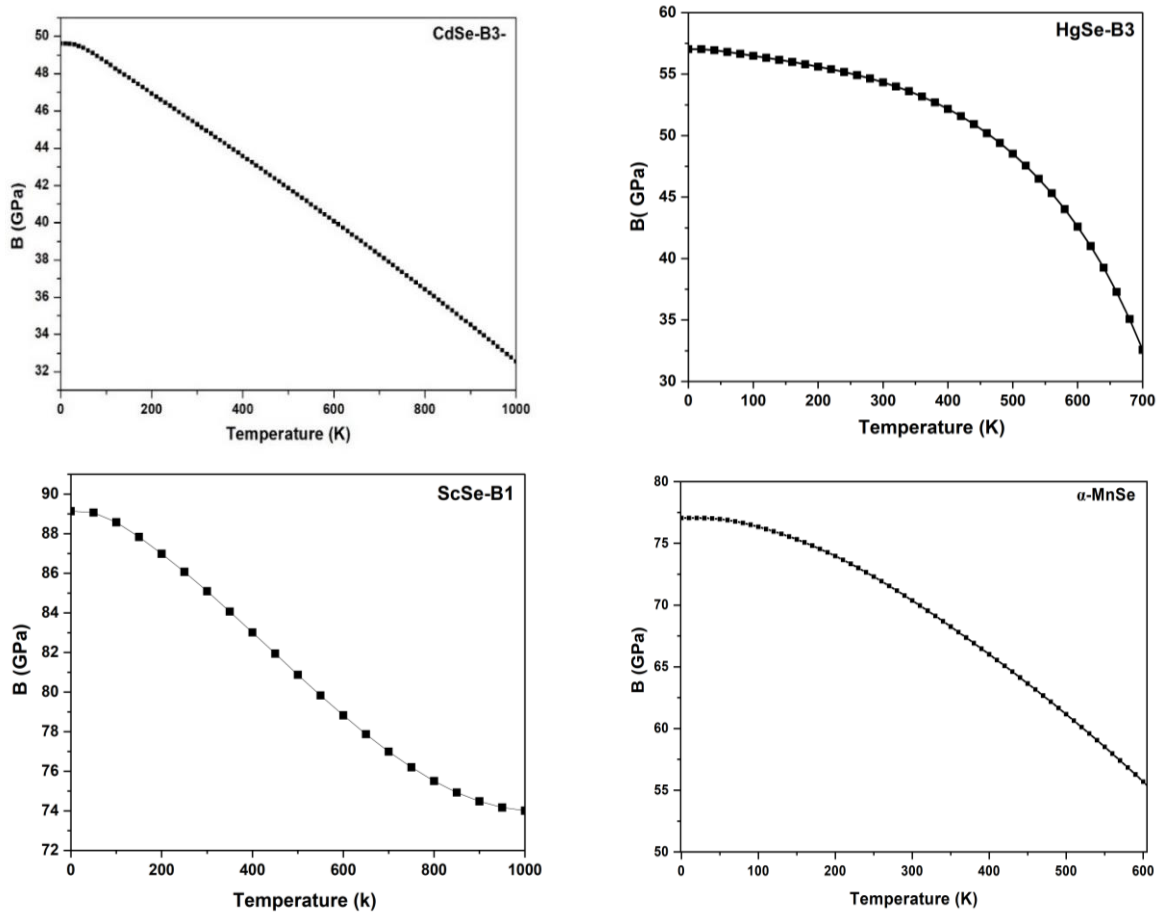

Figure III- 15: Variation of the bulk modulus (B) of CdSe, HgSe, ScSe and MnSe as a function of temperature.

Table III- 15: Bulk modulus (B) values of CdSe, HgSe, ScSe, and MnSe at 300 K.

Compounds	CdSe	HgSe	ScSe	MnSe
B (GPa)	45.270	55.933	85.090	70.369

III-3.7.2 Coefficient of thermal expansion

The thermal expansion coefficient (α) is critical parameter for understanding the thermodynamic and thermoelastic behavior of solid at high temperatures. Thermal expansion in solids leads to changes in the displacement of atoms from their equilibrium positions at high temperatures. These displacements are strongly influenced by factors such as anharmonic effects in the interatomic potential. Generally, thermal expansion is proportional to the temperature change, and materials with greater bonding energy exhibit lower expansion coefficient. Figure III-16 shows the variation of α as a function of temperature of CdSe, HgSe, ScSe, and MnSe. In all case, α show a monotonic increasing trend with rising temperature, reaching higher values at elevated temperatures. This observation suggests that the four

compounds maintain structural stability across the considered temperature range. Additionally, the overall trend of α curves for the ScSe closely resembles those reported in references [7,9]. Table III-16 lists calculated values of α of CdSe, HgSe, ScSe and MnSe at 300 K, α is calculated to be 6.601× 10^{-5} K^{-1}, 5.886× 10^{-5} K^{-1}, 4.623 × 10^{-5} K^{-1}, and 3.373× 10^{-5} K^{-1}, for CdSe, HgSe, ScSe and MnSe, respectively. which is slightly higher than that reported in reference [7] for ScSe.

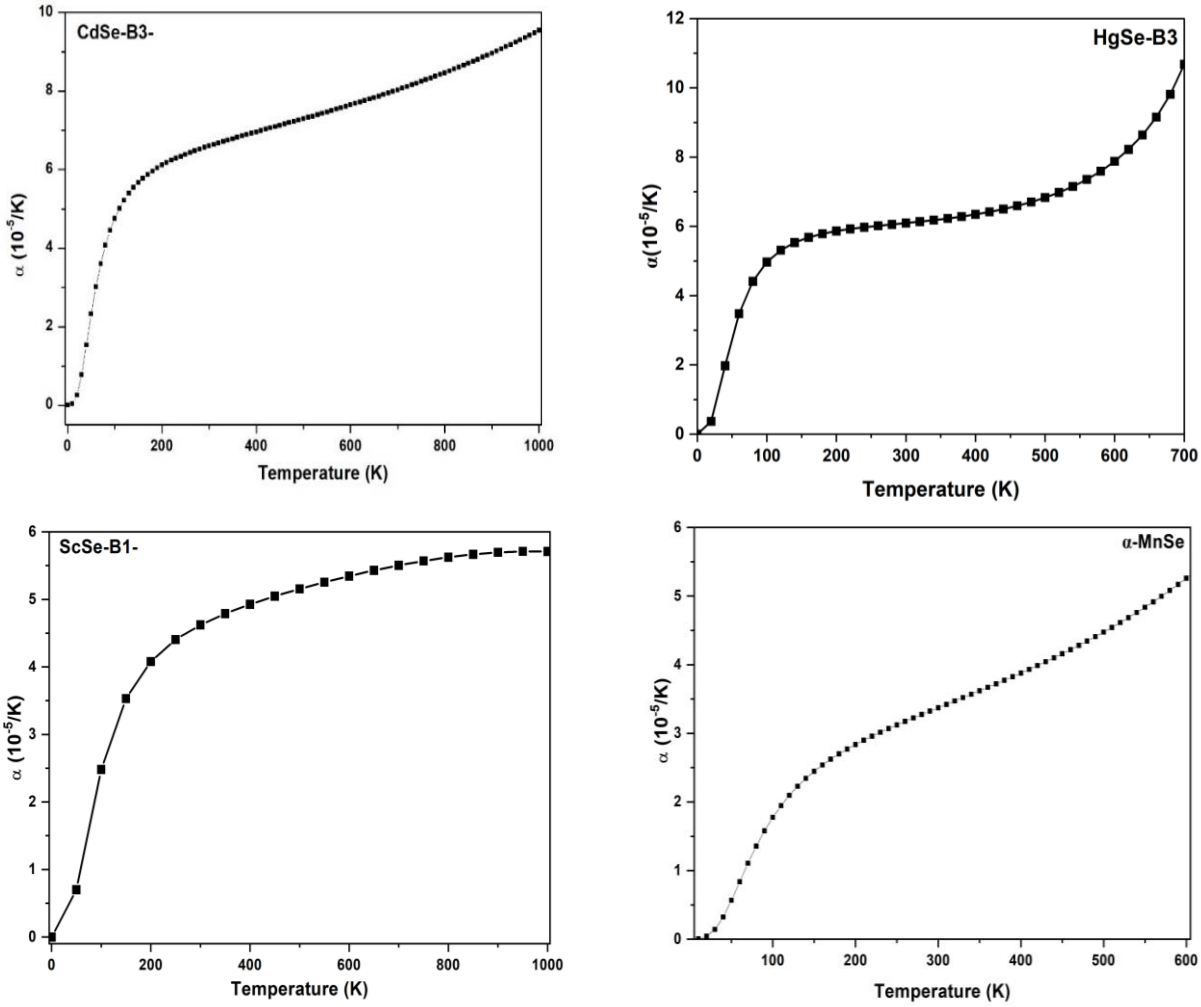

Figure III- 16: Variation of the thermal expansion coefficient (α) of CdSe, HgSe, ScSe and MnSe as a function of temperature.

Table III- 16: Thermal expansion (α) values of CdSe, HgSe, ScSe and MnSe at 300 K.

Compounds	CdSe	HgSe	ScSe	MnSe
α (10^{-5}/K)	6.601	5.886	4.623	3.373

III-3.7.3 Specific heat capacity C_V

The heat capacity is essential thermodynamic parameter that provides insights into material's vibrational characteristics and is of central importance in numerous applications. In particular, the specific heat at constant volume (C_V) reflects the phonon density of states, thereby offering direct connection to lattice dynamics. Figures III-17 illustrate the variation of C_V as a function of temperature for CdSe, HgSe, ScSe and MnSe. C_V exhibits similar behavior in response to temperature changes for CdSe, HgSe, ScSe, and MnSe. The heat capacity C_V of the studied systems exhibits two distinct behaviors, depending on T, across the considered range. At low temperatures, C_V rises rapidly with T, validating the experimental law in T^3 for these conditions. Conversely, at high temperatures, it gradually increases and approaches the Dulong-Petit limit: $C_V = 3nR$, where R is the gas constant and n is the number of atoms per unit cell. The calculated high temperature values converge to 49.774, 49.725, 49.576, and 49.629 (in units of $J.mol^{-1}K^{-1}$) for CdSe, HgSe, ScSe, and MnSe, respectively. Table III-17 presents C_V at 300 K for CdSe, HgSe, ScSe, and MnSe.

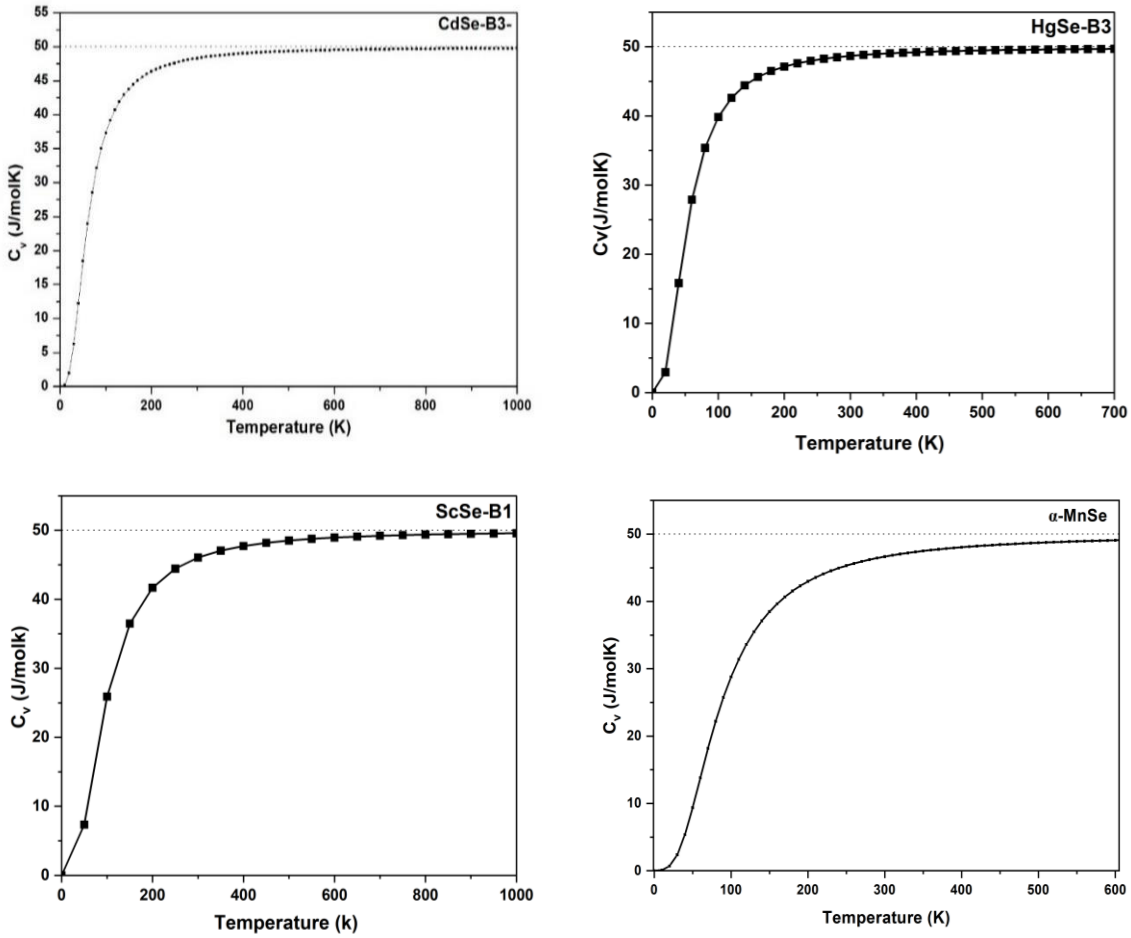

Figure III- 17: Variation of the heat capacity at constant volume C_V of CdSe, HgSe, ScSe and MnSe as a function of temperature.

Table III- 17: The heat capacity at constant volume (C_V) values of CdSe, HgSe, ScSe and MnSe at 300 K.

Compounds	CdSe	HgSe	ScSe	MnSe
C_v (J/mol.K)	48.302	48.673	46.043	46.656

III-4. Influence of pressure on properties

III-4.1 Influence of pressure phase transition

The change in total energy as a function of volume for CdSe and MnSe in both zinc-blende (B3) and rock-salt (B1) structures, HgSe in both zinc-blende (B3) and cinnabar (B9) phases, and ScSe in both NaCl (B1) and CsCl (B2) structures is shown in Figure III-18.

Applying hydrostatic pressure to a crystalline material causes its volume to decrease. When the pressure reaches a certain critical value, called the transition pressure (P_t), the material undergoes a structural phase change from its most stable form under ambient conditions to a more compact and energetically favorable phase. This study used the tangent method to determine the transition pressure (P_t). This method determines the transition point by analyzing the intersection of the energy-volume curves of the two competing phases. The common tangent line connecting the tangential points on the two total energy curves indicates the pressure induced transition. To find the transition pressure (P_t) from the E (V) curves, we calculated the pressure using the following relationship:

$$P_t = \left|\frac{E_2 - E_1}{V_2 - V_1}\right| \qquad \text{III} - 12$$

Table III-18 presents the calculation of the transition pressure (P_t) for CdSe, HgSe, ScSe, and MnSe. The calculation of transition pressure (P_t) of CdSe 2.622 GPa for the B3→B1 is a agree well with the experimental value reported in references [83], and shows better consistency compared to previous simulations [84]. In contrast, the calculation of transition pressure (P_t) of HgSe 2.745 GPa for the B3→B9 is greater than the experimental value reported in the range 0.74 to 2.20 [2,85–87]. and also exceeds the values predicted by other ab initio calculations, which range from 0.78-1.96 GPa [22,88,89]. However, our calculations of the transition pressure of ScSe 40.838 GPa for the B1→B2 have no comparable experimental results available. Yet, it is slightly smaller than the theoretical values published in the range of 47.0-53.65 GPa [7,35]. Similarly, the calculated transition pressure of MnSe 0.652 GPa for the MnSe B1→B3 transition also lacks experimental validation but is less than the theoretical value mentioned in reference [45].

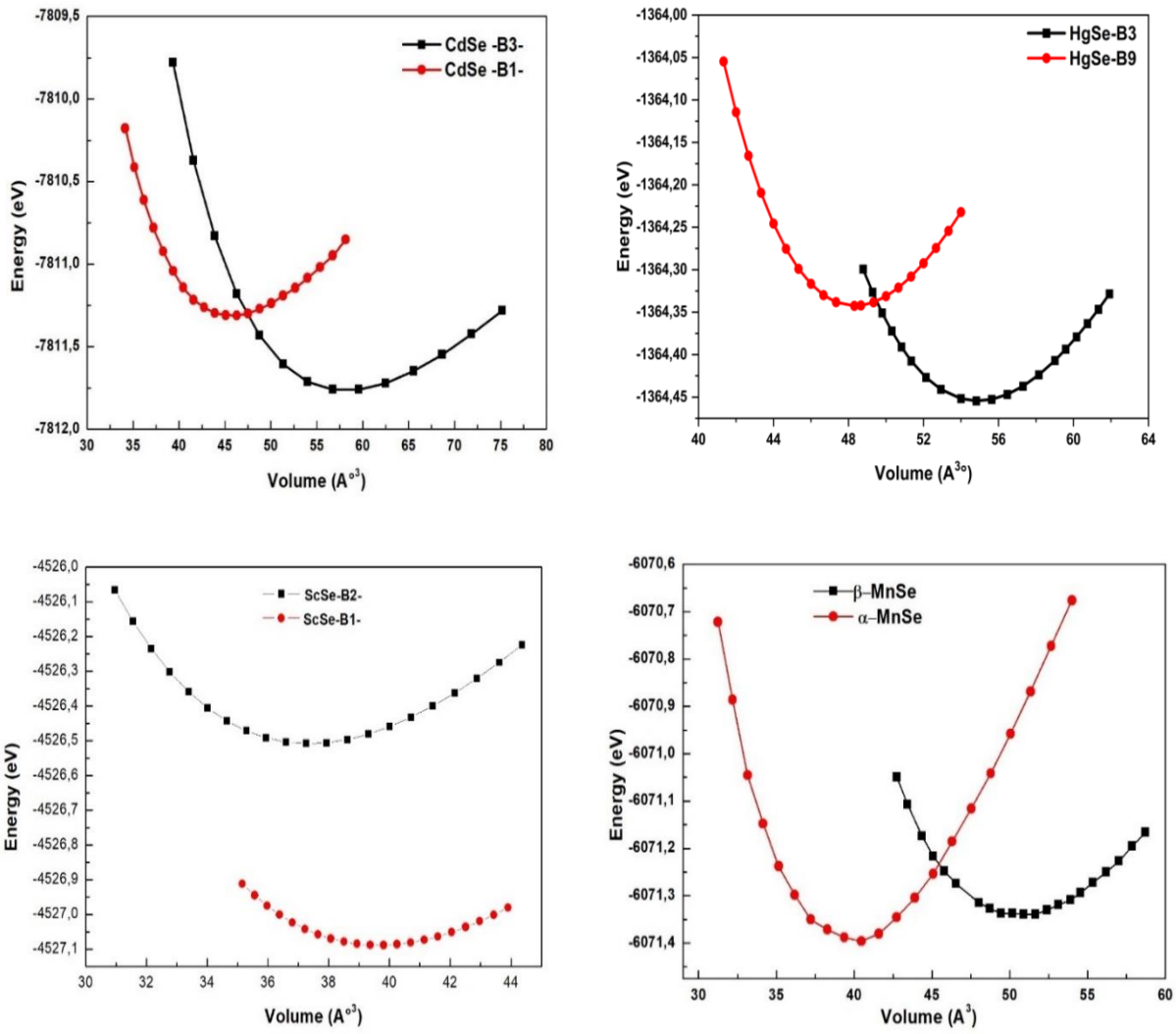

Figure III- 18: Variation of total energy as a function of volume for CdSe and MnSe in both zinc-blende and rock-salt structures, HgSe in both zinc-blende and cinnabar phases, and ScSe in both NaCl and CsCl structures.

Table III-18: Calculated transition pressure (P_t) in GPa for CdSe, HgSe, ScSe and MnSe.

Compounds	P_t (GPa)	This study	Other calculations	Experiments
CdSe	$B3 \rightarrow B1$	2.622	3.5 [84]	3 [83]
HgSe	$B3 \rightarrow B9$	2.745	1.96 [90] 1.92 [22] 0.70 [88] 0.6 [89] 1.9 [89] 1.5 [87]	0.74-1.50 [85] 1.15 [2] 1.8 [87] 1.15-2.20 [91]
ScSe	$B1 \rightarrow B2$	40.838	53.65 [7] 52.0 [35] 53.0 [35] 47.4 [37]	
MnSe	$B1 \rightarrow B3$	0.652	1 [45]	

III-4.2 Influence of pressure on structural properties

The application of hydrostatic pressure significantly influences the structural parameters of crystalline solids, particularly the lattice constant, unit cell volume, and bulk modulus, as modifications result from the reduction of interatomic distances, which enhances the overlap of electronic orbitals and fortifies interatomic interactions.

To quantitatively describe this behavior, the relationship between pressure (P) and volume (V) can be fitted using the third-order Birch–Murnaghan equation of state (EOS):

$$P(V) = \frac{3}{2}B_0\left[\left(\frac{V_0}{V}\right)^{7/3} - \left(\frac{V_0}{V}\right)^{5/3}\right] \times \left\{1 + \frac{3}{4}(B_0' - 4)\left[\left(\frac{V_0}{V}\right)^{2/3} - 1\right]\right\} \qquad \text{III} - 13$$

Where V_0 is the equilibrium unit cell volume, B_0 is the bulk modulus at zero pressure, and B_0' is its first derivative with respect to pressure.

By fitting the calculated total energy-volume data to this EOS, we can obtain reliable values for the equilibrium volume, bulk modulus, and its pressure derivative for CdSe, HgSe, ScSe, and MnSe. These parameters offer key insights into the compressibility and mechanical response of the materials under different pressures.

Figure III-19 shows the variation of a_0 of CdSe, HgSe, ScSe and MnSe as a function of pressure. In all compounds, the lattice constant decreases progressively with rising pressure, which is consistent with the expected compressive behavior of crystalline solids under hydrostatic pressure. This monotonic reduction reflects the contraction of the crystal lattice as atoms are forced closer together, thereby increasing the material's stiffness.

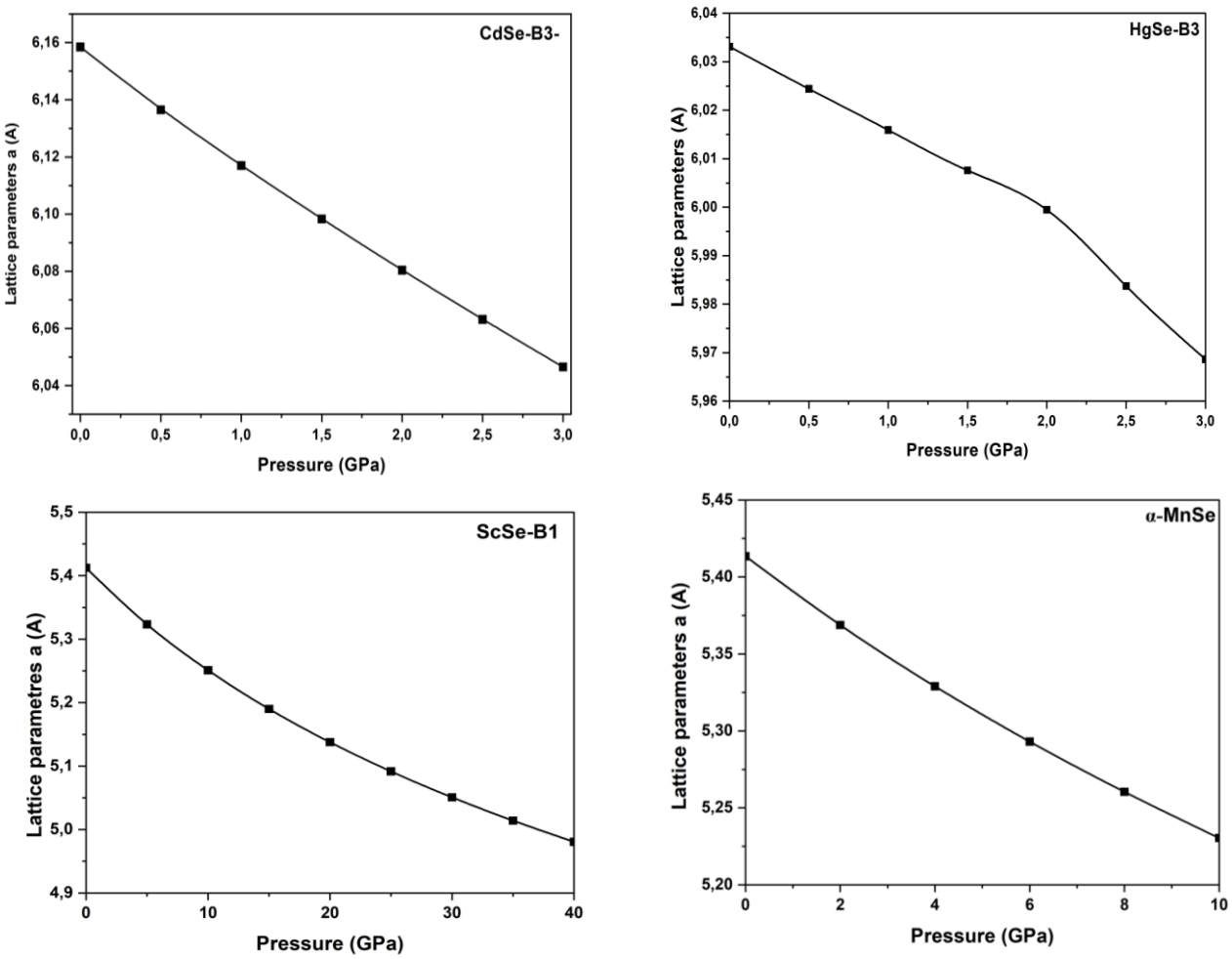

Figure III- 19: Variation of the unit cell parameter (a_0) as a function of pressure for CdSe, HgSe, ScSe and MnSe.

III-4.3 Influence of pressure on electronic properties

The band structures of CdSe and HgSe, as well as ScSe and MnSe, exhibit similar overall features at both zero and applied pressure, with only minor variations. CdSe, HgSe, and the spin-down channel of MnSe retain a direct band gap, while the spin-up channel of MnSe displays an indirect band gap. Additionally, pressure does not alter the metallic character of ScSe in the rock salt structure.

Figure III-20 illustrates the variation in band gap energy with pressure for CdSe, HgSe, ScSe and MnSe. The results indicate a linear rise in the band gap values of CdSe and HgSe as pressure rises, reflecting the strengthening of orbital overlap and reduced interatomic distances under pressure. From an application perspective, these results are of considerable significance. The expansion of the band gap in CdSe and HgSe under pressure indicates increased potential for high-pressure optoelectronic devices, especially in the visible to near UV spectrum. In contrast, MnSe exhibits different behavior: the spin-up band gap decreases slowly and linearly

with increasing pressure, whereas the spin-down band gap show a more pronounced linear decrease**,** indicating strong spin-dependent interactions under applied hydrostatic pressure**.** The pressure-induced reduction of the band gap in MnSe, along with its unique spin-up and spin-down behaviors, underscores its potential for spintronic applications, where adjustable spin dependent electrical characteristics are crucial.

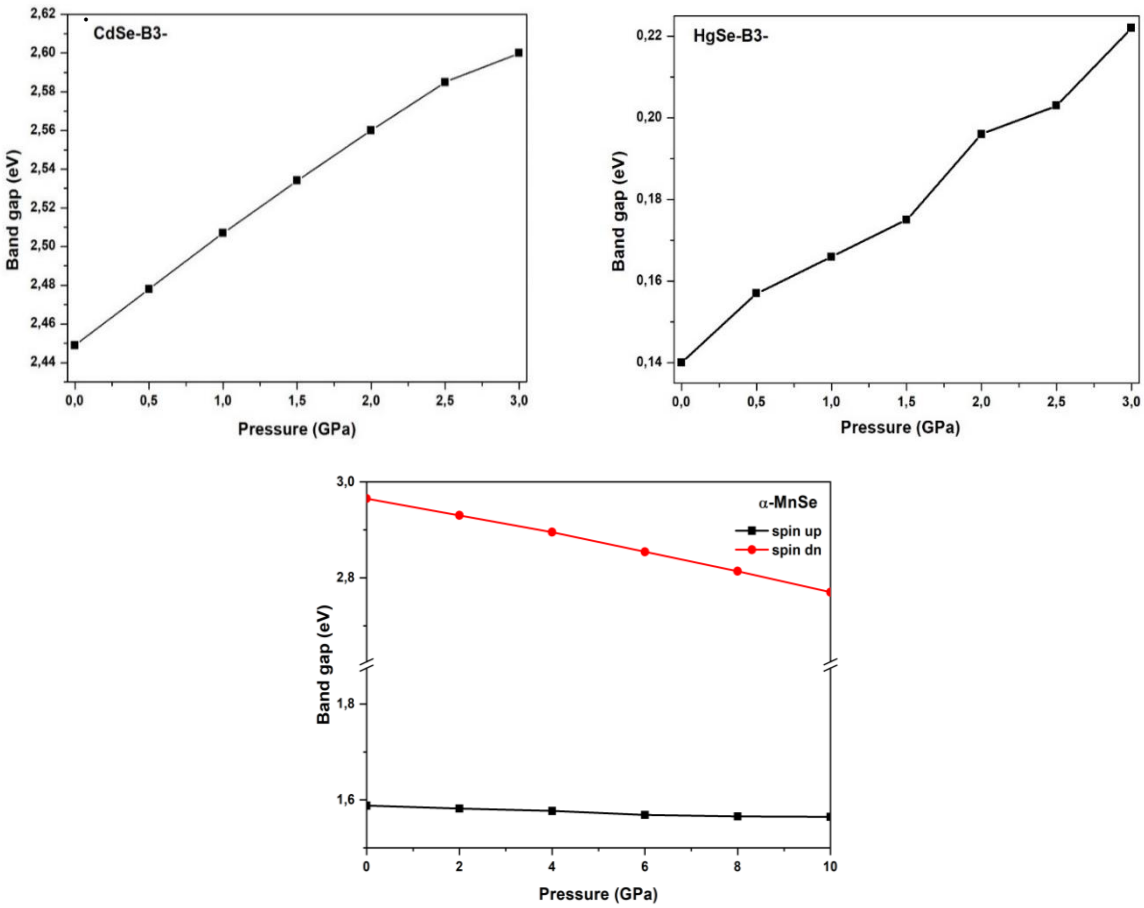

Figure III- 20: Variation of band gap of CdSe, HgSe and MnSe as a function of pressure.

III-4.4 Influence of pressure on optical properties

III-4.4.1 Dielectric function

Figures III-21, III-22, III-23, and III-24 depict the Re ε (ω) and Im ε (ω) parts of the dielectric function under different pressures as functions of photon energy for CdSe and HgSe in B3 structure, as well as ScSe and MnSe in B1 structure. Overall, both Re ε (ω) and Im ε (ω) parts of the dielectric function exhibit almost identical qualitative behavior, with minor variations. For the Re ε (ω) part of the dielectric function reaches a maximum near the absorption edge at lower frequencies, followed by regions of reduced intensity as a photon energy increases. The imaginary part, which is the most important property influencing the

optical characteristics of these materials, peaks shift to lower frequencies in the low frequency region and to higher frequencies in the high frequency region. The overall shape of both part resembles that of a harmonic oscillator confirming the expected optical response for CdSe, HgSe, ScSe, and MnSe under hydrostatic pressure. This behavior indicates that pressure modifies interband transition energies without altering the fundamental dielectric response of these compounds.

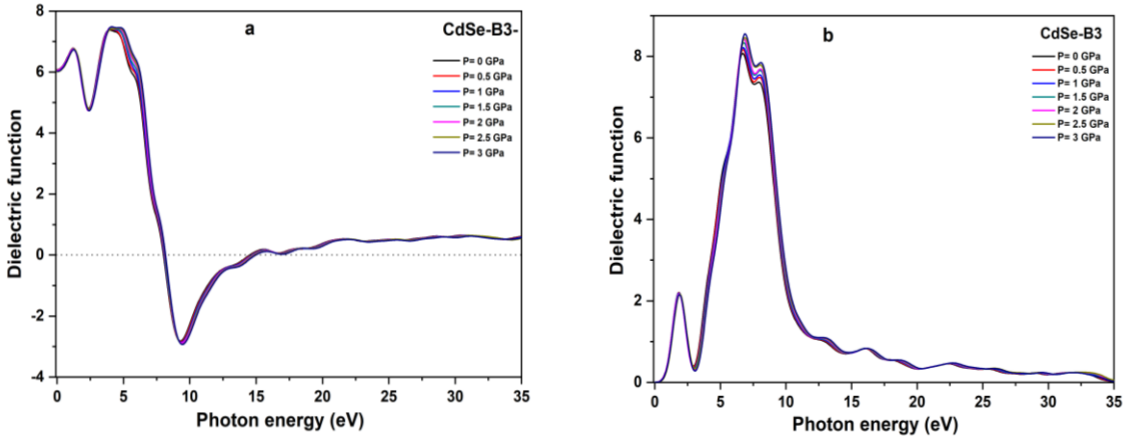

Figure III- 21: a) Real R $\boldsymbol{\varepsilon(\omega)}$ and b) imaginary Im $\boldsymbol{\varepsilon(\omega)}$ parts of the dielectric function at different pressures of CdSe as a function of photon energy.

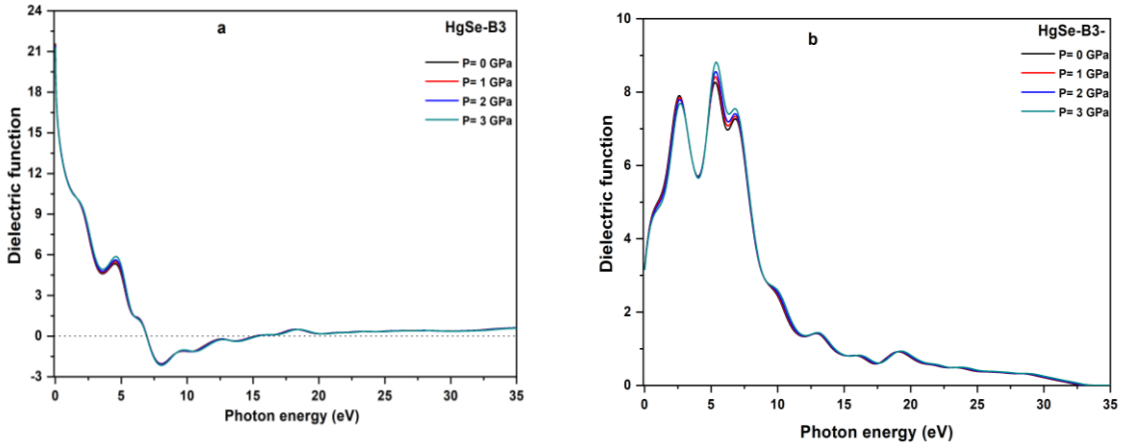

Figure III- 22: a) Real R $\boldsymbol{\varepsilon(\omega)}$ and b) imaginary Im $\boldsymbol{\varepsilon(\omega)}$ parts of the dielectric function at different pressures of HgSe as a function of photon energy.

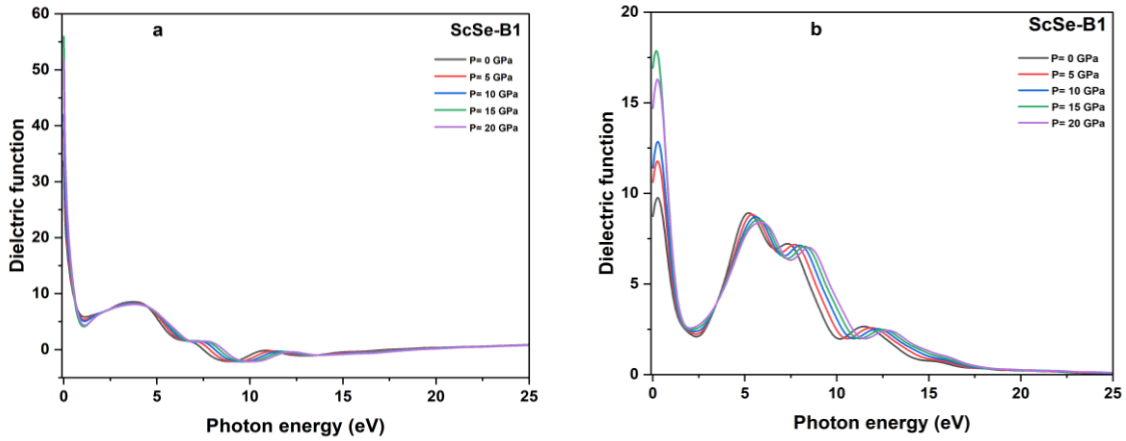

Figure III- 23: a) Real R $\boldsymbol{\varepsilon(\omega)}$ and b) imaginary Im $\boldsymbol{\varepsilon(\omega)}$ parts of the dielectric function at different pressures of ScSe as a function of photon energy.

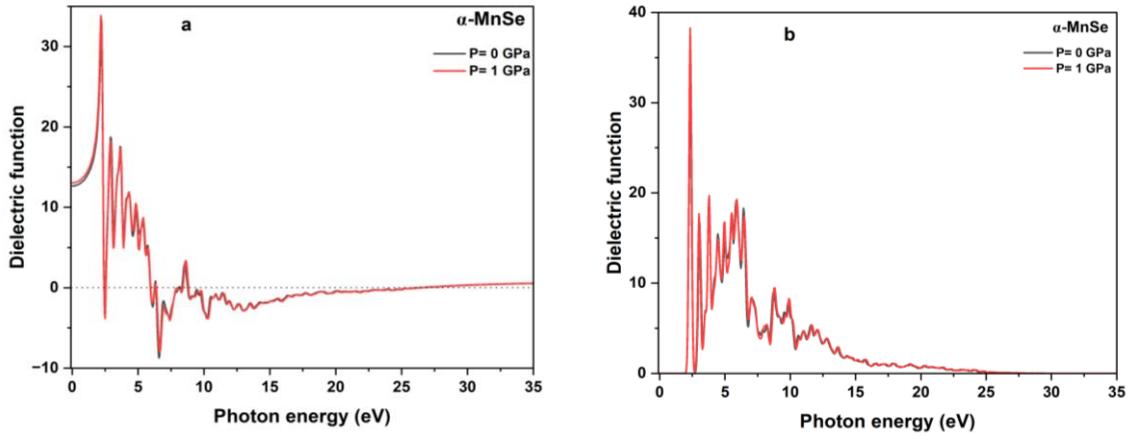

Figure III- 24: a) Real R $\boldsymbol{\varepsilon(\omega)}$ and b) imaginary Im $\boldsymbol{\varepsilon(\omega)}$ parts of the dielectric function at different pressures of MnSe as a function of photon energy.

III.4.4.2 Refractive index

Figures III-25, III-26, III-27, and III-28 illustrate the refractive index spectra n (ω) and k (ω) at different pressures as a function of photon energy of CdSe, HgSe, ScSe and MnSe, respectively. At zero pressure (0 GPa), distinct peaks are clearly observed in both the n (ω) and k (ω) parts of the refractive index. When hydrostatic pressure is applied, these peaks exhibit noticeable shifts: they move upward in the low frequency region while shifting downward in the high frequency region. This behavior reflects pressure induced modifications in the electronic band structure, particularly in the interband transition energies that strongly influence optical dispersion. The primary impact of pressure is observed in the static refractive index values, the refractive indices of CdSe, HgSe, ScSe and MnSe exhibit a slight but systematic increase with pressure. This trend is consistent with the pressure induced decrease in lattice

constants, which improve orbitals overlap and modifies the dielectric response, this increasing the refractive index at low photon energy. The n (ω) and k (ω) component of the refractive index exhibit nearly identical qualitative behavior under different pressure, with only minor variation between the compounds. This indicates that while pressure alter the magnitude and position of spectral features, it does not fundamentally change the overall optical response mechanism.

From an application standpoint, the tenability of the refractive index under hydrostatic pressure indicates the potential for adaptive photonic and optoelectronic devices, such as tunable lenses, modulators, and optical coatings. Materials like CdSe and HgSe, which already have established roles in optoelectronics, could particularly benefit from pressure tuned refractive control, whereas ScSe and MnSe might find application in high pressure optical systems or as reference materials in fundamental optic studies.

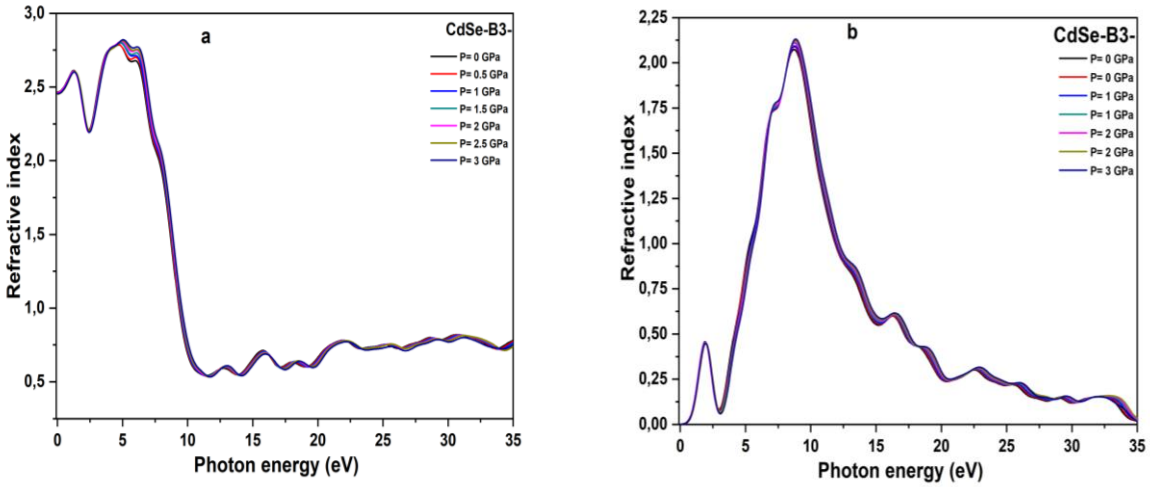

Figure III- 25: a) Real n($\boldsymbol{\omega}$) and b) imaginary k($\boldsymbol{\omega}$) parts of the refractive index at different pressures of CdSe as a function of photon energy.

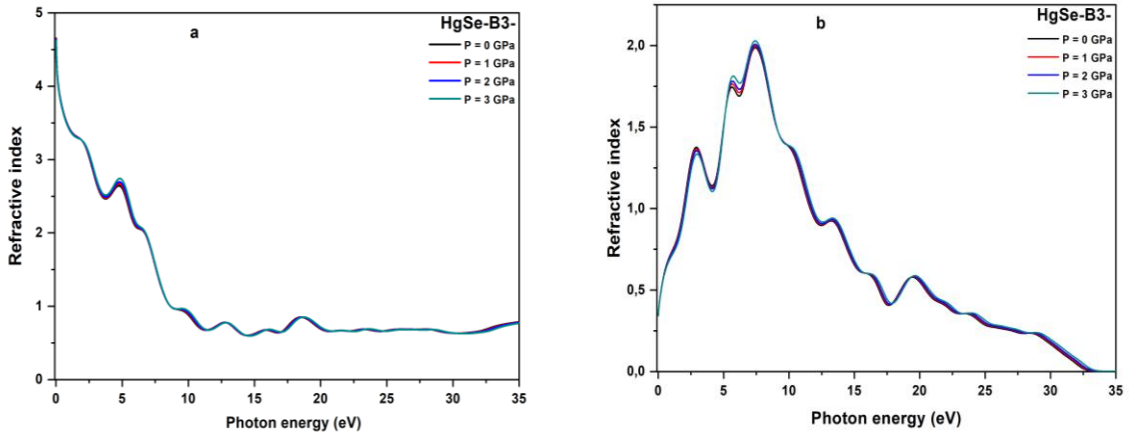

Figure III- 26: a) Real n($\boldsymbol{\omega}$) and b) imaginary k($\boldsymbol{\omega}$) parts of the refractive index at different pressures of HgSe as a function of photon energy.

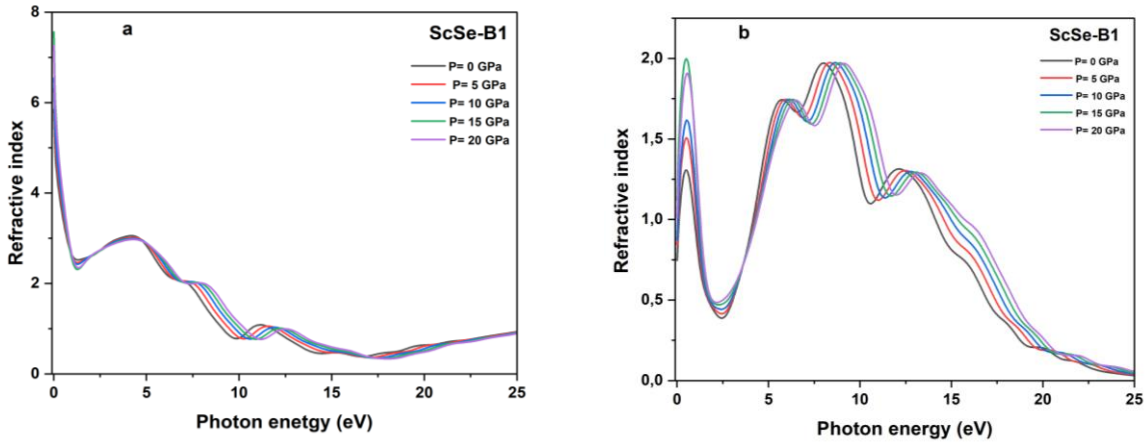

Figure III- 27: a) Real n(ω)) and b) imaginary k(ω) parts of the refractive index at different pressures of ScSe as a function of photon energy.

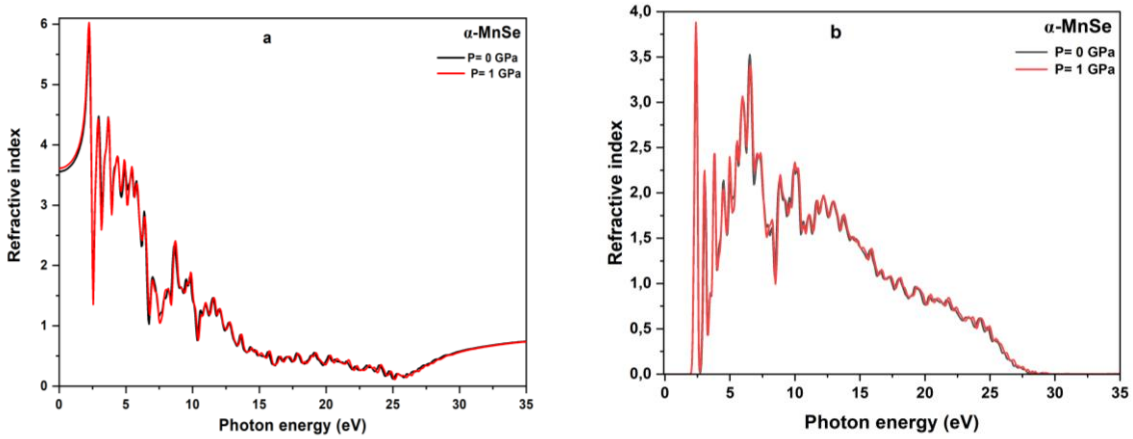

Figure III- 28: a) Real n(ω) and b) imaginary k(ω) parts of the refractive index at different pressures of MnSe as a function of photon energy.

III-4.4.3 Reflectivity

Figure III-29 illustrates the reflectivity spectra as a function of photon energy under different pressures of CdSe, HgSe, ScSe and MnSe. In all four compounds, the overall reflectivity trends remain similar under compression, indicating that pressure does not fundamentally alter their optical response mechanisms. However, slight differences are noticeable in the intensities and peak positions. The most prominent effect is the upward shift of peaks in the low energy region with increasing pressure. This shift is closely linked to the blue shift of interband transitions, caused by the pressure induced reduction in lattice properties and higher orbital overlap.

At higher photon energies, the reflectivity curves exhibit less susceptibility to pressure, suggesting that the deep electronic transitions are less impacted by lattice compression compared to low energy transitions near the band boundaries. The observed result implies that the optical reflectivity of these compounds can be regulated by external pressure, which could

be beneficial in photonic coatings, pressure sensors, or optical systems where controlled reflectance is needed.

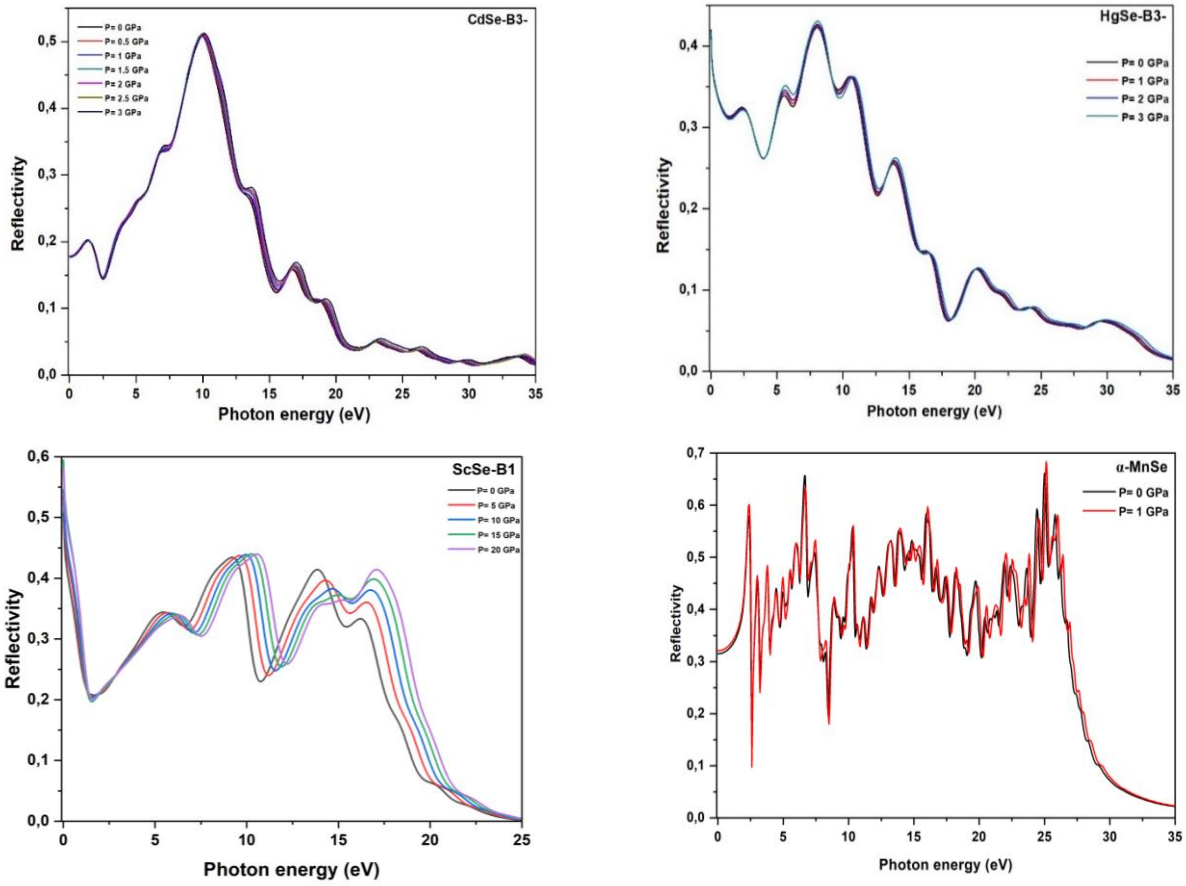

Figure III- 29: Reflectivity spectrum at different pressures of CdSe, HgSe, ScSe and MnSe as a function of photon energy.

III.4.4.4 Absorption

Before absorption occurs, light of a specific wavelength penetrates a depth into the material, specified by the optical absorption coefficient. Figure III-30 displays the absorption spectra of CdSe, HgSe, ScSe and MnSe, under different pressures as a function of photon energy. Across all compounds, the absorption curves demonstrate virtually identical qualitative patterns, with only modest variances in intensity and peak positions. The absorption coefficient increases slowly with photon energy, demonstrating the availability of higher energy electronic transitions. Moreover, the application of pressure boosts the absorption strength, resulting to greater values of the absorption coefficient. This pressure induced enhancement is ascribed to the greater overlap of electronic orbitals, which alters the band structure and promotes more efficient interband transitions. At low photon energies, absorption remains feeble until the fundamental absorption threshold is reached, corresponding to the transition from the valence

band maximum to the conduction band minimum. Beyond this threshold, absorption rises quickly with both photon energy and external pressure, demonstrating that compression effectively limits penetration depth and strengthens the material's ability to absorb radiation. These findings imply that the optical absorption of CdSe, HgSe, ScSe, and MnSe can be controlled by hydrostatic pressure, which may be helpful for applications in pressure sensitive optoelectronic devices, solar energy harvesting, and radiation shielding.

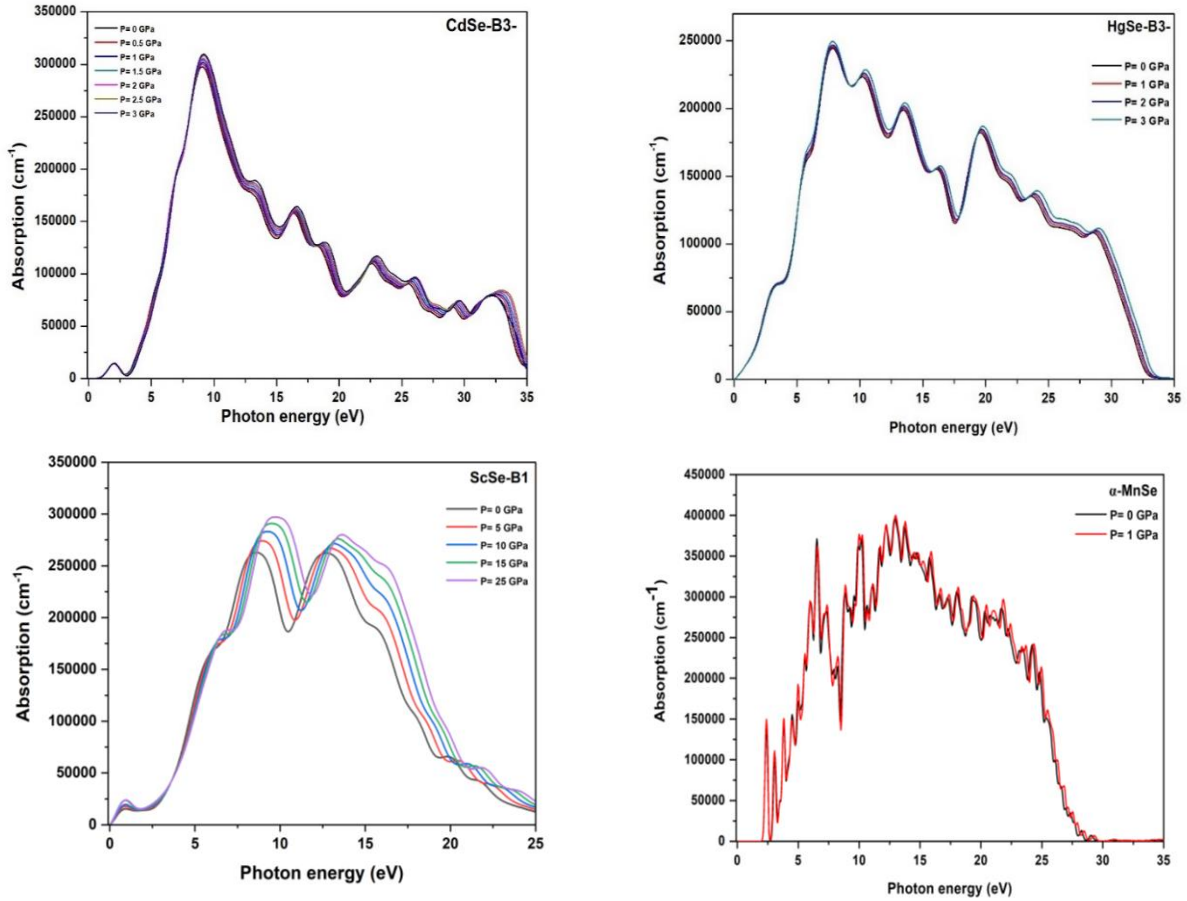

Figure III- 30: The optical absorption coefficient spectrum at different pressures of CdSe, HgSe, ScSe and MnSe as a function of photon energy.

III-4.5. Influence of pressure on elastic constants and mechanical stability

The elastic stiffness coefficient B_{ij} [92], which is obtained from the computed elastic constants C_{ij}. They are obtained as follow:

$$\begin{cases} B_{11} = C_{11} - P \\ B_{44} = C_{44} - P \\ B_{12} = C_{12} + P \end{cases} \qquad \text{III} - 14$$

Where P is the hydrostatic pressure.

Knowing these elastic constants enabled us to confirm mechanical stability, which requires that the entire elastic constant must be positive and the whole set of elastic constant C_{ij} should satisfy the Born stability criteria. These Criteria are outlined for a cubic crystal [79,80] :

$$\begin{aligned} M_1 &= B_{11} - B_{12} > 0 \\ M_2 &= B_{11} + 2B_{12} > 0 \\ M_3 &= B_{44} > 0 \end{aligned} \qquad \text{III} - 15$$

Figures III-31, III-32, III-33, and III-34 illustrate the variation of elastic constant C_{ij} and the corresponding mechanical stability criteria under pressure for CdSe, HgSe, ScSe and MnSe, respectively.

These figures indicate that the elastic constants C_{11} and C_{12} for CdSe, HgSe, ScSe, and MnSe increase linearly with rising pressure. This trend indicates expected stiffening of the lattice against longitudinal and compressive strains as atoms are forced closer together. In contrast, C_{44}, which governs shear rigidity, remains nearly constant with pressure for all compounds. Additionally, the Born mechanical stability criteria were subsequently assessed utilizing these elastic constants. Our findings demonstrate that CdSe, HgSe and MnSe exhibit mechanical stability across the entire investigated pressure range, as all three stability conditions are met. Conversely, ScSe in the rock-salt (B1) structure shows stability only up to approximately ~33 GPa. Beyond this critical pressure (~33.906), the stability conditions are no longer fulfilled, with the violation primarily arising from the C_{44} term. This breakdown signifies the onset of shear instability, marking the pressure at which ScSe loses its mechanical stability and may undergo a structural transformation.

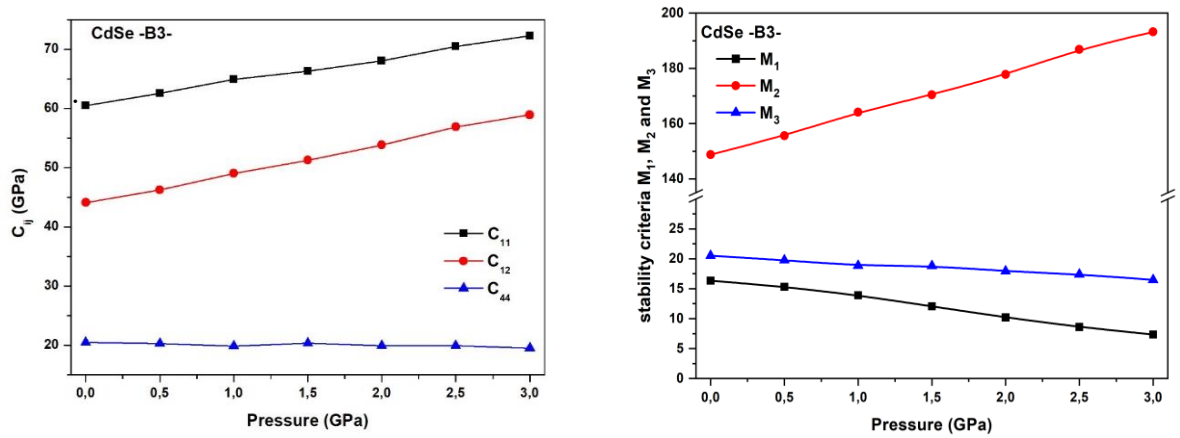

Figure III- 31: Variation of elastic constant and the mechanical stability criteria of CdSe as a function of pressure.

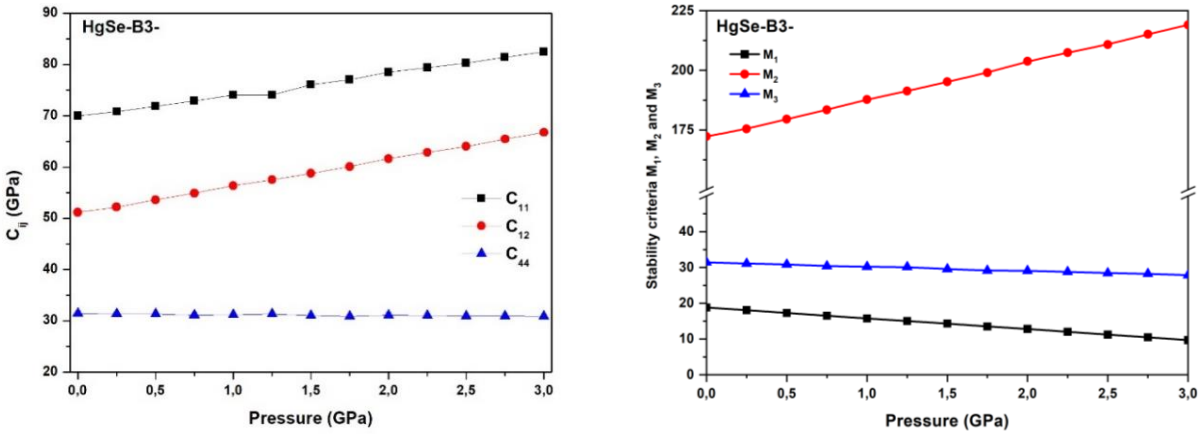

Figure III- 32: Variation of elastic constant and the mechanical stability criteria of HgSe as a function of pressure.

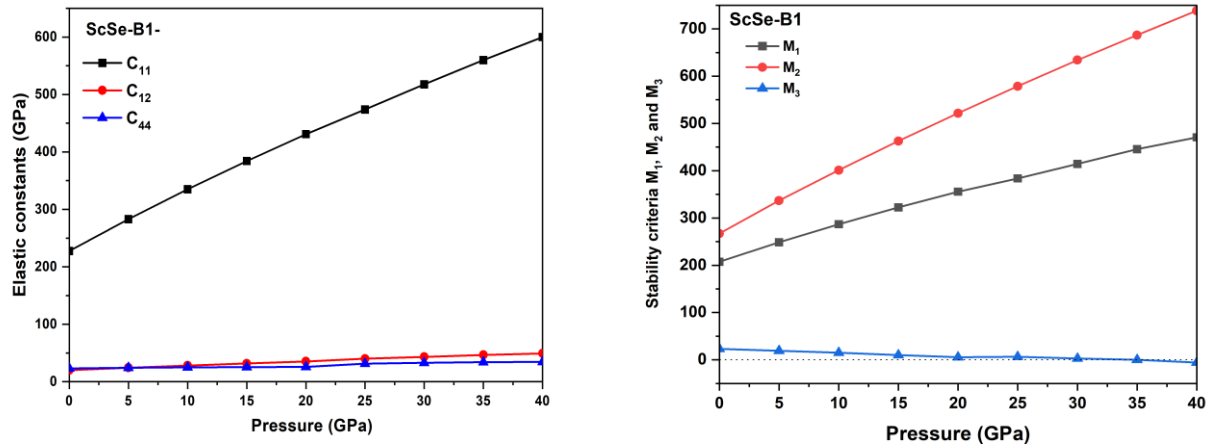

Figure III- 33: Variation of elastic constant and the mechanical stability criteria of ScSe as a function of pressure.

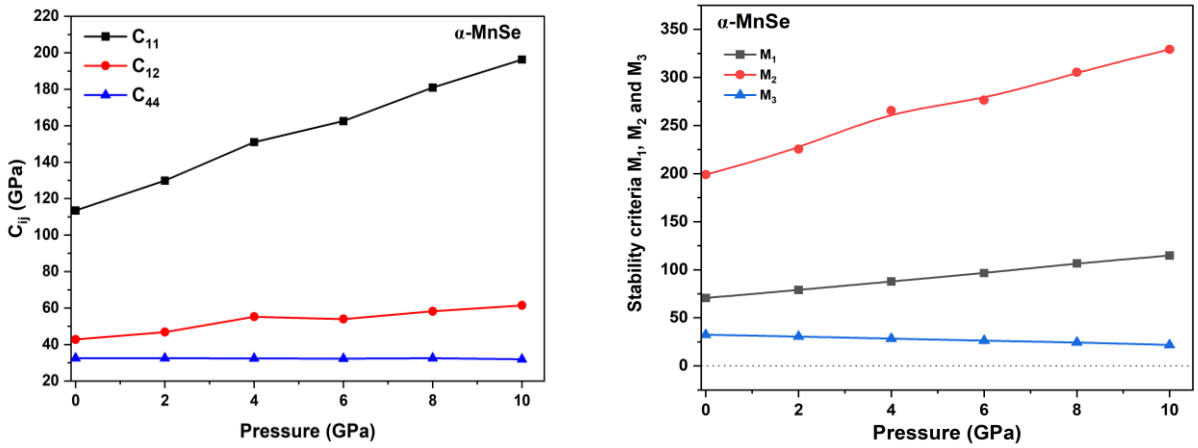

Figure III- 34: Variation of elastic constant and the mechanical stability criteria of MnSe as a function of pressure.

III-4.6 Influence of pressure on lattice dynamics

Figure III-35 displays the phonon dispersion diagrams of CdSe, HgSe and ScSe, calculated at both at zero and under hydrostatic pressure, with optimized lattice parameters along various high symmetry directions in the Brillouin zone (BZ). The phonon dispersion curve provide valuable insights into the vibrational properties and structural stability of these compounds. Importantly, The lack of imaginary (negative) frequencies throughout the whole Brillouin zone, both at ambient conditions and under pressure demonstrates that CdSe, HgSe and ScSe remain dynamically stable under compression. Their atomic lattices resist small perturbations, indicating strong vibrational stability.

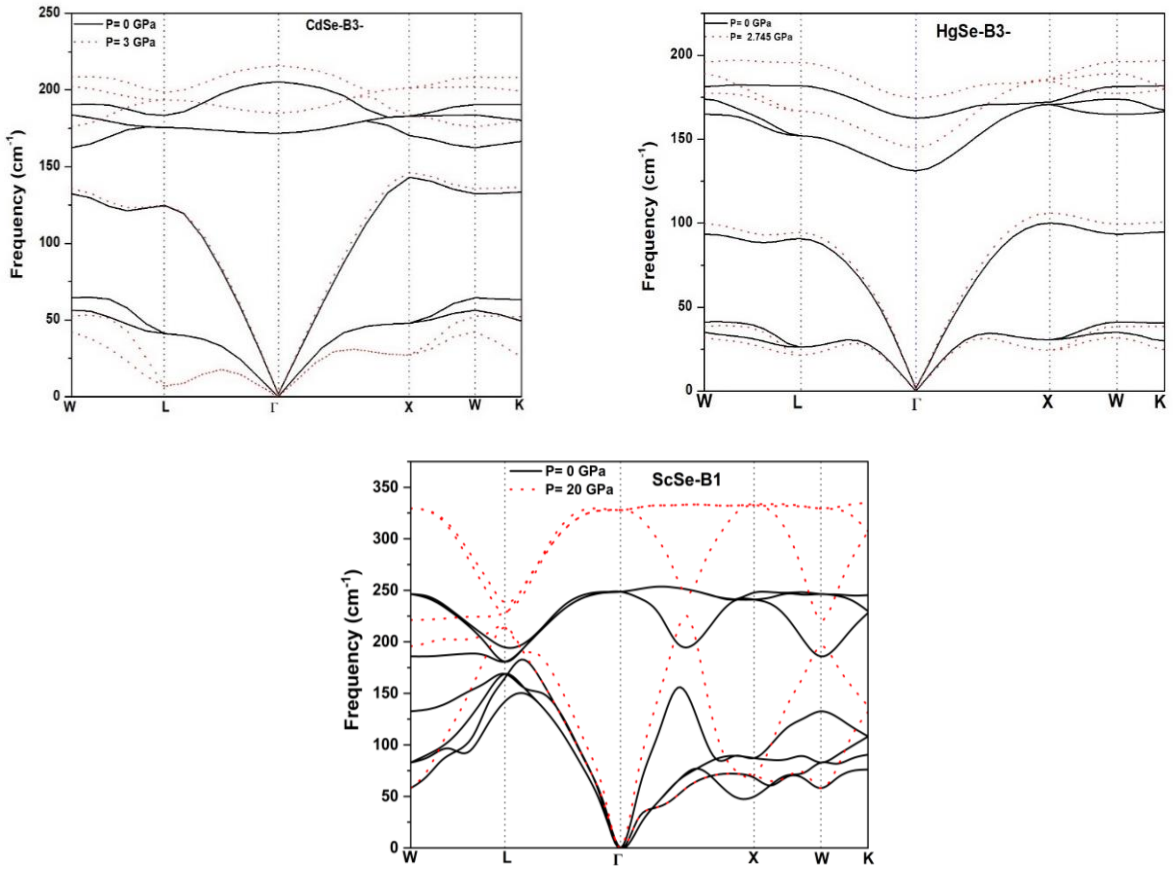

Figure III- 35: Phonon dispersion curves of CdSe, HgSe and ScSe.

III-4.7 Influence of pressure on thermodynamic properties

III-4.7.1 Influence of pressure on bulk modulus (B)

The bulk modulus (B) changes at various pressures as a function of temperature for CdSe, HgSe, ScSe and MnSe is depicted in Figure III-36. For CdSe, B decrease streadly with increasing pressure across the relevant pressure range. This behavior is typical of

semiconductors and suggests that CdSe retain thermomechanical stability under the applied pressure and temperature conditions. For HgSe, B falls with increasing temperature and pressure in the low pressure range (0–1 GPa). Yet, at higher pressures (1.5–3 GPa), the modulus falls with temperature up to ~400 K, beyond which it exhibits an anomalous rise. This abnormal behavior may suggest the onset of pressure temperature induced instability in HgSe. Moreover, for ScSe, B decreases with temperature at pressures up to 20 GPa, consistent with expected thermal softening. At higher pressures (above 20 GPa), B increases with temperature, deviating from normal thermodynamic behavior. This trend suggests the possibility of phase instabilities or transitions in ScSe under these conditions. For MnSe, B decreases with temperature at low pressures (0–2 GPa). At higher pressures (4–10 GPa), however, B instead increases with temperature, which again points to anomalous behavior and potential instability of the MnSe phase under combined high pressure and high temperature conditions.

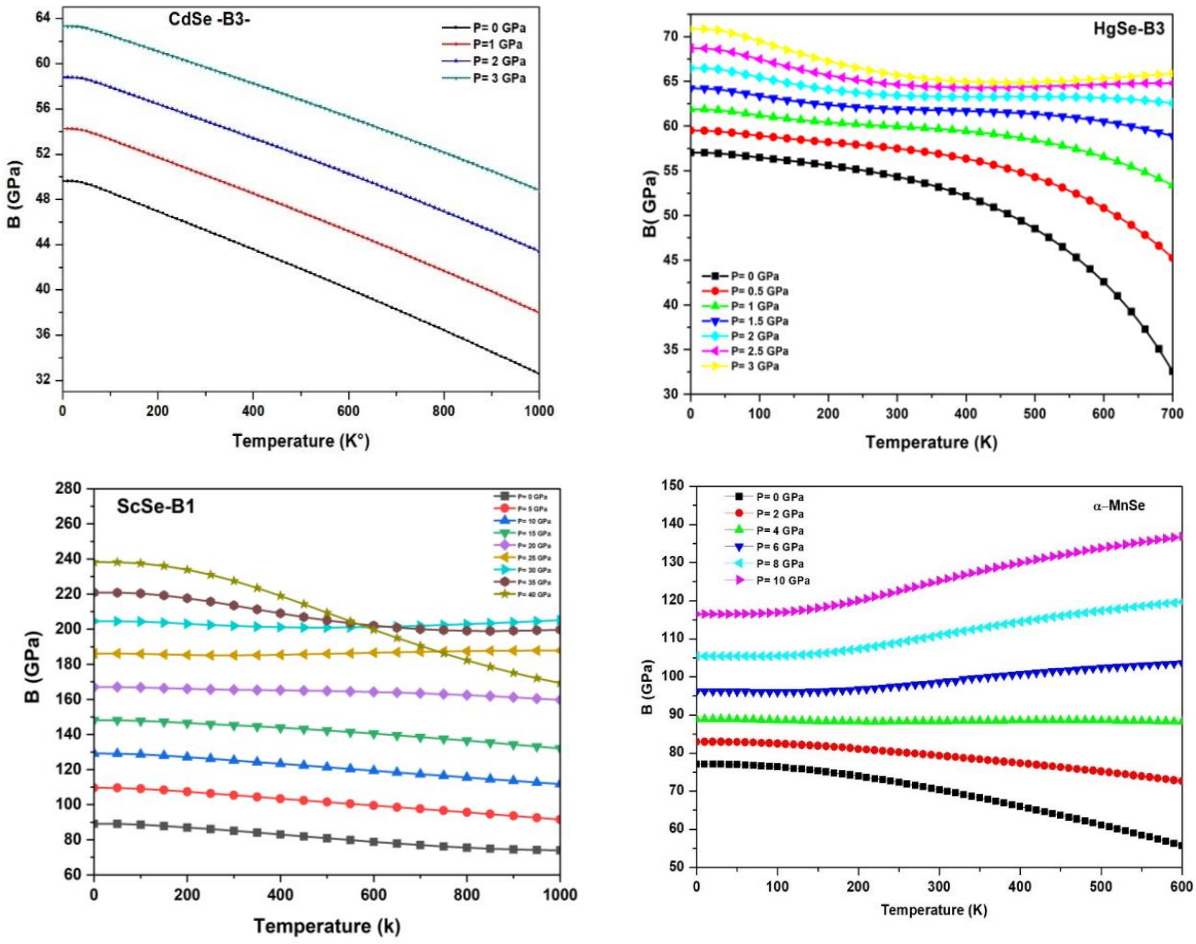

Figure III- 36: Bulk modulus variation at different pressures of CdSe, HgSe, ScSe and MnSe as a function of temperature.

III-4.7.2 Coefficient of thermal expansion (α)

Figure III-37 shows the variation of the thermal expansion coefficient (α) with temperature at different pressures for CdSe, HgSe, ScSe and MnSe. For CdSe, α demonstrates a monotonically increasing trend with increasing temperature, with the coefficient continuing to expand at higher temperatures. This constant result suggests the thermomechanical stability of CdSe under the studied pressure and temperature ranges. Moreover, for HgSe, α increase monotonically with temperature at low pressures (0–1 GPa), but at higher pressures, the behavior becomes inconsistent: the coefficient begins to drop at rising temperatures, suggesting a breakdown in the predicted thermal expansion response. A similar anomaly is reported for ScSe, which shows monotonically increasing α from 0 to 20 GPa, but deviates from this pattern at higher pressures, with the coefficient falling at high temperatures. For MnSe, α increases consistently with temperature at low pressures (0–2 GPa), but again, abnormal behavior develops at higher pressures, where α begins to decrease with temperature. These results collectively suggest that while CdSe remains stable, the compounds HgSe, ScSe, and MnSe show evidence of pressure temperature induced instabilities in their thermal expansion behavior. Such anomalies may be indicative of incipient phase transitions or anharmonic lattice effects under extreme conditions.

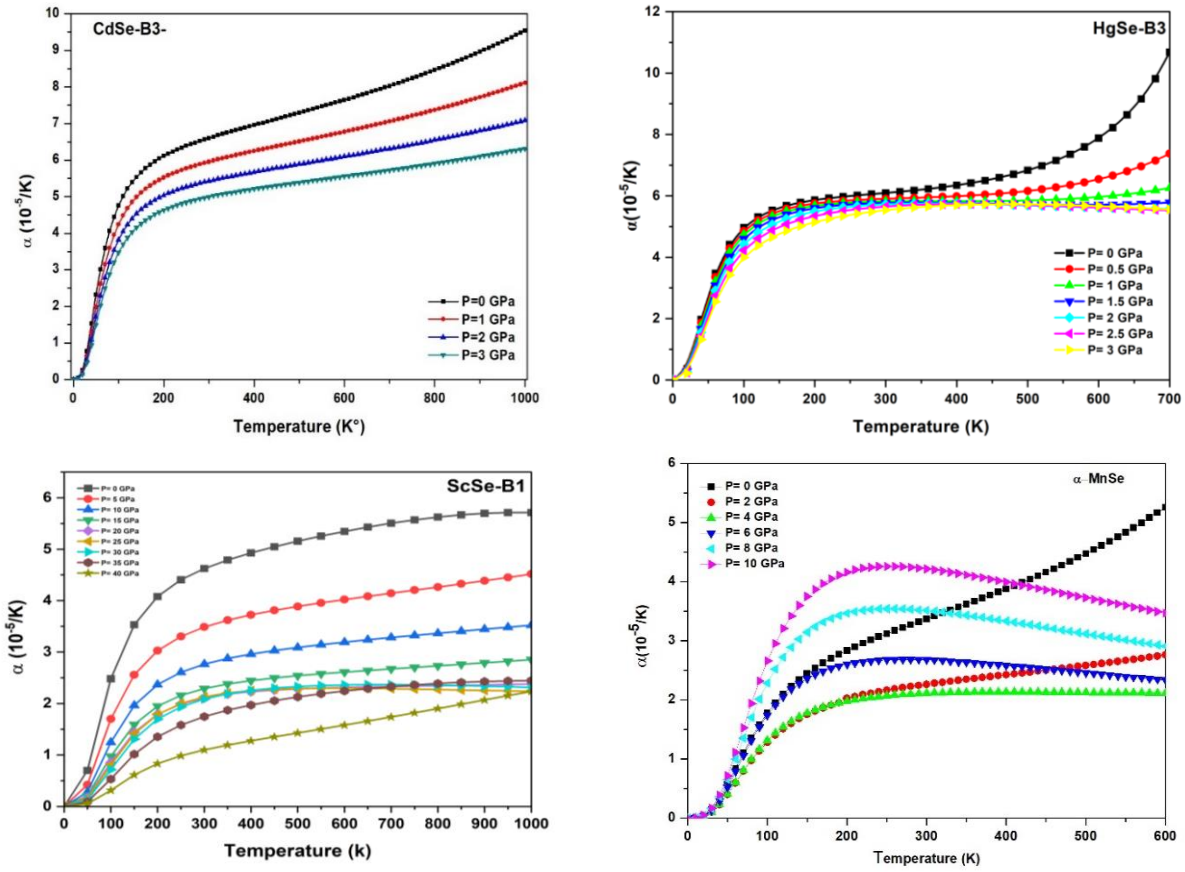

Figure III- 37: Variation of the thermal expansion coefficient (α) at different pressures of CdSe, HgSe, ScSe and MnSe as a function of temperature.

III. 4.7.3 Specific heat capacity (C_V)

The heat capacity is essential for many applications and provides important details about its vibrational properties. In particular, the specific heat capacity C of a material is a fundamental thermodynamic parameter that reflects the phonon density, offering crucial insights into its vibrational properties and applications. Figure III-38 shows the evolution of C_V as a function of temperature under different pressures for CdSe, HgSe, ScSe and MnSe. This figures shows that C_V increases exponentially with temperature at low T: exhibiting an exponential like growth up to ~300 K for CdSe and MnSe, ~400 K for HgSe, and ~500 K for ScSe. This low temperature behavior is consistent with the Debye T^3 law, which describes the phonon contribution to C_V in this regime. At higher temperatures, the increase in C_V gradually slows down, and the heat capacity approaches the Dulong-Petit limit ($C_V=3nR$). This saturation behavior is clearly observed for all four compounds (CdSe, HgSe, ScSe, and MnSe), confirming that their high temperature thermodynamic behavior is dominated by lattice vibrations, as expected from classical theory.

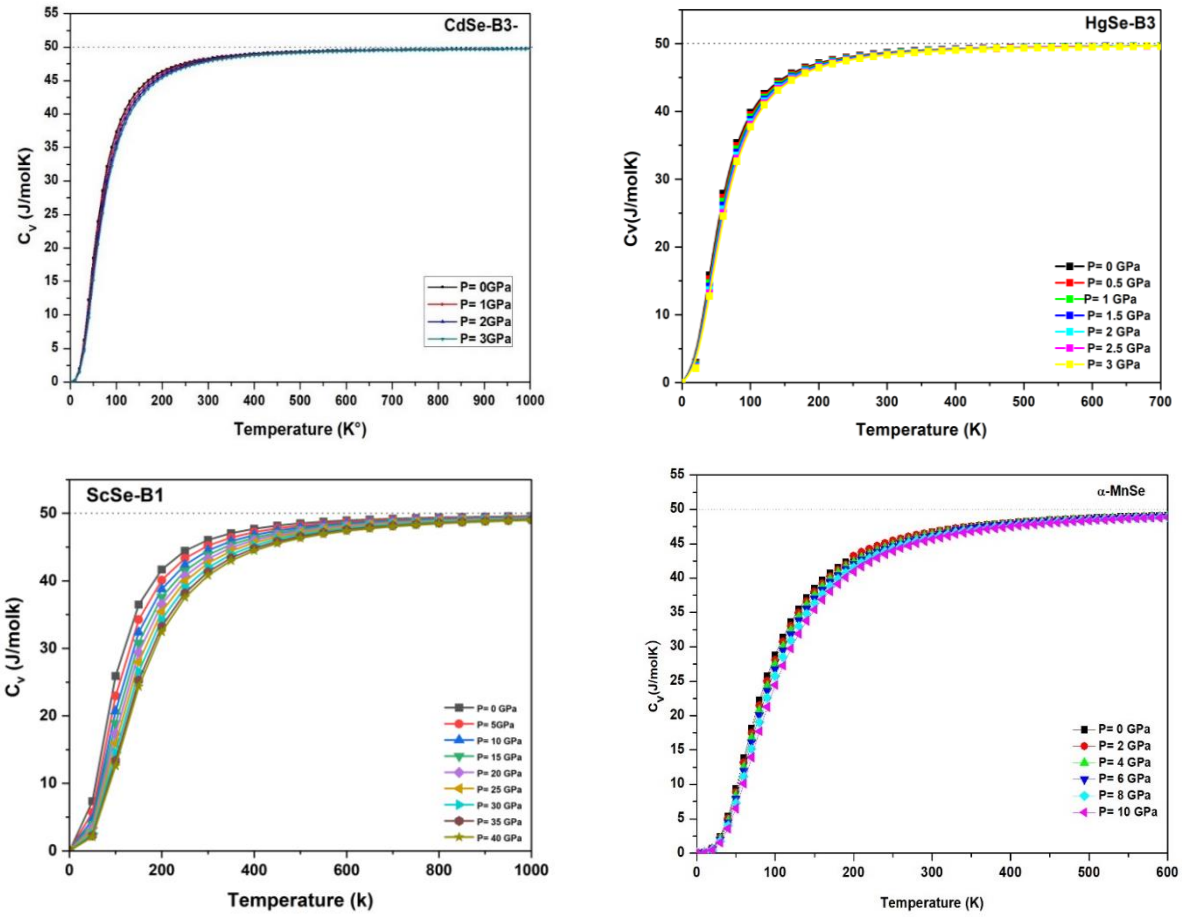

Figure III- 38: Variation of the heat capacity at constant volume C_V at different pressures of CdSe, HgSe, ScSe and MnSe as a function of temperature.

III-5 High-pressure phases

III-5.1 Structural properties

In this part, we investigate the high-pressure phase properties of the studied compounds. Specifically, CdSe is examined in the rock salt (B1) structure with space group $Fm\bar{3}m$ (225), where Cd atoms occupy the 4a (0, 0, 0) positions and Se atoms occupy the 4b (1/2, 1/2, 1/2) sites. HgSe is analyzed in the cinnabar (B9) phase with space group $P3_121\bar{}$(154), where Hg atoms are located at the 3a sites with fractional coordinates by the internal parameters u_1: (u_1, 0, 0), (0, u_1, 1/3) and (-u_1, -u_1, 2/3), while the Se atoms occupy the 3b sites defined by internal parameter u_2: (u_2, 0, 1/2), (0, u_2, 5/6), and (u_2, u_2, 1/6). In addition, ScSe is considered in the CsCl type (B2) structure with space group $Pm\bar{3}m$ (221), where Sc atoms occupy the 1a positions (0, 0, 0) and the Se atoms occupy the 1b position (1/2, 1/2, 1.2). Finally, MnSe is studied in the zinc-blende (β) structure with space group $F\bar{4}3m$ (216), where Mn atoms occupy the 4a (0, 0, 0) positions, and Se atoms occupies the 4c (1/4, 1/4, 1/4) sites, as shown in Figure III-39.

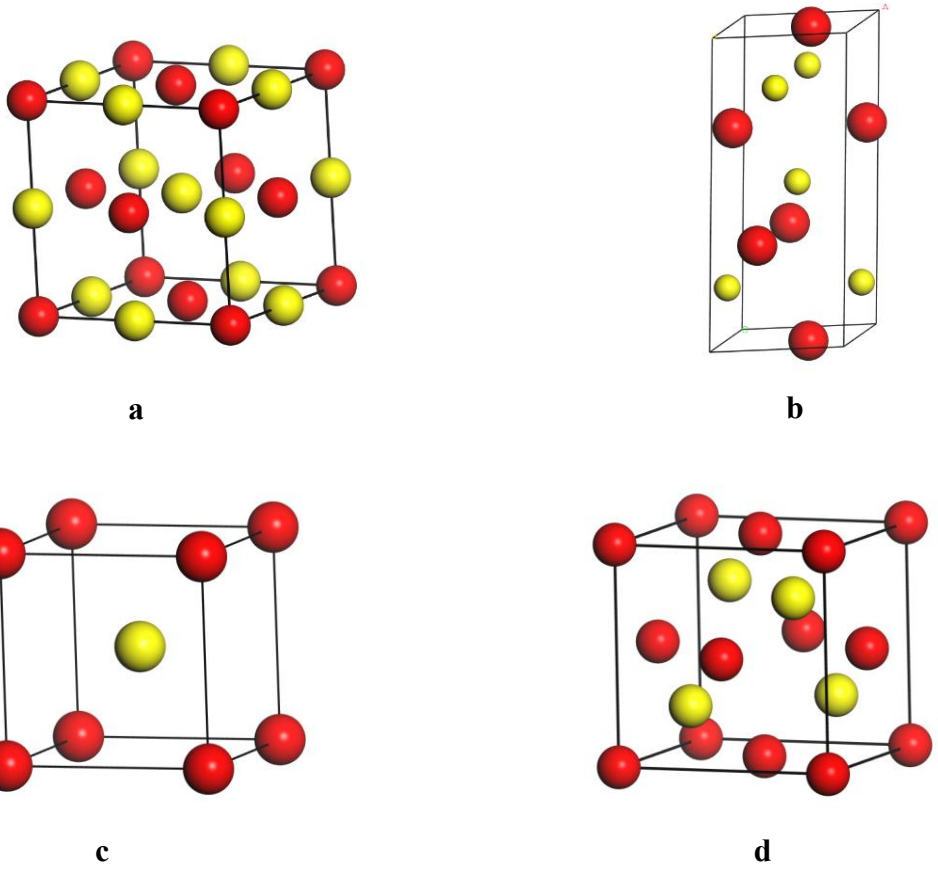

Figure III- 39: Crystalline structure: a) CdSe in the rocksalt (B1) structure, b) HgSe in the cinnabar (B9) phase, c) ScSe in the CsCl type (B2) structure and d) MnSe in the zinc-blende (β) structure.

Figure III-40 illustrate total energy changes as a function of volume E (V) for CdSe in the rock-salt (B1) structure, HgSe in the cinnabar phase (B9) , ScSe in the CsCl type (B2) structure, and MnSe in the zinc-blende (β) structure.

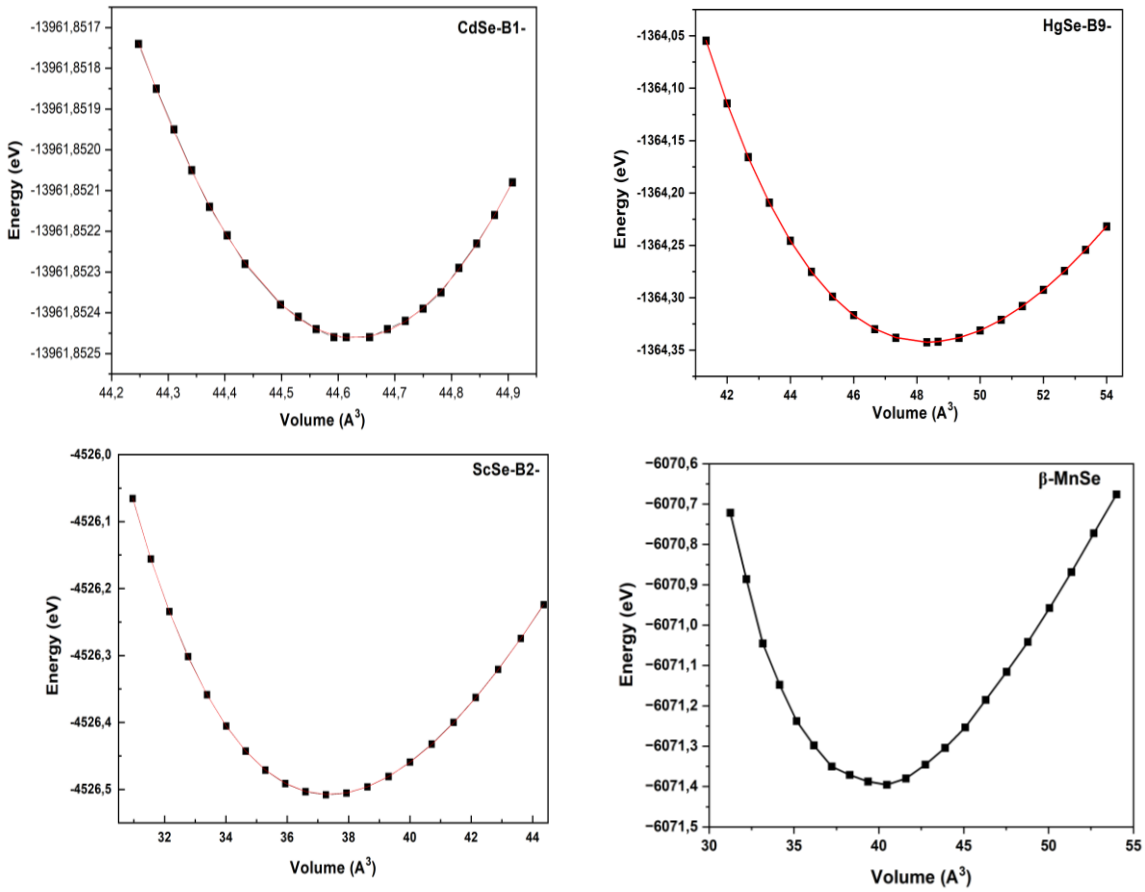

Figure III- 40: Total energy changes as a function of the volume of CdSe in the rock salt (B1) structure, HgSe in the cinnabar phase (B9), ScSe in the CsCl type (B2) structure, and MnSe in the zinc blende (β) structure.

The energy-volume curves were fitted to the Murnaghan equation of state to determine the fundamental structural characteristics [14], including the lattice parameters (a_0, c_0), the bulk modulus (B_0), and its pressure derivative (B'). A brief overview of the results, which are included in the comparison with experimental data from other studies, is presented in Tables III-19, III-20, III-21, and III-22 for CdSe, HgSe, ScSe, and MnSe, respectively.

The calculated lattice parameters (a_0) of CdSe match the experimental results [29] and are more accurate than other calculations reported in the literature [30]. However, there are no comparable experimental results for the bulk modulus (B_0) and its derivative (B′). Similarly, for HgSe, the calculated (a_0 and c_0) are consistent with the experimental measurements [2,85], but no experimental data exist for (B_0) or (B′). Additionally, the calculated lattice parameter (a_0) for ScSe has no experimental comparison, although our value for ScSe agrees well with the literature [7,9,35]. Furthermore, no experimental results are available for B_0 or its derivative (B′); however, our values closely match those reported [9,35]. Moreover, the lattice parameters

(a_0) for MnSe are very close to experimental data, with less than a 1% deviation from references [94], but there are no experimental results for (B_0). Our values again align well with those reported in the literature [25,45].

Table III- 19: Structural properties, including lattice parameters (a_0), bulk modulus (B_0), and its derivative B′ of CdSe.

Compound	Parameters	This study	Other calculations	Experiments
CdSe	a_0 (A°)	5.685	5.5762 [30]	5.71 [29]
	B_0 (GPa)	67.515	84.32 [30]	
	B'	4.520	4.8022 [30]	

Table III- 20: Structural properties, including lattice parameters (a_0), bulk modulus (B_0), and its derivative B′ of HgSe.

Compound	Parameters	This study	Other calculations	Experiments
HgSe	a_0 (A°)	4.180	4.481 [88] 4.179 [88] 4.514 [22]	4.174 [2] 4.120 [85]
	c_0 (A°)	9.550	9.499 [88] 9.708 [88] 9.970 [22]	9.626 [2] 9.560 [85]
	B_0 (GPa)	50.664	53 [88] 9.11 [22]	
	B'	4.926	10.85 [22]	

Table III- 21: Structural properties, including lattice parameters (a_0), bulk modulus (B_0), and its derivative B′ of ScSe.

Compound	Parameters	This study	Other calculations	Experiments
ScSe	a_0 (A°)	3.343	3.338 [9] 3.302 [7] 3.299 [35] 3.2531 [37]	
	B_0 (GPa)	92.523	92.41 [9] 98.466 [7] 90.35 [35] 99.7 [37]	
	B'	4.183	3.84 [9] 3.961 [7] 4.03 [37]	

Table III- 22: Structural properties, including lattice parameters (a_0), bulk modulus (B_0), and its derivative B′ of MnSe.

Compound	Parameters	This study	Other calculations	Experiments
MnSe	a_0 (A°)	5.870	5.806 [25] 5.92 [45] 5.85 [45] 5.85 [45]	5.88 [93]
	B_0 (GPa)	55.546	47.5 [25] 49.75 [45] 61.76 [45] 62.70 [45]	
	B'	4.563	3.73 [25] 5.62 [45] 5.90 [45] 5.92 [45]	

III-5.2 Electronic properties

III-5.2.1 Band structure

Figures III-41 illustrate the energy bands of CdSe, HgSe, ScSe and MnSe obtained through the GGA-PBEsol approximation.

For CdSe, the calculation reveals an indirect band gap (L-X) with a value of 0.363 eV. In the case of HgSe, the system also exhibits an indirect band gap, slightly larger at 0.455 eV. By contrast, ScSe displays metallic behavior with no energy gap, as both the CBM and VBM intersect the Fermi level. Additionally, for MnSe, both spin channels show semiconducting properties. The spin-up channel has a direct band gap (Γ-Γ), with both the CBM and VBM located at the Γ point, and a band gap value of 0.248 eV. Meanwhile, the spin-down channel exhibits an indirect band (Γ-X) with a much larger band gap of 3.07 eV. Table III-23 presents the results comparing CdSe, HgSe, ScSe, and MnSe, calculated using the GGA PBE-sol approximation.

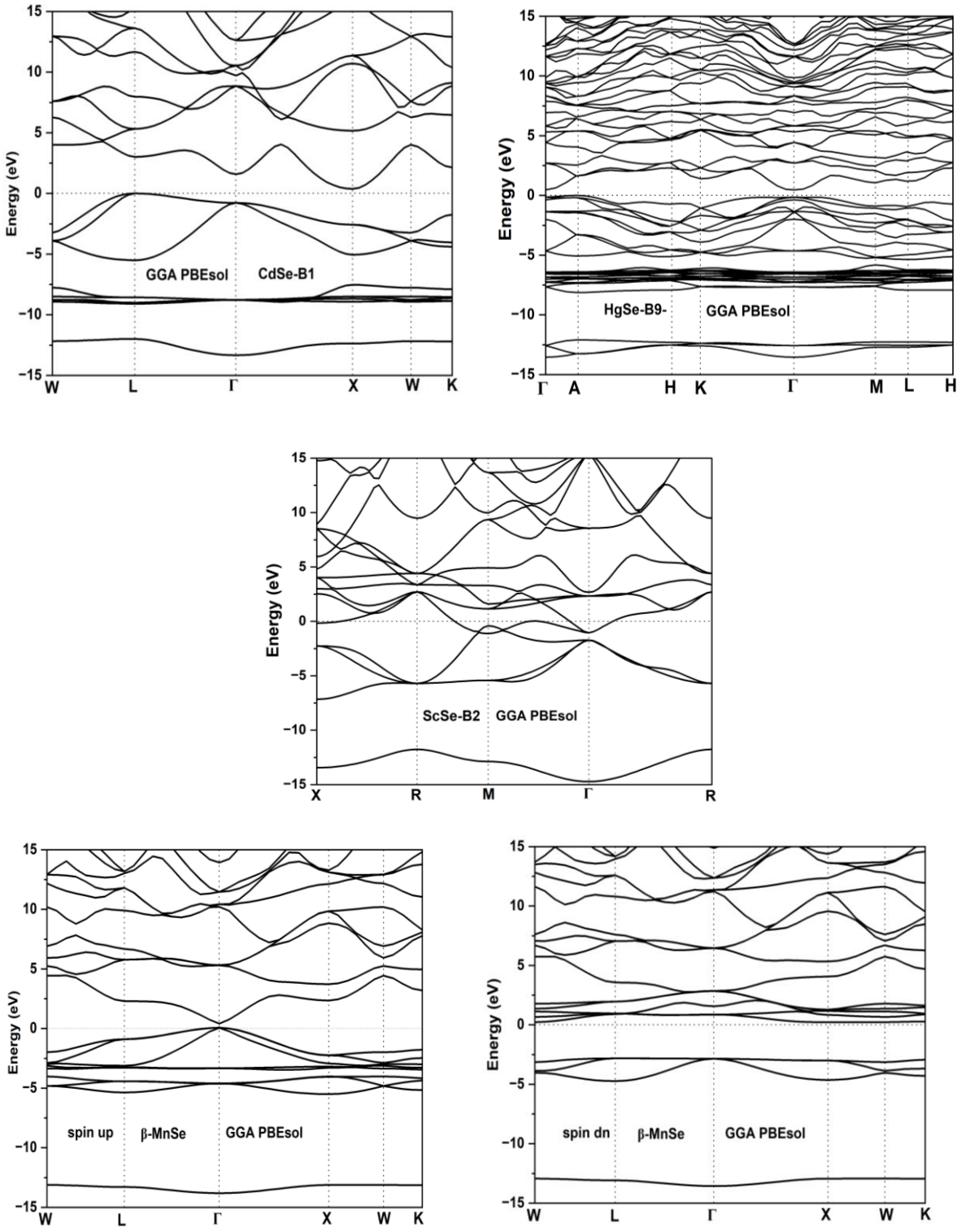

Figure III- 41: Band structure of the CdSe, HgSe, ScSe and MnSe obtained by GGA-PBEsol.

Table III- 23: Fundamental gap energy of CdSe, HgSe, ScSe, and MnSe obtained using GGA-PBEsol.

Compounds		This study (eV)	Other calculations	Experiments
CdSe		0.364		
HgSe		0.455		
ScSe		0		
MnSe	Spin up	0.248		
	Spin dn	3.070		

III-5.2.2 Density of states

Figure III-42 shows the total (TDOS) and partial (PDOS) density of states of CdSe, HgSe, ScSe, and MnSe, all obtained using the GGA-PBEsol approximation.

We observed three distinct peaks for CdSe, the first peak, located around -11 eV below the Fermi level, which consists entirely of Se-s orbitals. Above this, the Cd-d orbital band is found at -8 eV. The third peak, primarily composed of Se-p orbitals, is located near the Fermi level at approximately -3.5 eV, with a minor contribution from Cd-s orbitals. The conduction band is composed mainly of Cd-p orbitals, with a minor contribution from Cd-s orbitals. Moreover, for HgSe, the existence of four clearly defined regions is evident. The first region is about -13.5 eV below the Fermi level and is composed entirely of Se-s orbitals. Above this, the Hg-d orbital band appears with a slight contribution from Se-p orbitals around -7.5 eV. The third region consists entirely of Hg-s and Se-p orbitals around -6 eV, while the fourth region is mainly Hg-p orbitals near -5 eV. The conduction band is primarily composed of Hg-p orbitals, with a small contribution from s orbitals. Furthermore, For ScSe, the lowest bands are due to Se-s states located around -15 eV, and the Sc-d bands are from -5 eV with minor contributions from Sc-p and Se-s orbitals. The metallic character of ScSe is primarily due to the Sc-d states with small contributions from Sc- p states at the Fermi level. Moreover, for MnSe, the two lowest bands are Se-p and Mn-d hybridized, while the higher bands correspond to Se-s states. Below the Fermi level, the spin-down Se-p bands extend to higher energies. In contrast, the spin-up Mn-p and Mn-d bands. Above the Fermi level shift downward due to strong Mn-p states. As a result, there are fewer occupied spin-down states and more occupied spin-up states. The spin-up Mn-p bands are the main contributors near the Fermi level.

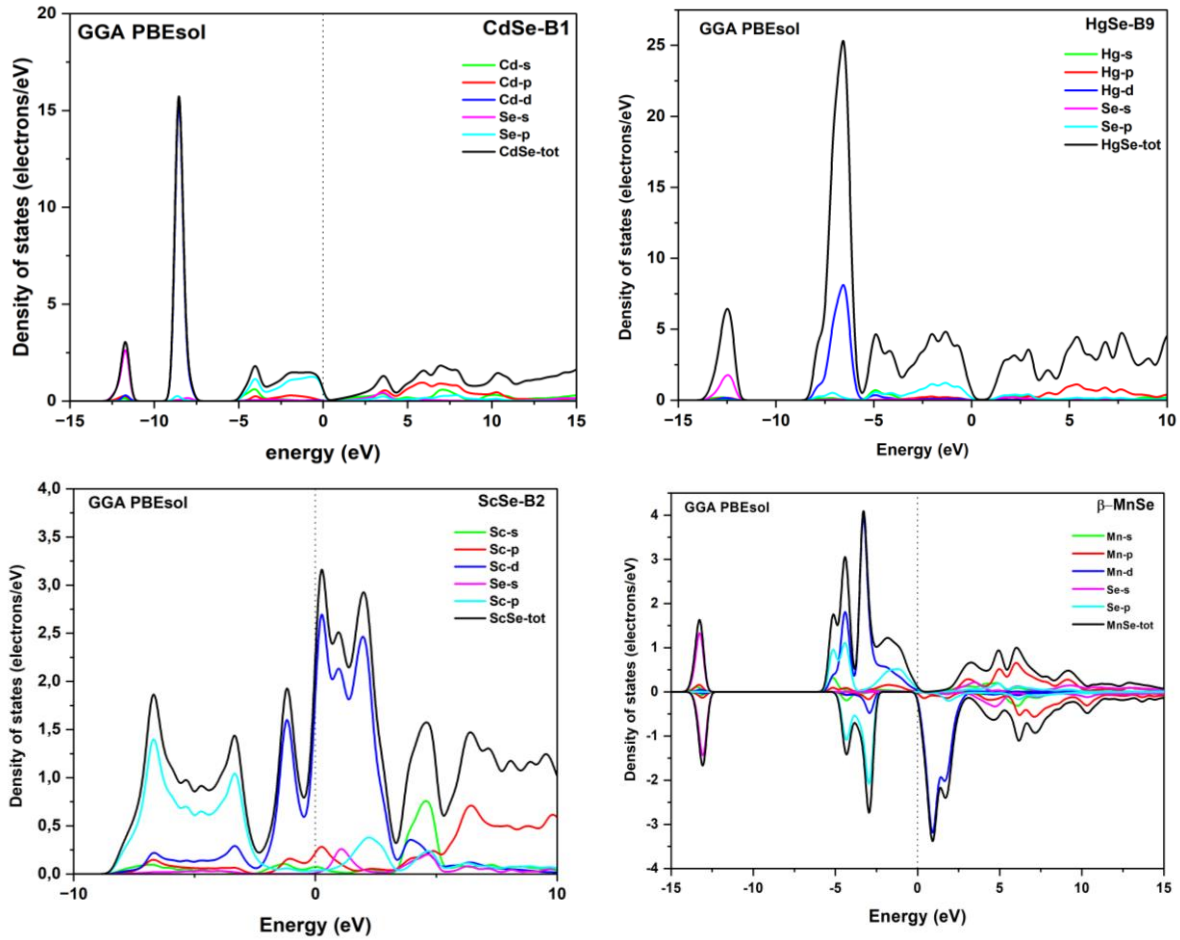

Figure III- 42: Total and partial density of states of CdSe, HgSe, ScSe and MnSe obtained by GGA-PBEsol.

III-5.3 Effect of exchange correlation

III-5.3.1 Band structure

Figures III-43 depict the energy bands of CdSe, HgSe, ScSe, and MnSe as obtained using the B3LYP hybrid functional.

For CdSe, an indirect band gap (L-X) is observed, with a value of 1.667 eV. Similarly, HgSe also exhibits an indirect band gap with value of 1.401 eV. Moreover, for ScSe, the result confirm its metallic nature, as both CBM and VBM intersect the Fermi level, leaving no band gap. Furthermore, for MnSe, both spin channels display semiconductor behavior. The spin-up channel has a direct band gap (Γ-Γ) with both CBM and VBM located at the Γ point, with a band gap value of 2.51 eV. Meanwhile, the spin-down channel features an indirect band gap (Γ-X) with a significantly larger value of 4.84 eV. The corresponding results are summarized in Table III-24, which compares the energy gaps of CdSe, HgSe, ScSe, and MnSe in their respective high-pressure phases as calculated using the B3LYP hybrid functional.

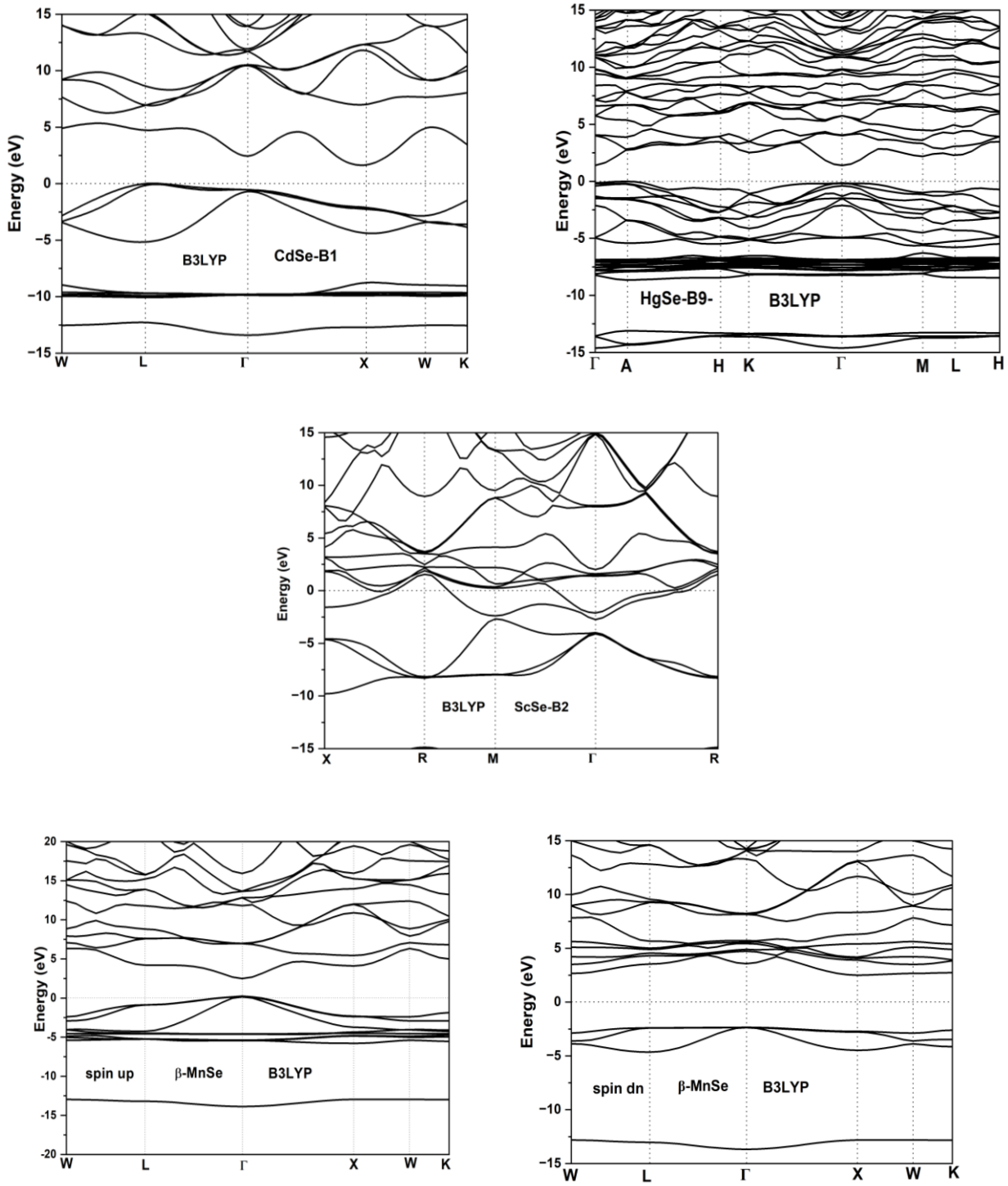

Figure III- 43: Band structure of the CdSe, HgSe, ScSe, and MnSe obtained by B3LYP.

Table III- 24: Fundamental gap energy of CdSe, HgSe, ScSe and MnSe obtained using hybrid functional B3LYP.

Compounds		This study (eV)	Other calculations	Experiments
CdSe		1.667		
HgSe		1.401		
ScSe		0		
MnSe	Spin up	2.510		
	Spin dn	4.840		

III-5.3.2 Density of states

Figure III-44 illustrates the total and partial density of states of CdSe, HgSe, ScSe and MnSe obtained by the hybrid functional B3LYP.

For CdSe, we observed three distinct peaks: the first is around -12.5 eV below the Fermi level, consisting entirely of Se-s orbitals, with the Cd-d orbitals band above at -10 eV. The third peak, near the Fermi level, involves Se-p orbitals with a small contribution from Cd-s orbitals. The conduction band mainly includes Cd-p orbitals, with a slight involvement of Cd-s orbitals. For HgSe, four regions are apparent in the cinnabar phase: the first at -13.5 eV below the Fermi level, containing only Se-s orbitals; a band of Hg-d orbitals above; a minimal contribution from Se-p orbitals around -7.5 eV; the third region includes Se-p and Hg-s orbitals at -6 eV; and the fourth contains Se-p orbitals near -5 eV, close to the Fermi level. The conduction band is primarily Hg-p orbitals, with minor Se-s contributions. In ScSe, the lowest bands, influenced by Se-p states, are around -10 eV, and the Se-p bands are near -5 eV, with small contributions from Sc-d and Sc-p orbitals. The metallic nature of ScSe mainly involves Sc-d states, with some input from Se-s and Sc-p orbitals at the Fermi level. In MnSe, the two lowest bands are p-d hybridized, while higher bands represent Se-s states. Below the Fermi level, the spin-down p bands shift upward, whereas the spin-up p bands above the Fermi level shift downward due to strong p-d interaction. Consequently, there are fewer occupied spin-down states and more occupied spin-up states, with the spin-up p bands dominating the region near the Fermi level.

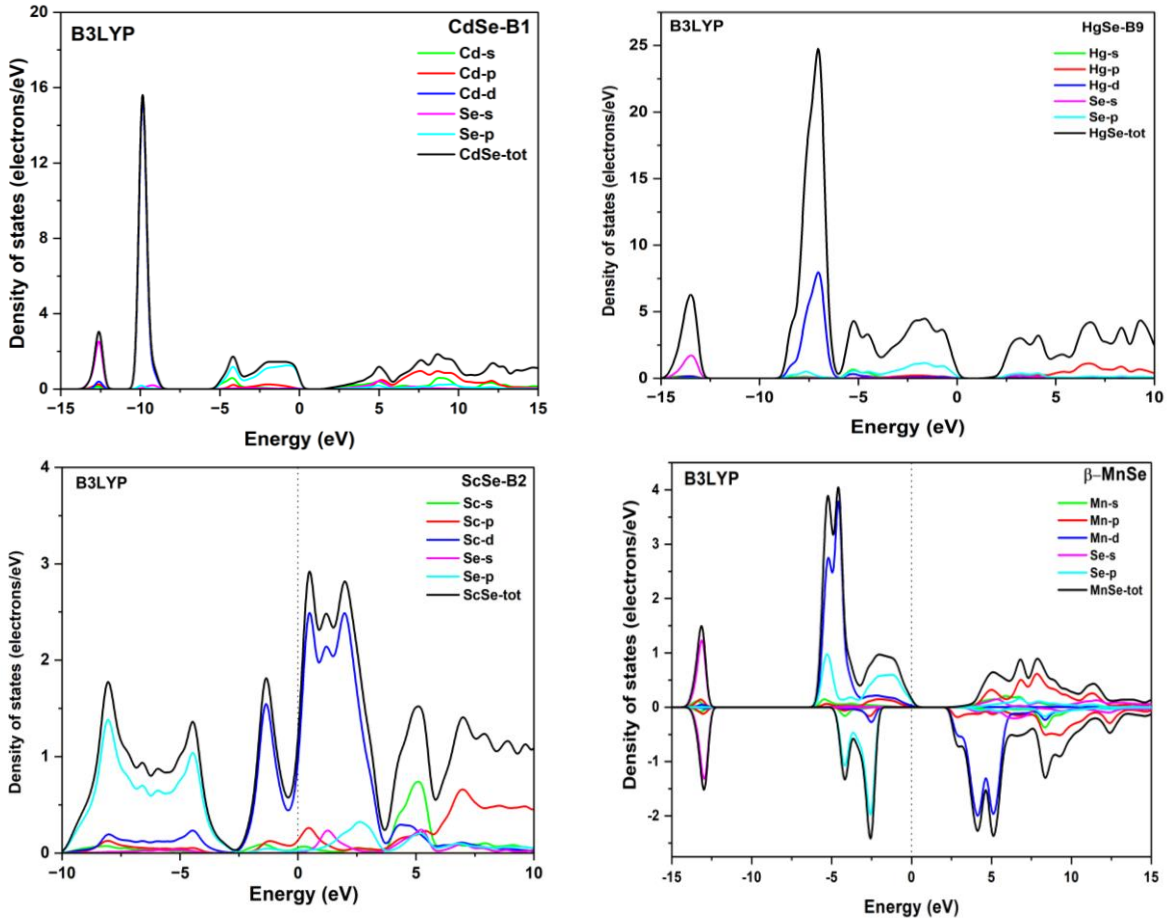

Figure III- 44: Total and partial density of states of CdSe, HgSe, ScSe and MnSe obtained by B3LYP.

III-5.4 Optical response

III-5.4.1 Dielectric function

Figure III-45 shows the calculated real Re (ω) and imaginary Im (ω) optical parts of the dielectric function of CdSe in the rock salt structure, HgSe in the cinnabar phase, ScSe in the CsCl type structure and MnSe in the zinc blende structure.

The real Re (ω) part ε of the dielectric function reaches an acute peak for low values for all compounds. Then, it is approached as a negative value in a region of medium energy. Continued by a low positive value in the region of high energies, however, the primary peak in each of the ε_0 curves are due to the interband transition of electrons from the valence band to the conduction band. In addition, we see a more intense central peak for CdSe, HgSe, and ScSe and MnSe. The central peak is more pronounced at around 4.223 eV, 2.876 eV, 1.825 eV and 2.432 eV for CdSe, HgSe, ScSe and MnSe, respectively. At higher energies, the real part of the dielectric function fall to zero at 5.648 eV, 5.036 eV, 5.720 eV, and 8.489 eV for CdSe, HgSe, ScSe, and MnSe, respectively. In this spectral region, the compounds primarily act as dispersive media, scattering the incident electromagnetic radiation. This metallic-like optical response

suggests that these materials could be useful for radiation shielding applications. Beyond the main peak, ε₀ exhibits an oscillatory structure around zero, eventually stabilising at approximately 18.412 eV for CdSe, 17.444 eV for HgSe, 18.501 eV for ScSe, and 23.027 eV for MnSe.

The imaginary Im (ω) part (ε_∞) of the dielectric function shows that ε_∞ approaches zero for CdSe, HgSe and MnSe, while for ScSe, it remains slightly non zero. The first critical point of the dielectric function occurs at energies of 0.629 eV, 0.138 eV, and 2.064 eV for CdSe, HgSe, and MnSe, respectively; these points indicate the threshold of optical transitions from the highest point in the valence band to the lowest point in the conduction band. This is known as the fundamental absorption threshold. Additionally, we observe a maximum primary peak, reflecting the highest absorption of these materials in the low-energy region. Consequently, the strong absorption in the infrared range and the upper limit of the visible spectrum make these materials promising candidates for optoelectronic device manufacturing, particularly in infrared detection and visible light optoelectronics. Table III-25 represents the values of static dielectric constant (ε_0) for CdSe, HgSe, ScSe and MnSe. Since no experimental data are available for comparison, our results provide reliable theoretical predictions that may serve as future reference values.

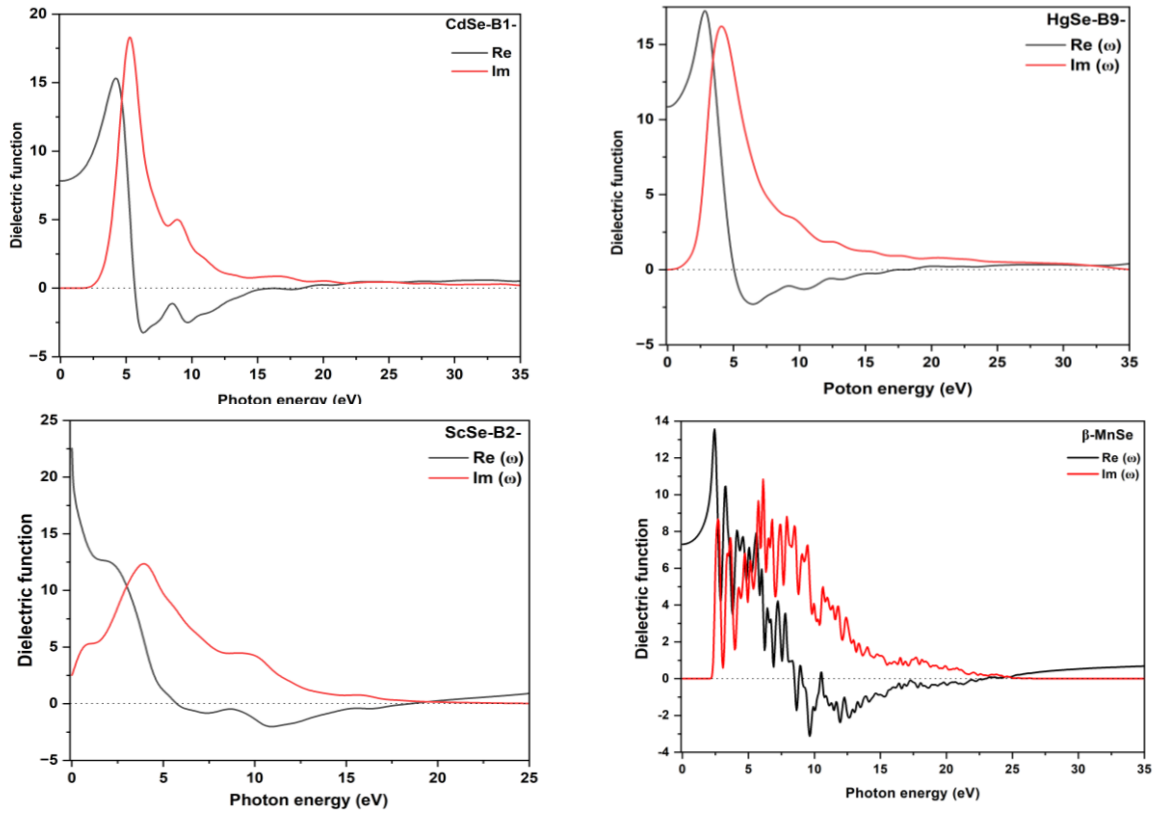

Figure III- 45: Real R $\boldsymbol{\varepsilon(\omega)}$ and imaginary Im $\boldsymbol{\varepsilon(\omega)}$ parts of the dielectric function of CdSe, HgSe, ScSe and MnSe as a function of photon energy

Table III- 25: Static dielectric constant (ε_0) of CdSe, HgSe, ScSe and MnSe.

Compounds	CdSe	HgSe	ScSe	MnSe
Static dielectric constant (ε_0)	7.823	10.850	22.539	7.306

III-5.4.2 Refractive index

Figure III-46 shows the calculated refractive index spectra, n (ω) and k (ω) for CdSe, HgSe, ScSe and MnSe.

The refractive index curves demonstrate a primary incident energy range of 0 to 35 eV for CdSe, HgSe, and MnSe, and 0 to 25 eV for ScSe. Distinct peaks are observed within these ranges, which arise near the resonance frequencies corresponding to the interband electronic transition from the valence band and conduction band. These features reflect the strong coupling between photon energy and electronic excitation in these compounds. The calculated static refractive index n (ω) is listed in Table III-26. Since no experimental or theoretical data are available for direct comparison, our results provide reliable predictions that may serve as useful references for future optical investigations.

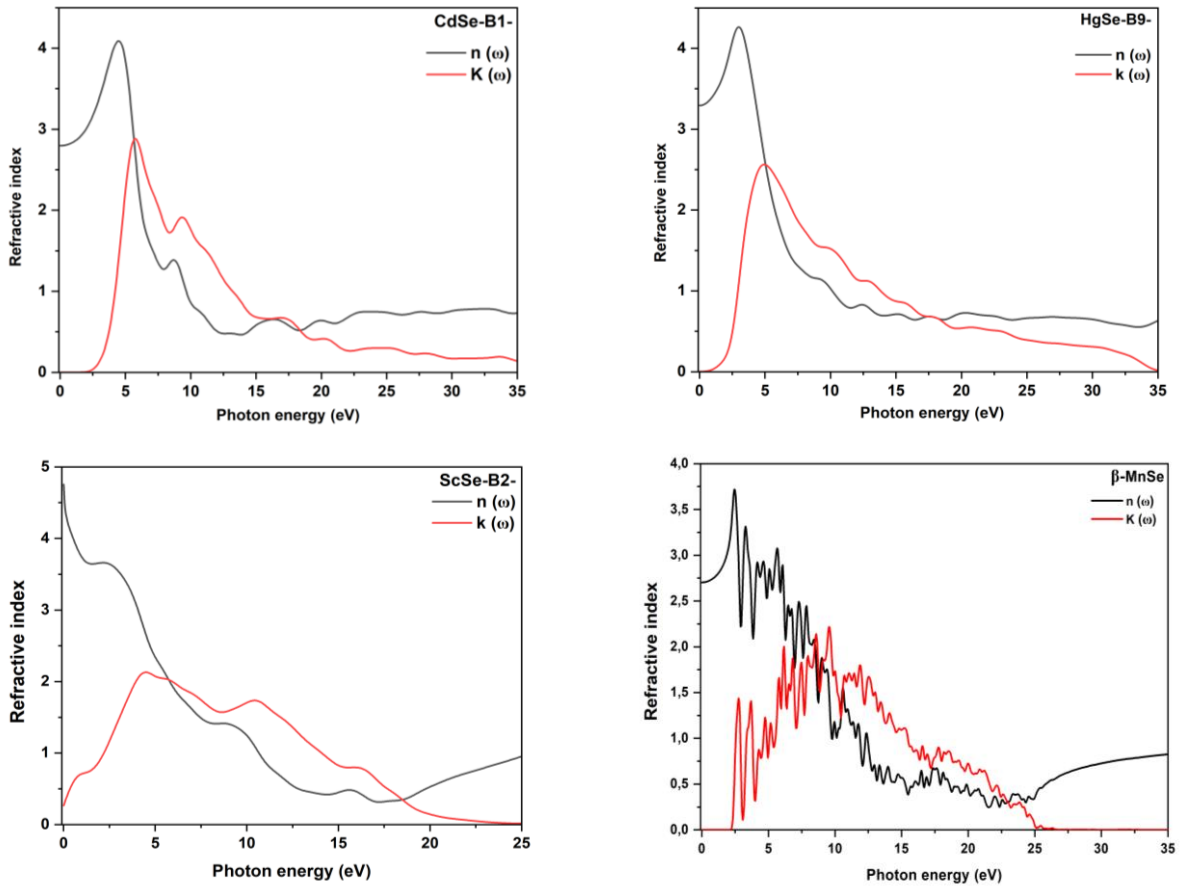

Figure III- 46: Real n(ω) and imaginary k(ω) parts of the refractive index of CdSe, HgSe, ScSe and MnSe as a function of photon energy.

Table III- 26: Static refractive index $\boldsymbol{n(0)}$ for CdSe, HgSe, ScSe and MnSe.

Compounds	CdSe	HgSe	ScSe	MnSe
Static refractive index $\boldsymbol{n(0)}$	2.797	3.293	4.754	2.703

III-5.4.3 Reflectivity

Figure III-47 illustrates the reflectivity spectrum of CdSe, HgSe, ScSe and MnSe as a function of photon energy, considering incident radiation polarized along the primary crystallographic directions. The spectra show clear variations in reflectivity across the studied photon energy ranges, indicating how the electronic structure responds to electromagnetic radiation. Peaks in the reflectivity curves correspond to strong interband electronic transitions, while the gradual decline at higher photon energies suggests increased transparency of the materials.

Table III-27 displays the reflectivity spectrum values for CdSe, HgSe, ScSe, and MnSe. Our results for these spectra lack comparable experimental data. They are predictable and may serve as references. Furthermore, the observed reflectivity behavior highlights the potential of these materials for technological applications, such as optical coatings for managing light reflection and transmission, radiation shielding within specific photon energy ranges, and optoelectronic devices, where customized reflectivity is essential for efficiency.

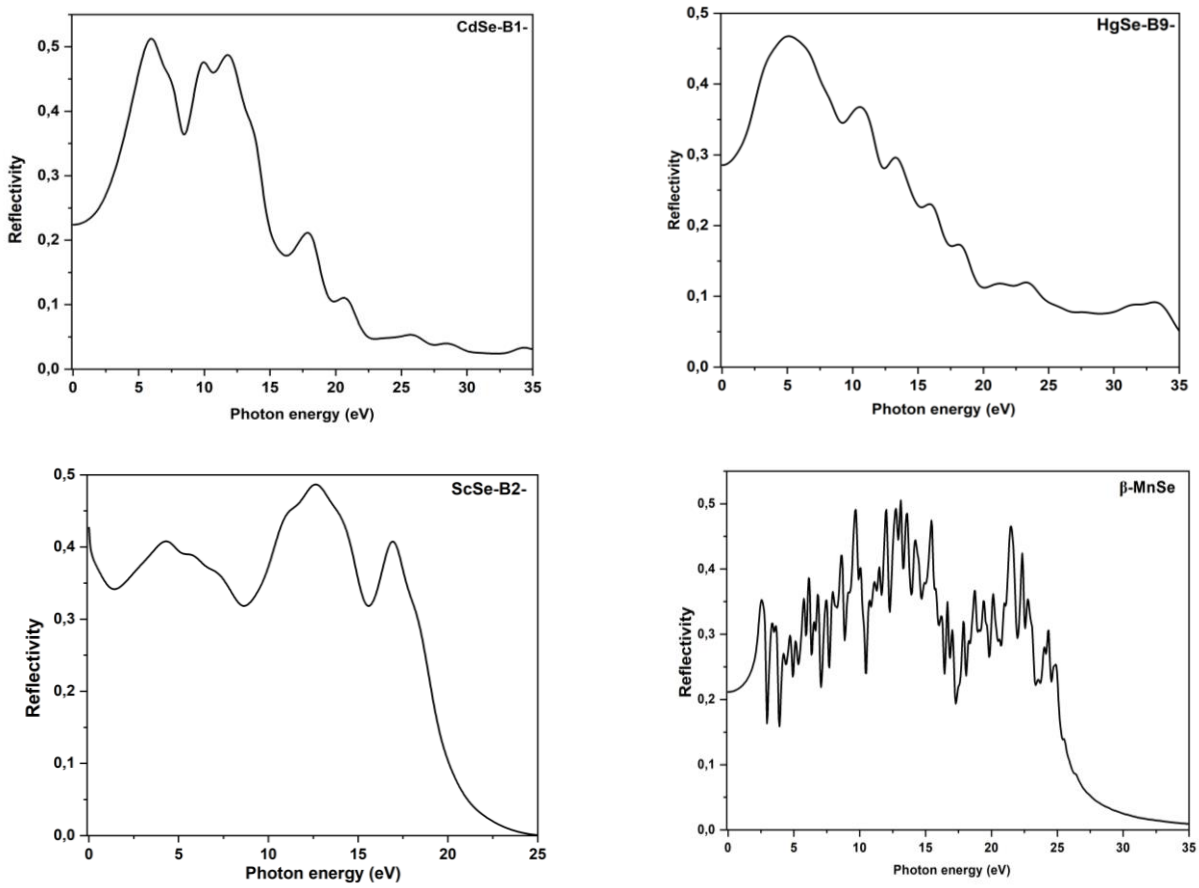

Figure III- 47: Reflectivity spectrum of CdSe, HgSe, ScSe and MnSe as a function of photon energy.

Table III- 27: Static reflectivity R(0) for CdSe, HgSe, ScSe and MnSe.

Compounds	CdSe	HgSe	ScSe	MnSe
Static reflectivity $\boldsymbol{R(0)}$	0.224	0.285	0.426	0.211

III-5.4.4 Absorption coefficient

Figure III-48 represents the optical absorption spectrum as a function of photon energy of CdSe, HgSe, ScSe and MnSe. From this figure, the optical absorption starts at about 1.99 eV, 0.994 eV and 2.011 eV for CdSe, HgSe and MnSe, respectively. Conversely, it starts at zero eV for ScSe, reflecting its metallic nature. Furthermore, the optical absorption coefficient rises with rising photon energy reaching maximum values at approximately 9.551 eV, 10.363 eV, 10.855 eV and 11.913 eV for CdSe, HgSe, ScSe and MnSe, respectively. After that, the absorption coefficient gradually decreases and eliminates at photon energies higher than 35 eV for CdSe, HgSe and MnSe, and 25 eV for ScSe. That results highlights that CdSe, HgSe and MnSe behave as semiconductors with well defined absorption edges, while ScSe shows metallic

absorption characteristics due to its zero gap nature. The energy ranges of strong absorption suggest their potential use in optoelectronic and photonic applications, particularly in devices operating across the visible to ultraviolet spectral regions

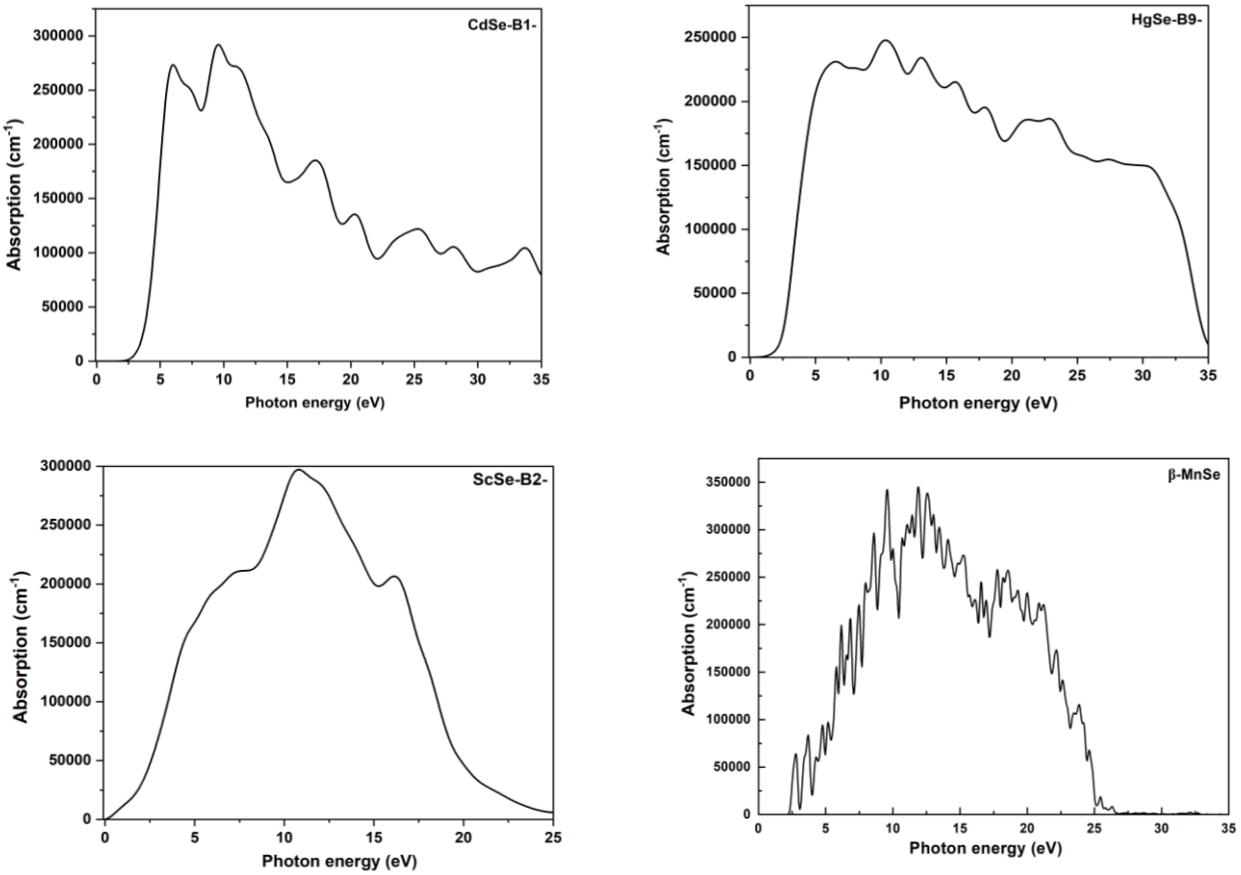

Figure III- 48: Optical absorption spectrum as a function of photon energy of CdSe, HgSe, ScSe and MnSe.

III-5.5 Elastic parameters and related mechanical properties

As we mentioned previously, only three distinct elastic constants, C_{11}, C_{12}, and C_{44}, are known to exist in cubic crystals. In contrast, the trigonal (rhombohedral)) crystal has six elastic constants: C_{11}, C_{12}, C_{44}, C_{33}, C_{13}, and C_{14}.

Tables III-28, III-29, III-30, and III-31 represent the calculated elastic constants, Shear modulus (G), Young's modulus (E), Poisson's ratio (**ν**), Cauchy pressure (C″) and Pugh's ratio (K) calculations for CdSe, HgSe, ScSe and MnSe, respectively.

The elastic constant results for CdSe, HgSe, ScSe and MnSe do not have comparable experimental findings. However, for CdSe, our calculated values are closely aligned with those reported in reference [94]. Howrver, for HgSe, because to the absence of experimental data, comparison is carried out with previous theoretical results [22]. Furthermore, for ScSe, our

computed values are comparable with theoretical results reported in [76], which demonstrate considerable variances, perhaps due to discrepancies in computational methodologies or structural models. Moreover, for MnSe, no comparable experimental findings are available. Furthermore, our results can serve as reliable reference data.

The calculated Young's modulus (E) and Shear modulus (G) also lack experimental data for all compounds. Moreover, our computed values agree reasonably well with theoretical studies, such as [22] for HgSe and [76]for ScSe, although some discrepancies exist, again likely due to differences in computational methods.

The ductility or brittleness of these materials can be elucidated using certain established criteria. Firstly, the calculated Poisson's ratio for all compounds are found to be above the critical threshold of 0.26, indicating a ductile character, This values show excellent accord with previously reported theoretical results [22] for HgSe and [76] for ScSe, though no experimental data are available for comparison. Moreover, the Pugh's ratio (B/G) was found to be 1.928 for CdSe, 2.603 for HgSe, 3.582 for ScSe and 4.290 for MnSe, since this value are well above the critical value 1.75, all compounds are clearly classified as ductile . The Cauchy pressure C″ also provides a reliable ductility criterion: a negative value indicates brittleness, while a positive value suggests ductility. For cubic crystal C″ is calculated using equation III − 9, whereas for trigonal crystals, the difference, C" = (C_{13}-C_{44}) is referred to as the Cauchy pressure [95], the conclusions of the Pettifor criterion and Poisson's ratio and Pugh report consistently confirm the ductile nature of these compounds. Finally, in all cases, the bulk modulus (B) is greater than the shear modulus (G). The elevated value of B indicates that shearing strain controls the mechanical stability of CdSe, HgSe, ScSe, and MnSe.

Understanding these elastic constants is essential for verifying the mechanical stability of materials. For stability to be maintained, the set of elastic constants C_{ij} must satisfy the the Born stability criteria, and that all C_{ij} must be positive. In the case of a cubic structure, the Born stability criteria conditions are given are detailed in equation III−11. For a trigonal (rhombohedral) crystal, the corresponding stability conditions are expressed by the relation provided in references [95].

$$C_{11} - |C_{12}| > 0\ ,\ C_{44} = 0, (C_{11} + C_{12})C_{33} > 2C_{13}^2\ , (C_{11} - C_{12})C_{44} > C_{14}^2 \qquad \text{III} - 16$$

By substituting the calculated elastic constants into the corresponding stability formulas, we confirm that the current results meet the Born stability criteria. This indicates that CdSe, HgSe, ScSe and MnSe are mechanically stable under the studied conditions.

Table III- 28: The calculated elastic constants (C_{ij}), shear modulus (G), Young's modulus (E), Poisson's ratio (ν), Pugh ratio (K), and Cauchy pressure (C″) of CdSe.

Compound	C_{ij} (GPa)	This study	Other calculation	Experiments
CdSe	C_{11}	128.177	133.0857 [94] 79.7 [96]	
	C_{12}	39.774	44.7621 [94] 46.7 [96]	
	C_{44}	29.774	28.9676 [94] 46.5 [96]	
	G (GPa)	35.012		
	E	89.886		
	ν	0.283		
	C_{12}-C_{44}	10		
	B/G	1.928		

Table III- 29: The calculated elastic constants (C_{ij}), shear modulus (G), Young's modulus (E), Poisson's ratio (ν), Pugh ratio (K), and Cauchy pressure (C″) of HgSe.

Compound	C_{ij} (GPa)	This study	Other calculation	Experiments
HgSe	C_{11}	72.848	15.29 [22]	
	C_{12}	30.747	2.03 [22]	
	C_{44}	22.765	10.81 [22]	
	C_{13}	44.404	4.96 [22]	
	C_{14}	8.740	5.11 [22]	
	C_{33}	85.249	28.75 [22]	
	G (GPa)	19.460	7.22 [22]	
	E	51.256	16.96 [22]	
	ν	0.317	0.175 [22]	
	C_{13}-C_{44}	21.639		
	B/G	2.603		

Table III- 30: The calculated elastic constants (C_{ij}), shear modulus (G), Young's modulus (E), Poisson's ratio (ν), Pugh ratio (K), and Cauchy pressure (C″) of ScSe.

Compound	C_{ij} (GPa)	This study	Other calculation	Experiments
ScSe	C_{11}	244.023	187.899 [22]	
	C_{12}	21.621	33.406 [22]	
	C_{44}	4.030	17.819 [22]	
	G (GPa)	26.728	33.664 [22]	
	E	73.359	89.202 [22]	
	ν	0.372	0.324 [22]	
	C_{12}-C_{44}	17.591		
	B/G	3.582k		

Table III- 31: The calculated elastic constants (C_{ij}), shear modulus (G), Young's modulus (E), Poisson's ratio (ν), Pugh ratio (K), and Cauchy pressure (C″) of MnSe.

Compound	C_{ij} (GPa)	This study	Other calculation	Experiments
MnSe	C_{11}	65.828		
	C_{12}	49.408		
	C_{44}	17.224		
	G (GPa)	12.793		
	E	35.613		
	ν	0.398		
	C_{12}-C_{44}	32.184		
	B/G	4.290		

III-5.6 Lattice dynamics

The phonon dispersion scheme calculated along many high-symmetry directions in the Brillouin zone (BZ) for CdSe , HgSe and ScSe with optimized lattice parameters is displayed in Figures III-49.

In cubic crystals containing two atoms per primitive cell. The phonon spectrum consists of three acoustic branches and three optical branches. For CdSe, the dispersion curve show no

negative frequency at any point in the Brillouin zone and confirming that CdSe are dynamically stable. In contrast, the dispersion curve of ScSe displays negative frequencies, suggesting that ScSe is dynamically unstable, consistent with previously reported results [37]. For CdSe, the three acoustic branches originate from the Γ point and evolve smoothly along the high-symmetry paths. The optical branches are relatively flat and extend up to ~175 cm^{-1}. Particularly, the TO and LO phonon modes at the Γ-point are found at 103.637 cm^{-1} and 175.656 cm^{-1}, respectively

The cinnabar (B9) phase of HgSe, investigated here for the first time from a phonon perspective, exhibits a rich and more complex vibrational behavior arising from its non-centrosymmetric trigonal structure (space group $P3_121$) and larger primitive cell containing six atoms. The calculated phonon dispersion curves exhibit 18 phonon branches, consisting of three acoustic modes and 15 optical modes. The absence of imaginary frequencies confirms the dynamical stability of the B9 phase. The dispersion relations display characteristic features such as mode splitting, crossings and anisotropic dispersion along different crystallographic directions (e.g., Γ–A, Γ–K), reflecting the reduced symmetry and chiral nature of the structure. The low-frequency acoustic modes, primarily located below 50 cm^{-1}, are attributed mainly to Hg displacements, while higher optical modes involve increasing contributions from Se atoms, especially in the 180–240 cm^{-1} range.

Table III-32 represents the values of phonon frequencies at the high symmetry point (Γ) for CdSe and HgSe. The phonon frequencies at the high symmetry point for CdSe and HgSe do not have comparable experimental findings. Our results are predictable and can serve as a reference.

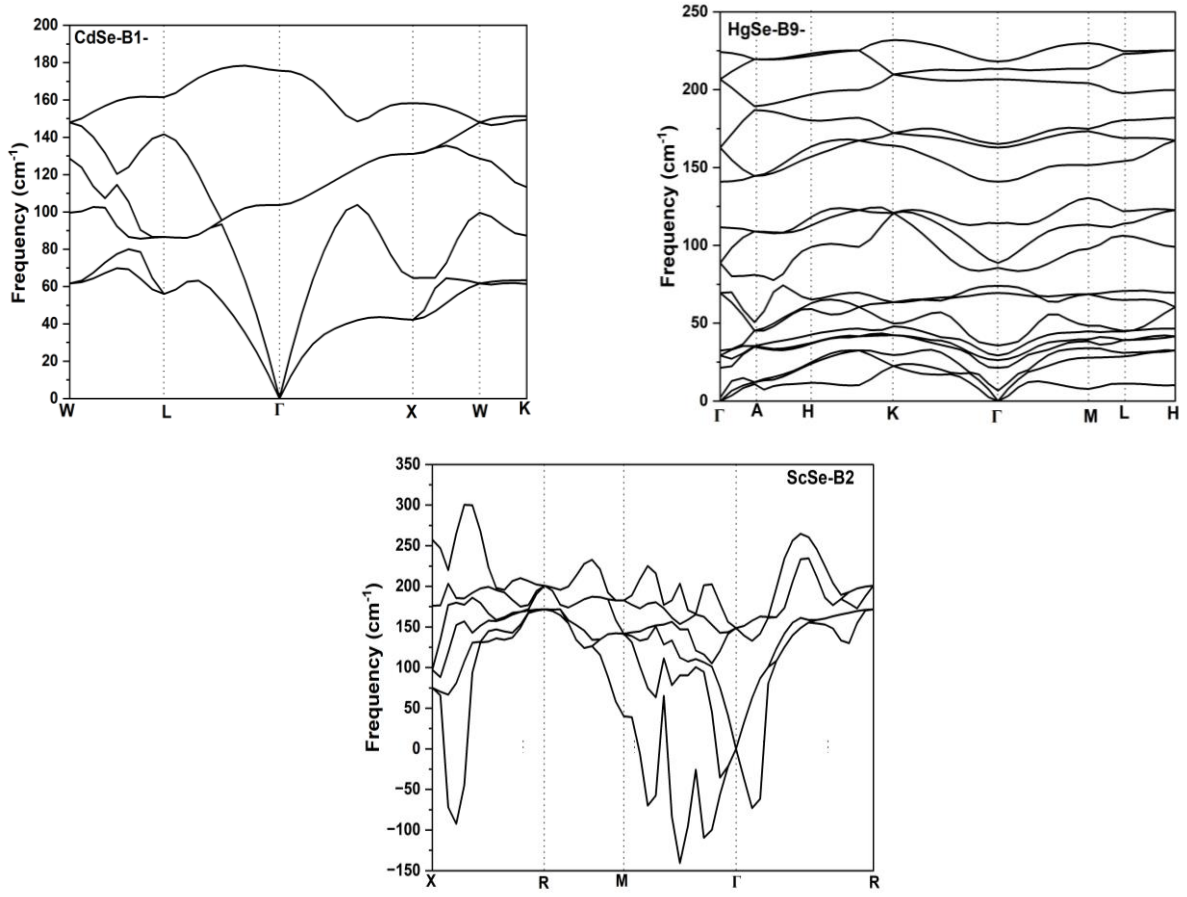

Figure III- 49: phonon dispersion curves of CdSe, HgSe and ScSe.

Table III- 32: Phonon frequencies at high-symmetry points for CdSe and HgSe.

Phonon frequencies (cm^{-1})	CdSe	HgSe
ω_{Lo}	175.656	218.115
ω_{TO}	103.637	213.319

III-5.7 Thermodynamic properties

III-5.7.1 Bulk modulus (B)

Figure III-50 shows the variation of the bulk modulus (B) as a function of temperature of CdSe, HgSe, ScSe and MnSe.

Increasing temperature generally tends to expand the material, increasing interatomic distances. This reduces the interatomic bonding forces, thus decreasing the stiffness of the material. Consequently, B decreases with increasing temperature for all compounds. Table III-33 presents B values of CdSe, HgSe, ScSe and MnSe at 300 K. at ambient temperature, B is calculated to be 68.191 GPa for CdSe, 57.032 GPa for HgSe, 54.1864 GPa for MnSe and 91.894

for ScSe. This value decreases slightly to 55.494 GPa, 65.308 GPa, 87.366 GPa and 45.704 GPa at 300K for CdSe, HgSe, ScSe and MnSe at 300K, respectively. There are no experimental or theoretical results available for comparison of B, our results are predictable and may serve as references.

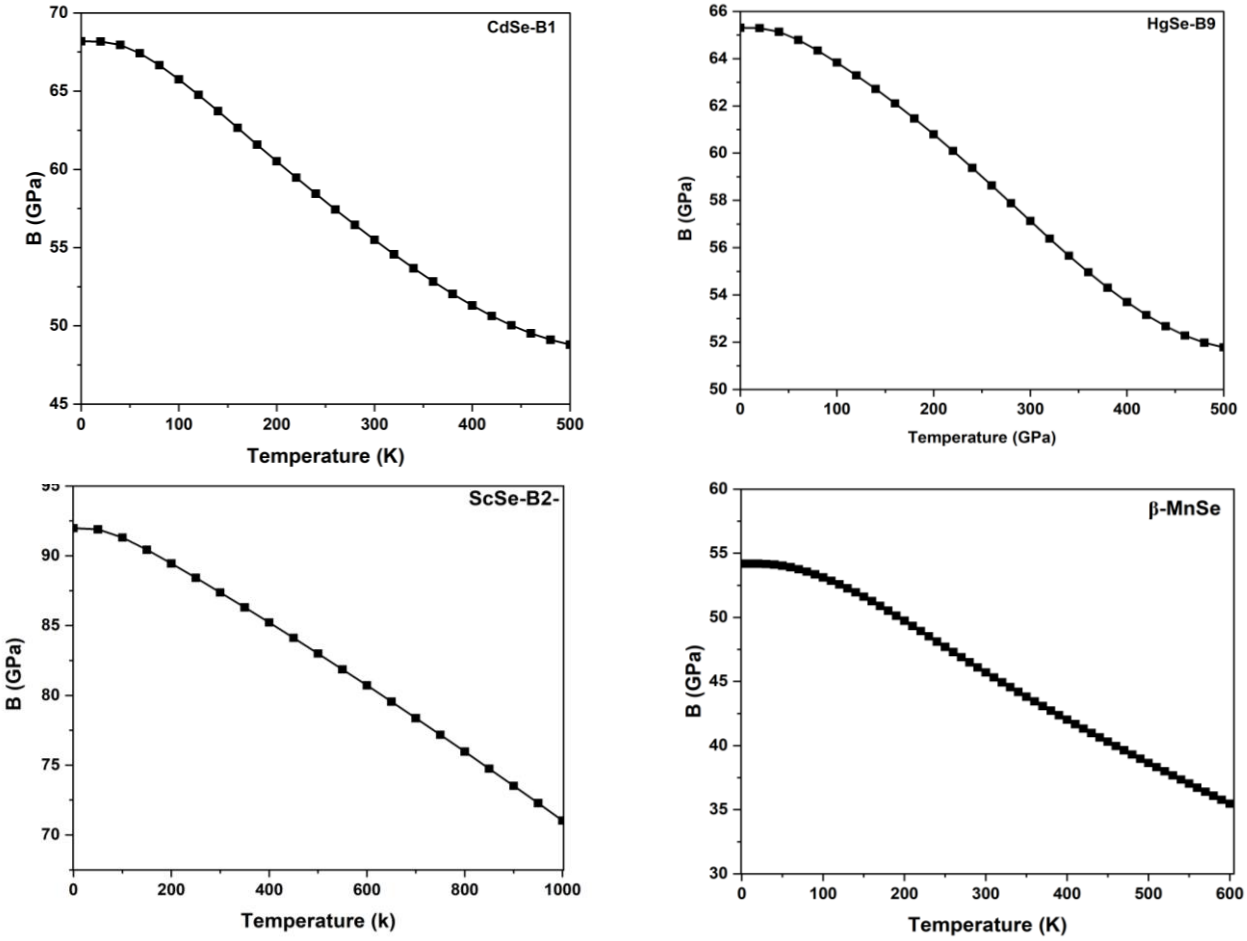

Figure III- 50: The variation of the bulk modulus (B) of CdSe, HgSe, ScSe and MnSe as a function of temperature.

Table III- 33: Bulk modulus (B) values of CdSe, HgSe, ScSe and MnSe at 300K.

Compounds	CdSe	HgSe	ScSe	MnSe
B (GPa)	55.494	65.308	87.366	45.704

III-5.7.2 Coefficient of thermal expansion

Figure III-51 shows the variation of the thermal expansion coefficient (α) as a function of temperature of CdSe, HgSe, ScSe and MnSe. In all case, α show a monotonic increasing trend with rising temperature, reaching higher values at elevated temperatures. This observation suggests that the four compounds maintain structural stability across the considered

temperatures range. Table III-34 lists calculated values of α of CdSe, HgSe, ScSe and MnSe at 300 K. At ambient pressures (0 GPa), α is calculated to be (in unit 10^{-5} K^{-1}) 6.601, 5.886, 4.623 and 3.373 for CdSe, HgSe, ScSe and MnSe, respectively.

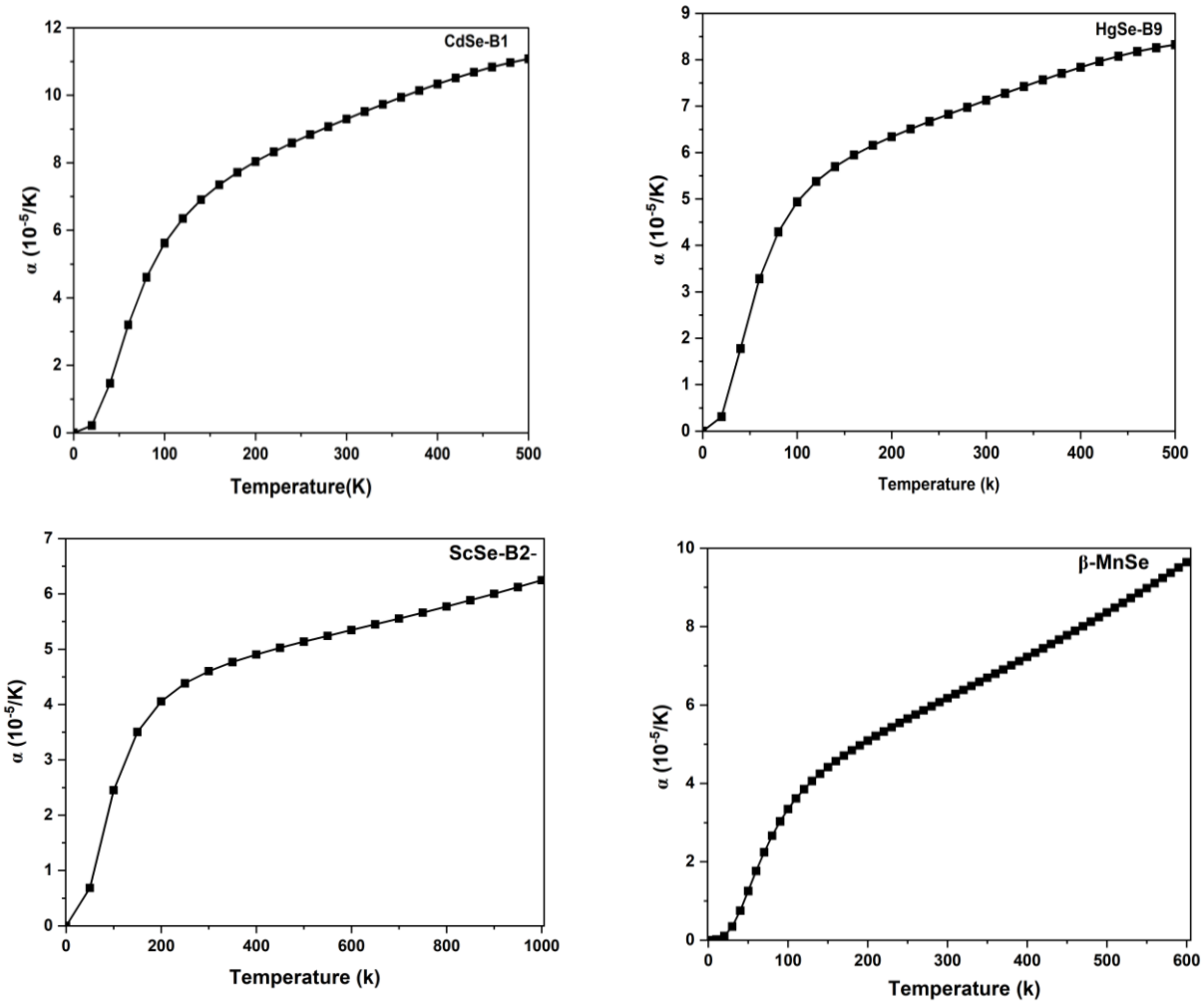

Figure III- 51: Variation of the thermal expansion (α) of CdSe, HgSe, ScSe and MnSe as a function of temperature.

Table III- 34: Thermal expansion (α) values of CdSe, HgSe, ScSe and MnSe at 300 K.

Compounds	CdSe	HgSe	ScSe	MnSe
α (10^{-5}/k)	9.297	7.127	4.568	6.174

III-5.7.3 Specific heat capacity C_V

Figures III-52 illustrate the variation of the heat capacity at constant volume (C_V) as a function of temperature for CdSe, HgSe, ScSe, and MnSe. C_V exhibits similar behavior in response to temperature changes for CdSe, HgSe, ScSe, and MnSe. The heat capacity C_V of the studied systems reveals two distinct behaviors, depending on T across the considered range. At low temperatures, C_V rises rapidly with T, validating the experimental law in T^3 for these

conditions. Conversely, at high temperatures, it gradually increases and approaches the Dulong-Petit limit C_V=3nR. The calculated high temperature values converge to 49.774, 49.725, 149.576, and 49.629 (in units of J.mol^{-1}K^{-1}) for CdSe, HgSe, ScSe, and MnSe, respectively.

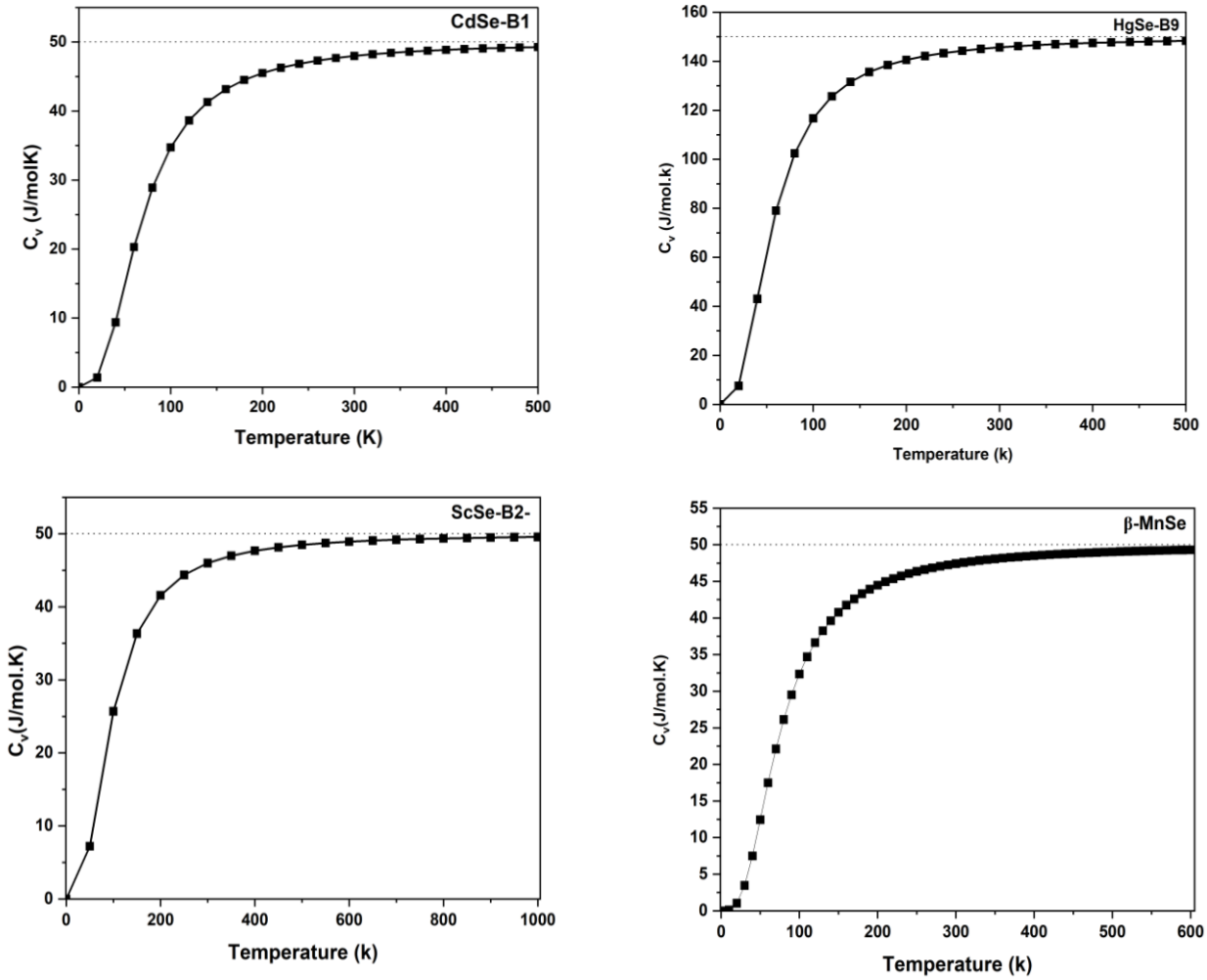

Figure III- 52: Variation of the heat capacity at constant volume C_V of CdSe, HgSe, ScSe, and MnSe as a function of temperature.

Table III- 35: Heat capacity at constant volume C_V of CdSe, HgSe, ScSe and MnSe at 300K.

Compounds	CdSe	HgSe	ScSe	MnSe
C_V (J/mol.K)	47.061	145.633	45.638	47.421

II-6 Influence of pressure on properties

III-6.1 Influence of pressure on structural properties

Figure III-53 illustrates the variation of the lattice parameter (a_0) of CdSe in the rock salt structure, HgSe in the cinnabar phase, ScSe in the Cscl type structure, and MnSe in the zinc-blende structure as a function of pressure. In all compounds, the lattice constant gradually decreases with rising pressure, aligning with the expected compressive behavior of crystalline solids under hydrostatic pressure. This steady reduction signifies the contraction of the crystal lattice as atoms are pushed closer together, thereby increasing the material's stiffness.

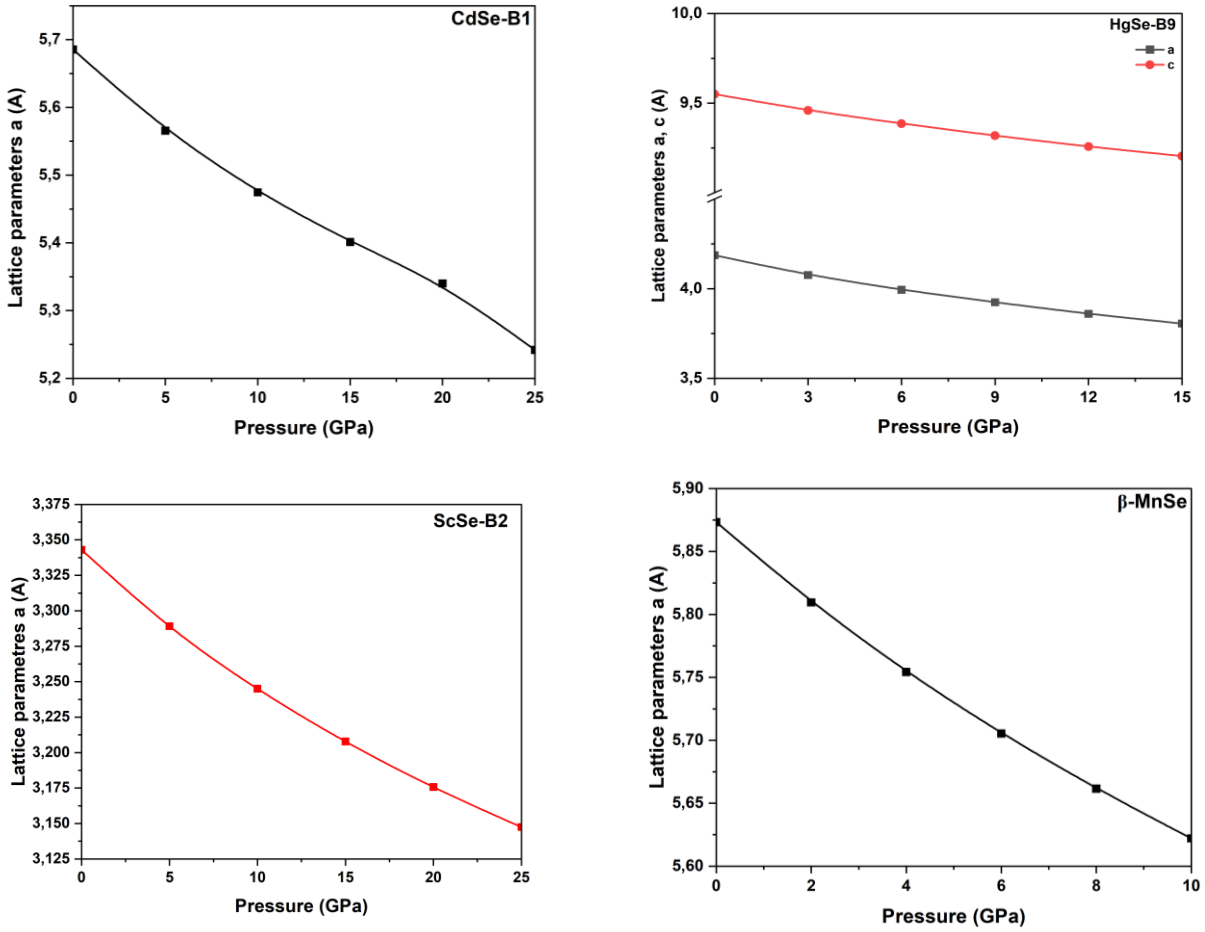

Figure III- 53: Variation of the unit cell parameter (a) as a function of pressure for CdSe, HgSe, ScSe and MnSe.

III-6.2 Influence of pressure on electronic properties

The band structures of CdSe, HgSe, ScSe and MnSe obtained by hybrid functional B3LYP exhibit similar overall features at zero and under pressure, with only minor variations. CdSe exhibits an indirect band gap (L-X), and the width of the band gap increases.

Furthermore, HgSe has a direct band gap (Γ-Γ); however, pressure does not alter the metallic nature of ScSe. Additionally, the spin-up channel of MnSe retains a direct band gap, while the spin-down channel exhibits an indirect band gap. Figure III-54 illustrates the variation of the band gap as a function of pressure for CdSe, HgSe, and MnSe. For both CdSe and HgSe, the band gap values exhibit a linear increase with rising pressure; in the case of MnSe, the spin-up channel band gap also increases linearly, though at a slower rate, whereas the spin-down channel band gap decreases slowly and linearly with increasing pressure. These results indicate that the electronic properties of these compounds can be effectively tuned by external pressure, highlighting their potential for use in pressure dependent optoelectronic and spintronic applications.

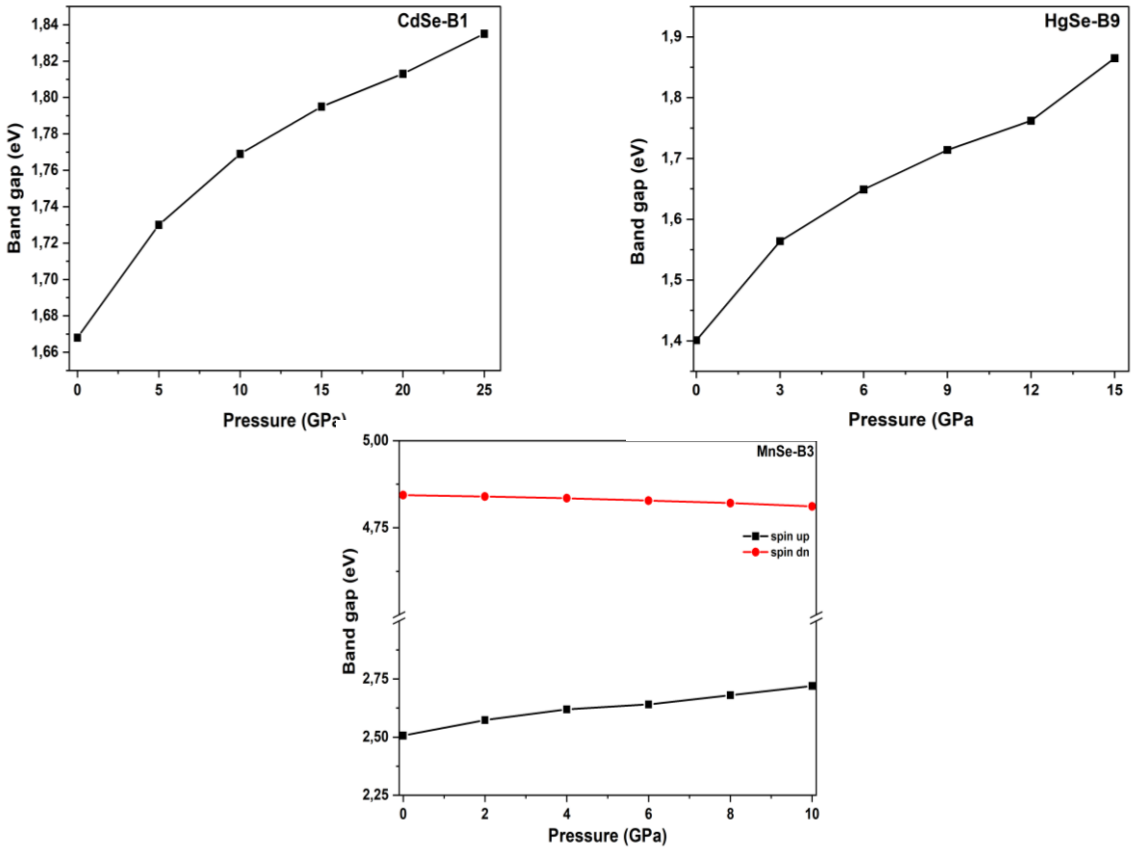

Figure III- 54: Variation of band gap energy of CdSe, HgSe and MnSe as a function of pressure.

III-6.3 Influence of pressure on optical properties

III-6.3.1 Dielectric function

Figures III-55, III-56, III-57, III-58 illustrates the real R ε(ω) and imaginary Im ε(ω) parts of the dielectric function at different pressure as a function of photon energy of CdSe, HgSe, ScSe and MnSe, respectively. The real R ε(ω) and imaginary Im ε(ω) components of the dielectric function display nearly identical qualitative behavior, with a few minor variations,

as seen by looking at these figures. For the R ε(ω) part of the dielectric function reaches a maximum close to the absorption limit for minor frequencies. Here are regions of reduced intensity that follow this maximum. Regarding the Im ε(ω) part, these peaks are displaced to lower frequencies in the low-frequency region and higher frequencies in the high-frequency region. The overall shape of both parts resembles that of a harmonic oscillator, confirming the expected optical response for CdSe, ScSe, HgSe, and MnSe under hydrostatic pressure. This behavior indicates that pressure modifies interband transition energies without altering the fundamental dielectric response of these compounds.

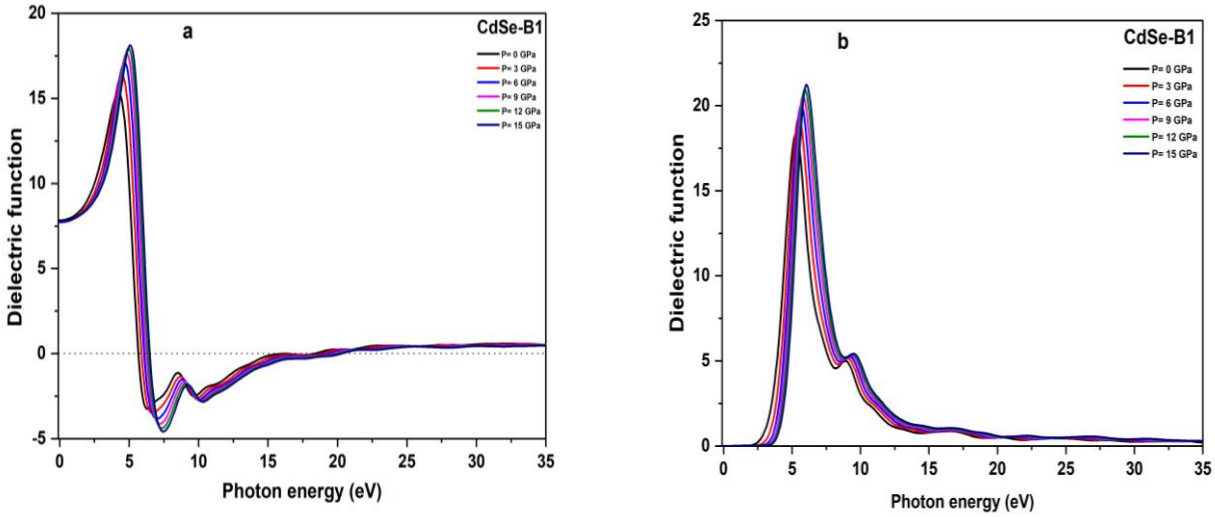

Figure III- 55: a) Real R $\boldsymbol{\varepsilon(\omega)}$ and b) imaginary Im $\boldsymbol{\varepsilon(\omega)}$ parts of the dielectric function at different pressures of CdSe as a function of photon energy.

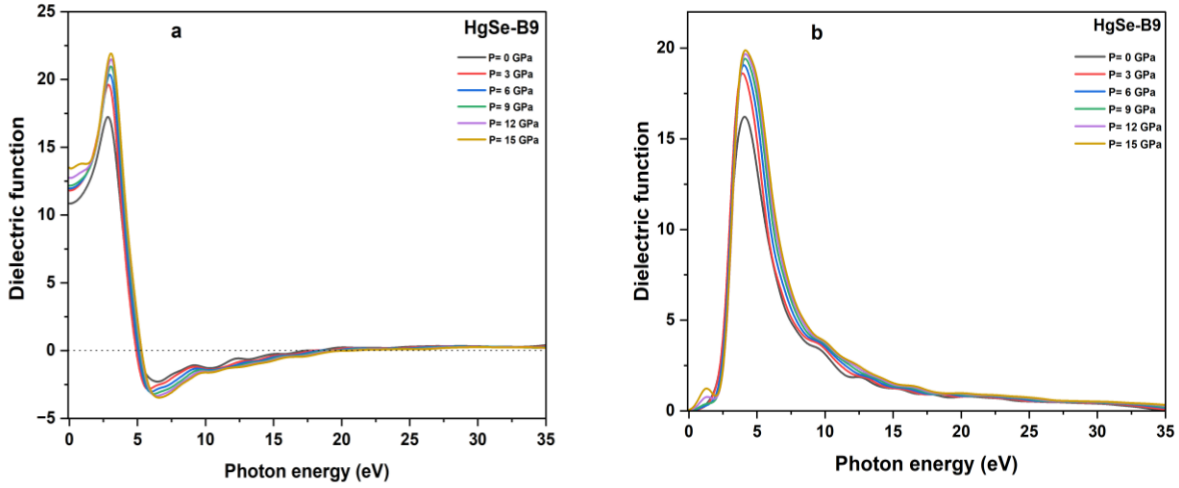

Figure III- 56: a) Real R $\boldsymbol{\varepsilon(\omega)}$ and b) imaginary Im $\boldsymbol{\varepsilon(\omega)}$ parts of the dielectric function at different pressures of HgSe as a function of photon energy.

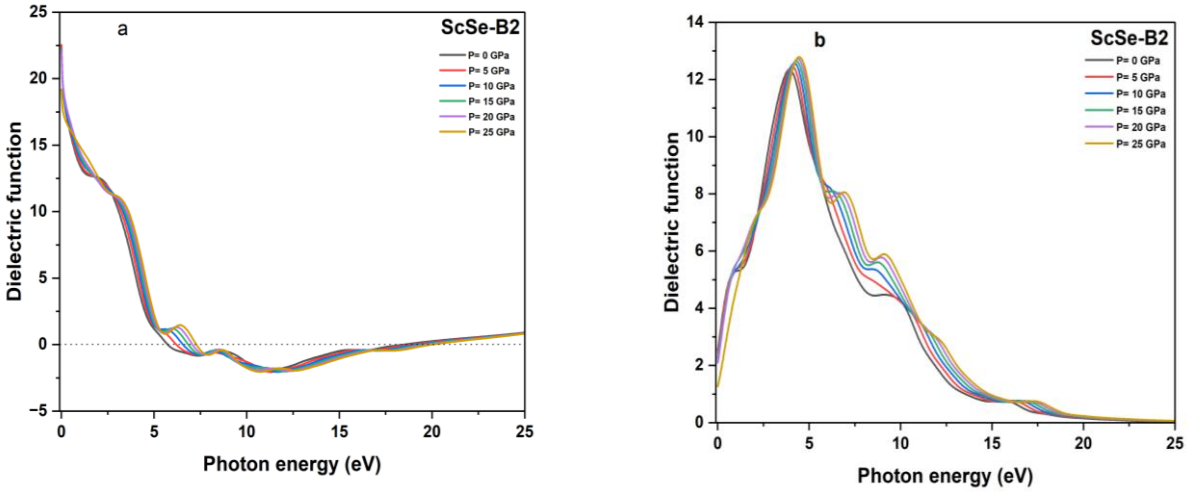

Figure III- 57: a) Real R $\boldsymbol{\varepsilon(\omega)}$ and b) imaginary Im $\boldsymbol{\varepsilon(\omega)}$ parts of the dielectric function at different pressures of ScSe as a function of photon energy.

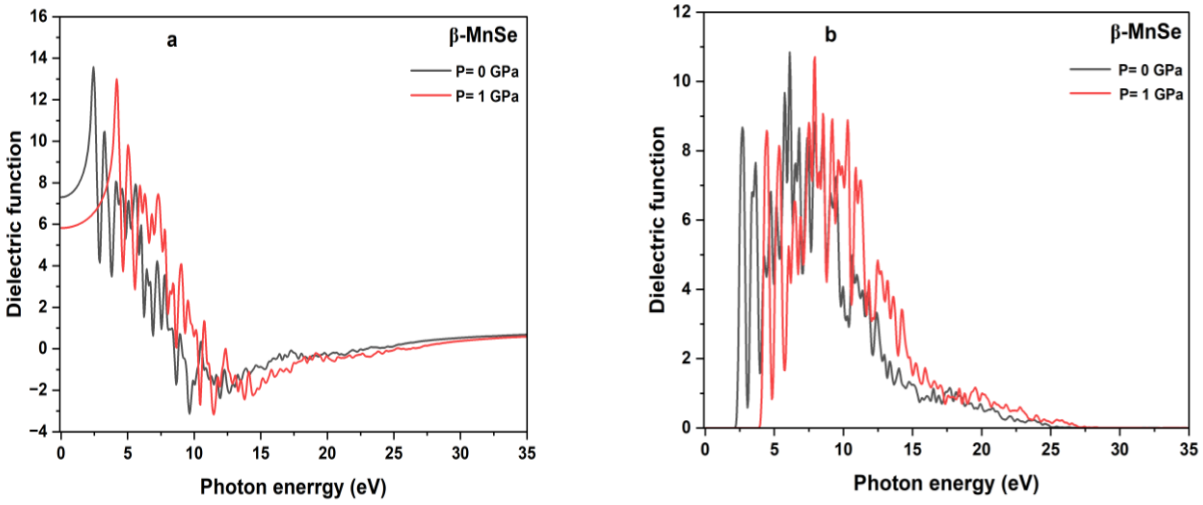

Figure III- 58: a) Real R $\boldsymbol{\varepsilon(\omega)}$ and b) imaginary Im $\boldsymbol{\varepsilon(\omega)}$ parts of the dielectric function at different pressures of MnSe as a function of photon energy.

III.6.3.2 Refractive index

Figures III-59, III-60, III-61 and III-62 illustrate the refractive index spectra n (ω) and k (ω) at different pressures as a function of photon energy for CdSe, HgSe, ScSe, and MnSe, respectively. At zero pressure (0 GPa), distinct peaks are clearly observed in both the n (ω) and k (ω) of the refractive index. When hydrostatic pressure is applied, these peaks exhibit noticeable shifts: they move upward in the low frequency region while shifting downward in the high frequency region. This behavior reflects pressure induced modifications in the electronic band structure, particularly in the interband transition energies that strongly influence optical dispersion. The primary impact of pressure is observed in the static refractive index values, the refractive indices of CdSe, HgSe, ScSe and MnSe exhibit a slight but systematic

increase with pressure. This trend is consistent with the pressure-induced decrease in lattice constants, which improves orbital overlap and modifies the dielectric response, this increasing the refractive index at low photon energy. The n (ω) and k (ω) components of the refractive index exhibit nearly identical qualitative behavior under different pressure, with only minor variation between the compounds. This indicates that while pressure alter the magnitude and position of spectral features, it does not fundamentally change the overall optical response mechanism.

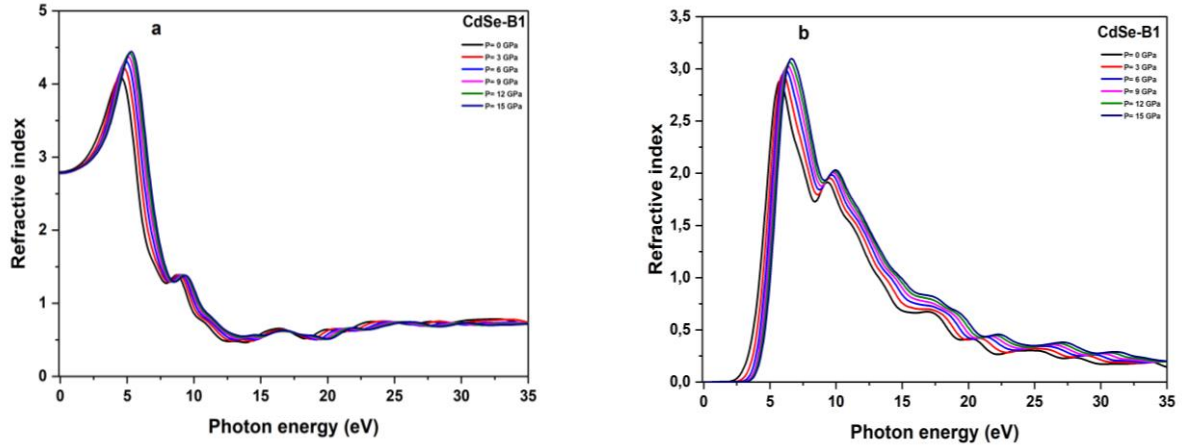

Figure III- 59: a) Real n(***ω***) and b) imaginary k(***ω***) parts of the refractive index at different pressures of CdSe as a function of photon energy.

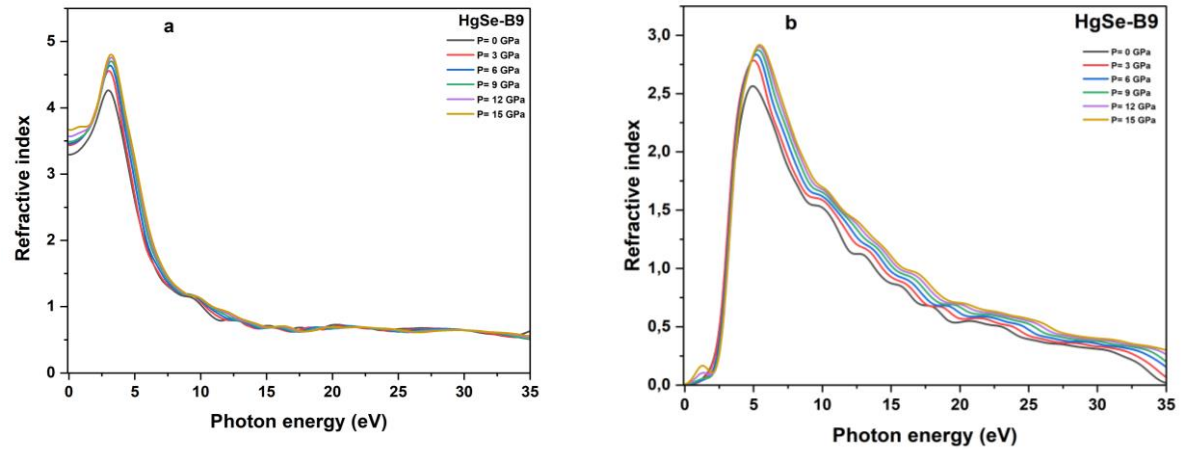

Figure III- 60: a) Real n(***ω***) and b) imaginary k(***ω***) parts of the refractive index at different pressures of HgSe as a function of photon energy.

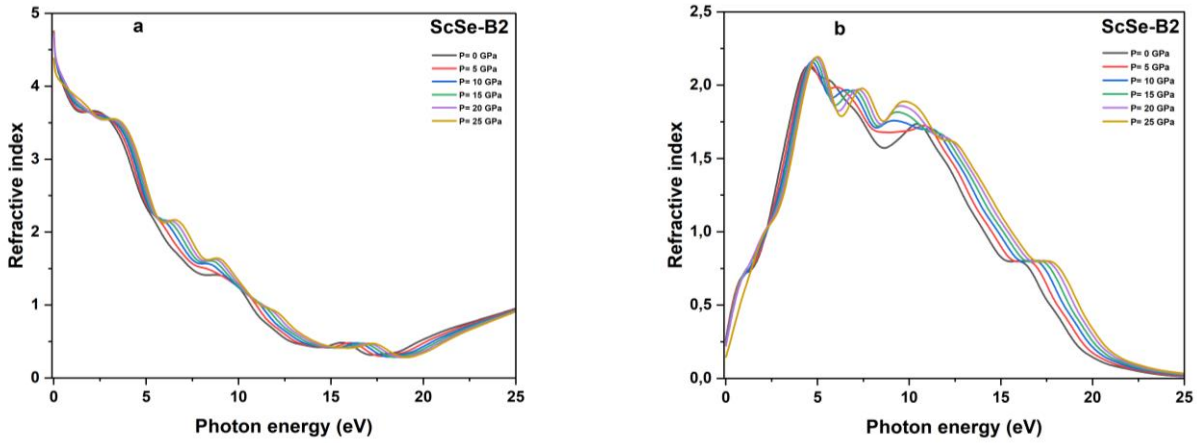

Figure III- 61: a) Real n(***ω***) and b) imaginary k(***ω***) parts of the refractive index at different pressures of ScSe as a function of photon energy.

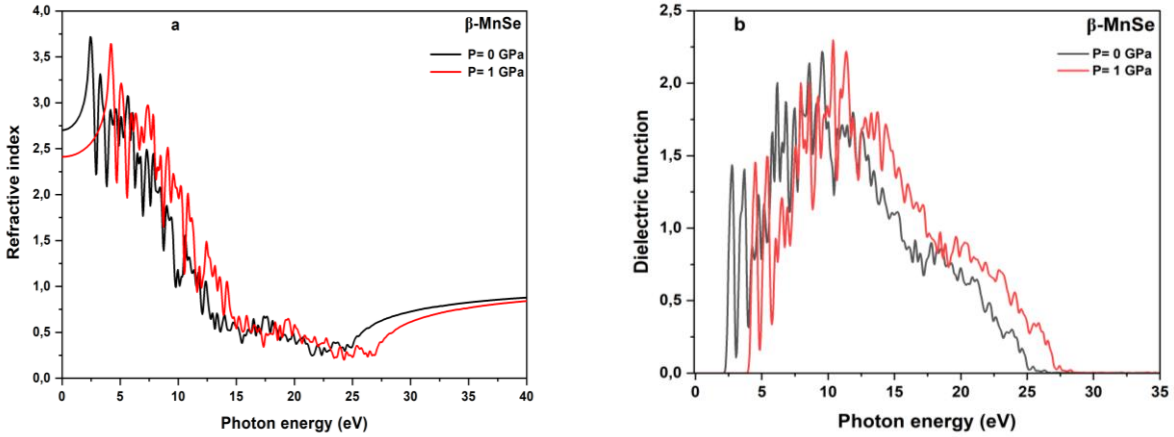

Figure III- 62: a) Real n(***ω***) and b) imaginary k(***ω***) parts of the refractive index at different pressures of MnSe as a function of photon energy.

III-6.3.3 Reflectivity

Figure III-63 illustrates the reflectivity spectra at different pressures as a function of photon energy of CdSe, HgSe, ScSe, and MnSe. In all four compounds, the overall reflectivity trends remain similar under compression, indicating that pressure does not fundamentally alter their optical response mechanisms. However, slight differences are noticeable in the peak positions and intensities. The most prominent effect is the upward shift of peaks in the low energy region with increasing pressure. This shift is directly linked to the blue shift of interband transitions, caused by the pressure induced reduction in lattice parameters and enhanced orbital overlap.

At higher photon energies, the reflectivity curves exhibit less susceptibility to pressure, suggesting that the deep electronic transitions are less impacted by lattice compression

compared to low energy transitions near the band boundaries. The observed result implies that the optical reflectivity of these compounds can be regulated by external pressure, which could be beneficial in photonic coatings, pressure sensors, or optical systems where controlled reflectance is needed.

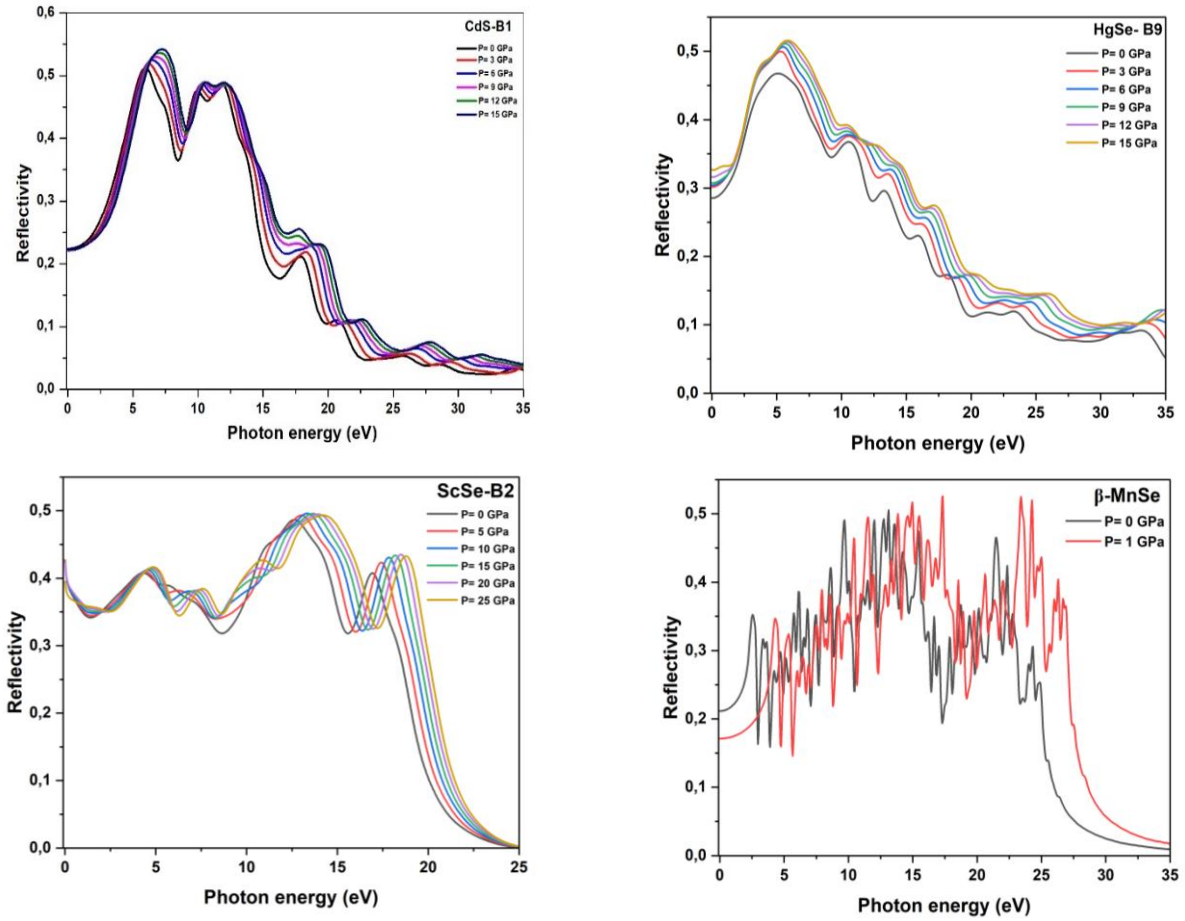

Figure III- 63: Reflectivity spectrum at different pressures of CdSe, HgSe, ScSe and MnSe as a function of photon energy.

III.6.3.4 Absorption

Figure III-64 illustrate the absorption spectra at different pressures as a function of photon energy of CdSe, HgSe, ScSe, and MnSe. Across all compounds, the absorption curves demonstrate virtually identical qualitative patterns, with only modest variances in intensity and peak positions. The absorption coefficient increases progressively with photon energy, demonstrating the availability of higher energy electronic transitions. Moreover, the application of pressure boosts the absorption strength, resulting to greater values of the absorption coefficient. This pressure-induced enhancement is ascribed to the greater overlap of electronic orbitals, which alters the band structure and promotes more efficient interband transitions. At low photon energies, absorption remains feeble until the fundamental absorption threshold is

reached, corresponding to the transition from the valence band maximum to the conduction band minimum. Beyond this threshold, absorption rises quickly with both photon energy and external pressure, demonstrating that compression effectively limits penetration depth and strengthens the material's ability to absorb radiation. These findings imply that the optical absorption of CdSe, HgSe, ScSe, and MnSe can be controlled by hydrostatic pressure, which may be helpful for applications in pressure-sensitive optoelectronic devices, solar energy harvesting, and radiation shielding.

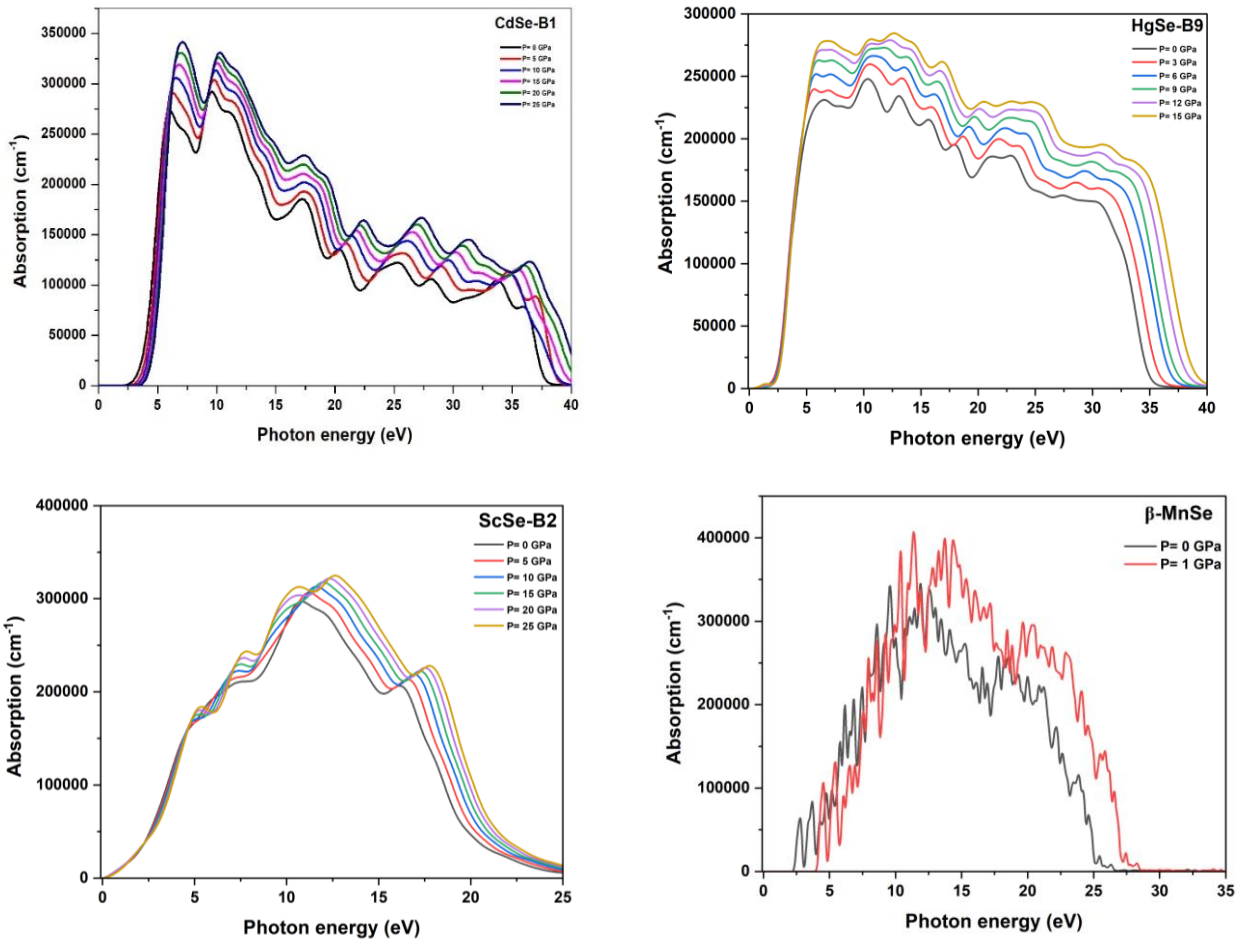

Figure III- 64: The optical absorption coefficient spectrum at different pressures of CdSe, HgSe, ScSe and MnSe as a function of photon energy.

III-6.4 Influence of pressure on elastic constants and mechanical stability

Knowing the elastic constant C_{ij} and obtaining the stiffness coefficient B_{ij} mentioned in equation III-14 for cubic crystal. However, For the trigonal crystal, the elastic stiffness coefficient B_{ij} [92] is defined as follow:

$$\begin{cases} B_{11} = C_{11} - P \\ B_{44} = C_{44} - P \\ B_{12} = C_{12} + P \\ B_{33} = C_{33} - P \\ B_{14} = C_{14} + P \\ B_{13} = C_{13} + P \end{cases} \qquad \text{III} - 17$$

Where P is hydrostatic pressure.

Knowing these elastic constants enabled us to confirm mechanical stability, which requires that the entire elastic constant must be positive and the whole set of elastic constant C_{ij} should satisfy the Born stability criteria. Criteria for a cubic crystal are mentioned in equation III-15, However, Criteria for a trigonal (rhombohedral) crystal [97] defined as follow:

$$\begin{cases} M_1 = B_{11} - |B_{12}| > 0 \\ M_2 = B_{44} > 0 \\ M_4 = B_{33}(B_{11} + B_{12}) - 2B_{13}^2 > 0 \\ M_5 = B_{44}(B_{11} - B_{12}) - 2B_{14}^2 > 0 \end{cases} \qquad \text{III} - 18$$

Figures III-65, III-66, III-67, and III-68 illustrate the variation of elastic constants C_{ij} and the mechanical stability criteria under pressure CdSe, HgSe, ScSe, and MnSe, respectively.

The result presented in the figures indicate that the elastic constants C_{11} and C_{12} for CdSe, ScSe, and MnSe increase linearly with rising pressure. In contrast, C_{44} remains almost constants. Furthermore, for HgSe, all elastic constants (C_{11}, C_{12}, C_{44}, C_{33}, C_{13}, and C_{14}) increase with rising pressure. Importantly, the current results confirm that CdSe in the rock salt structure maintains mechanical stability under pressure, as they meet the required stability criteria. On the contrary, these results reveal that the HgSe in the cinnabar phase, ScSe in the CsCl type structure and MnSe in the zinc-blende structure become mechanically unstable when the pressure exceeds 11.34 GPa, 10.44 GPa, and 4.45 GPa, respectively. Beyond these thresholds, the stability criteria are no longer fulfilled, suggesting a breakdown of mechanical stability under elevated pressure.

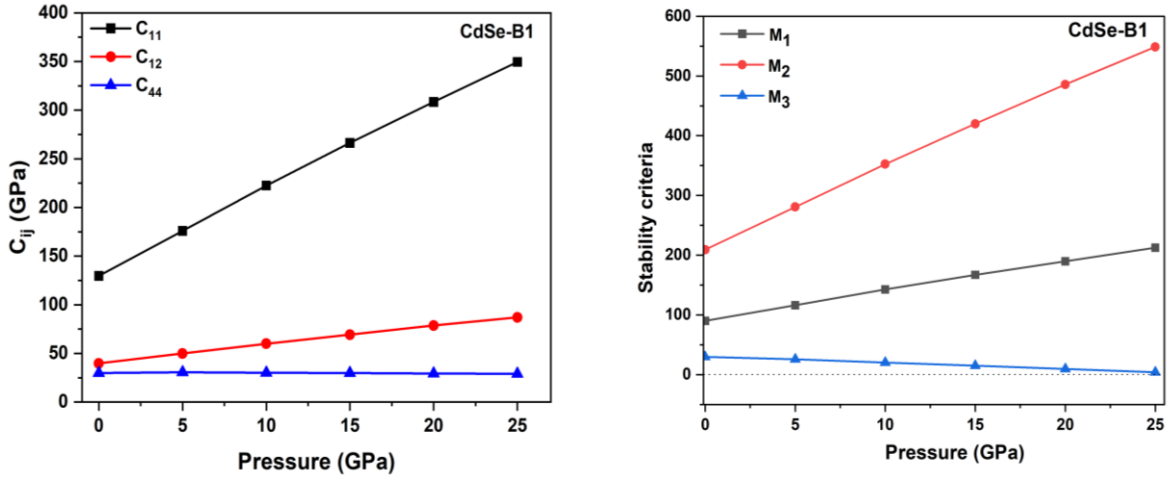

Figure III- 65: Variation of elastic constants C_{ij} and the mechanical stability criteria of CdSe as a function of pressure.

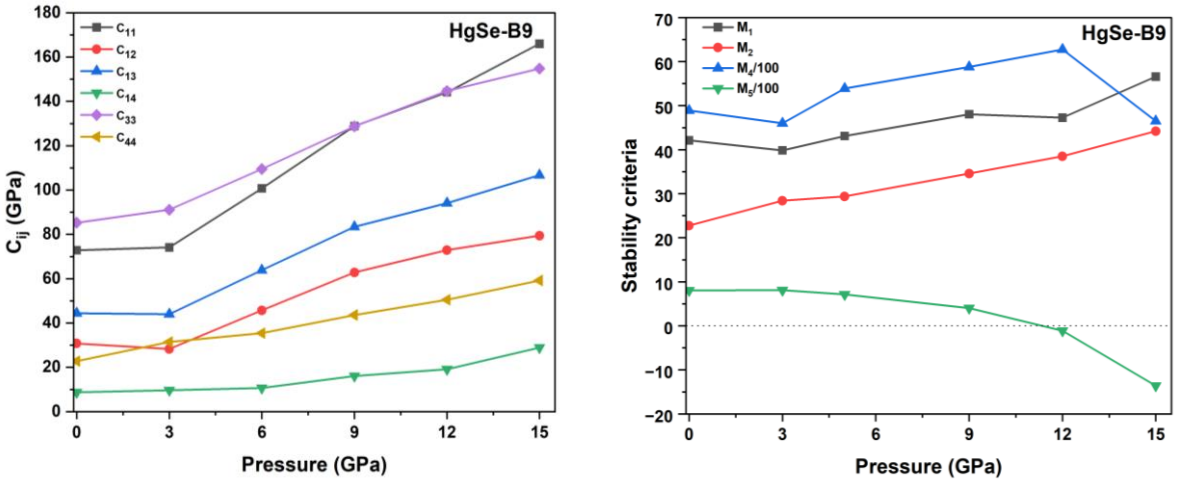

Figure III- 66: Variation of elastic constants C_{ij} and the mechanical stability criteria of HgSe as a function of pressure.

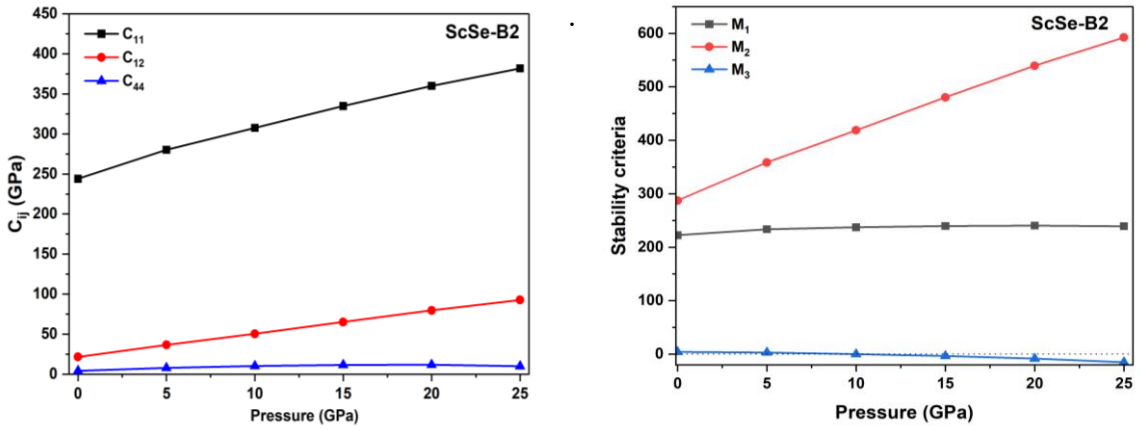

Figure III- 67: Variation of elastic constants C_{ij} and the mechanical stability criteria of ScSe as a function of pressure.

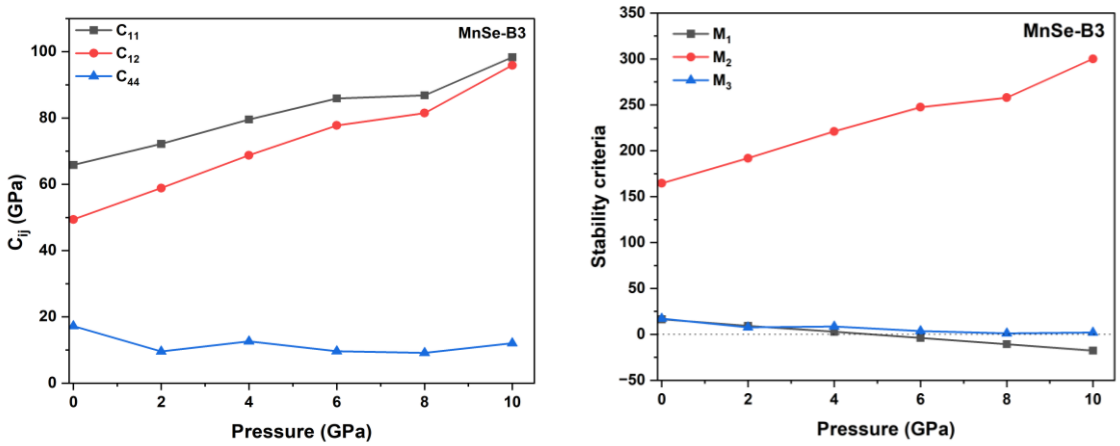

Figure III- 68: Variation of elastic constants C_{ij} and the mechanical stability criteria of MnSe as a function of pressure.

III-6.5 Influence of pressure on thermodynamic properties

III-6.5.1 Bulk modulus (B)

Figure III-69 shows the bulk modulus (B) as a function of temperature at different pressures of CdSe, HgSe, ScSe and MnSe. These results show that B decreases with increasing temperature for HgSe and ScSe. This observation suggests the potential stability of and ScSe under these pressure and temperature conditions. In contrast, for CdSe and MnSe, B decreases with temperature until pressure 15 GPa and 2 GPa for CdSe and MnSe, respectively. At high-pressures (20 and 25 GPa) for CdSe and (4, 6, 8, and 10 GPa) for MnSe, B begins to increase with temperature. This behavior suggests possible phase instabilities of CdSe and under these specific pressure and temperature conditions.

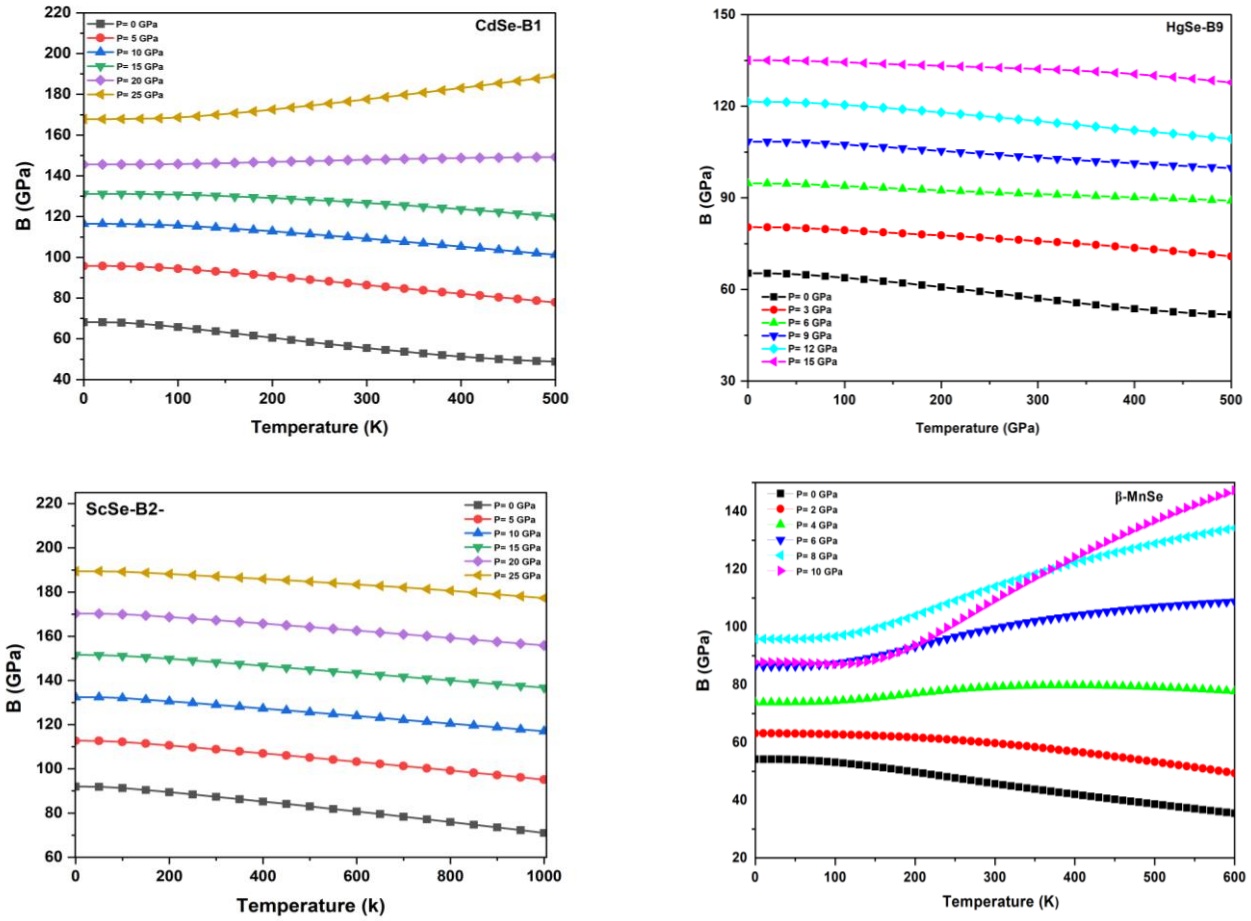

Figure III- 69: Bulk modulus (B) variation at different pressures of CdSe, HgSe, ScSe and MnSe as a function of temperature.

III-6.5.2 Coefficient of thermal expansion

Figures III-70 illustrates the variation of the thermal expansion coefficient (α) as a function of temperature at different pressures for CdSe, HgSe, ScSe and MnSe. For HgSe , and ScSe, α demonstrates a monotonically increasing trend with increasing temperature, with the coefficient continuing to expand at higher temperatures. This constant result suggests the thermomechanical stability of HgSe and ScSe under these pressures and temperature, Moreover, the overall trend of the thermal expansion curves for HgSe and ScSe is found to be similar. Furthermore, for CdSe and MnSe, α indicates a monotonically increasing with rising temperature up to 15 GPa, and 2 GPa, respectively. However, beyond these pressure ranges, the behavior becomes inconsistent at higher pressure, with α showing a decreasing tendency at high temperatures. This deviation suggests possible structural instabilities of CdSe and MnSe structure under these specific pressure and temperature conditions.

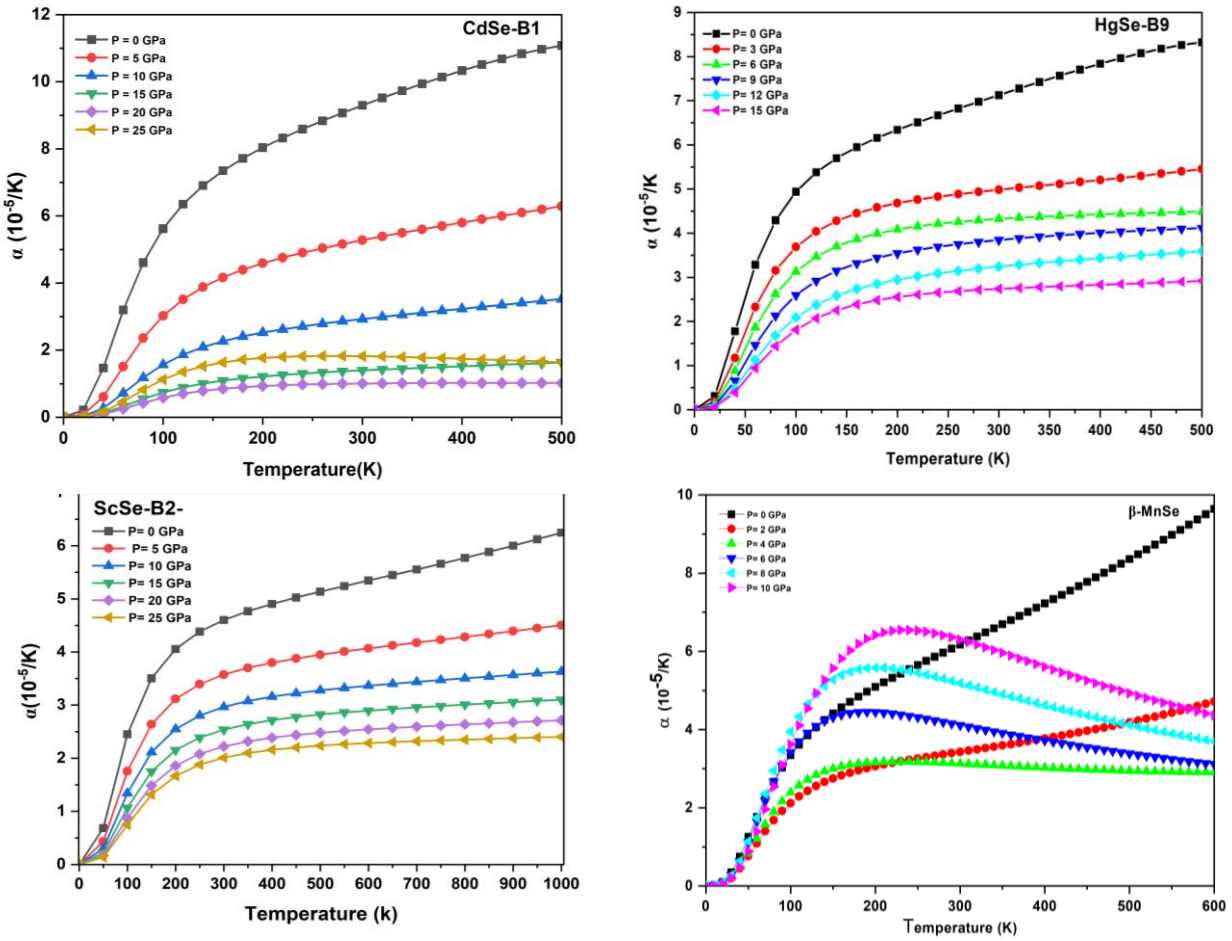

Figure III- 70: Variation of the thermal expansion coefficient (α) at different pressures of CdSe, HgSe, ScSe and MnSe as a function of temperature.

III. 6.5.3 Specific heat capacity C_V

Figure III-71 illustrates the evaluation of the heat capacity at constant volume C_V as a function of temperature at different pressures of CdSe, HgSe, ScSe and MnSe. The results show the heat capacity (C_v), increases exponentially with temperature, in the low temperature regim below 500 K for CdSe and MnSe, 500 K for ScSe, and 300 K for HgSe. At higher temperatures, At higher temperatures, the heat capacity gradually saturates and approaches the Dulong–Petit limit (Cv=3nR) for CdSe, HgSe, ScSe, and MnSe. This convergence confirms the expected classical behavior of lattice vibrations at elevated temperatures for CdSe, HgSe, ScSe, and MnSe.

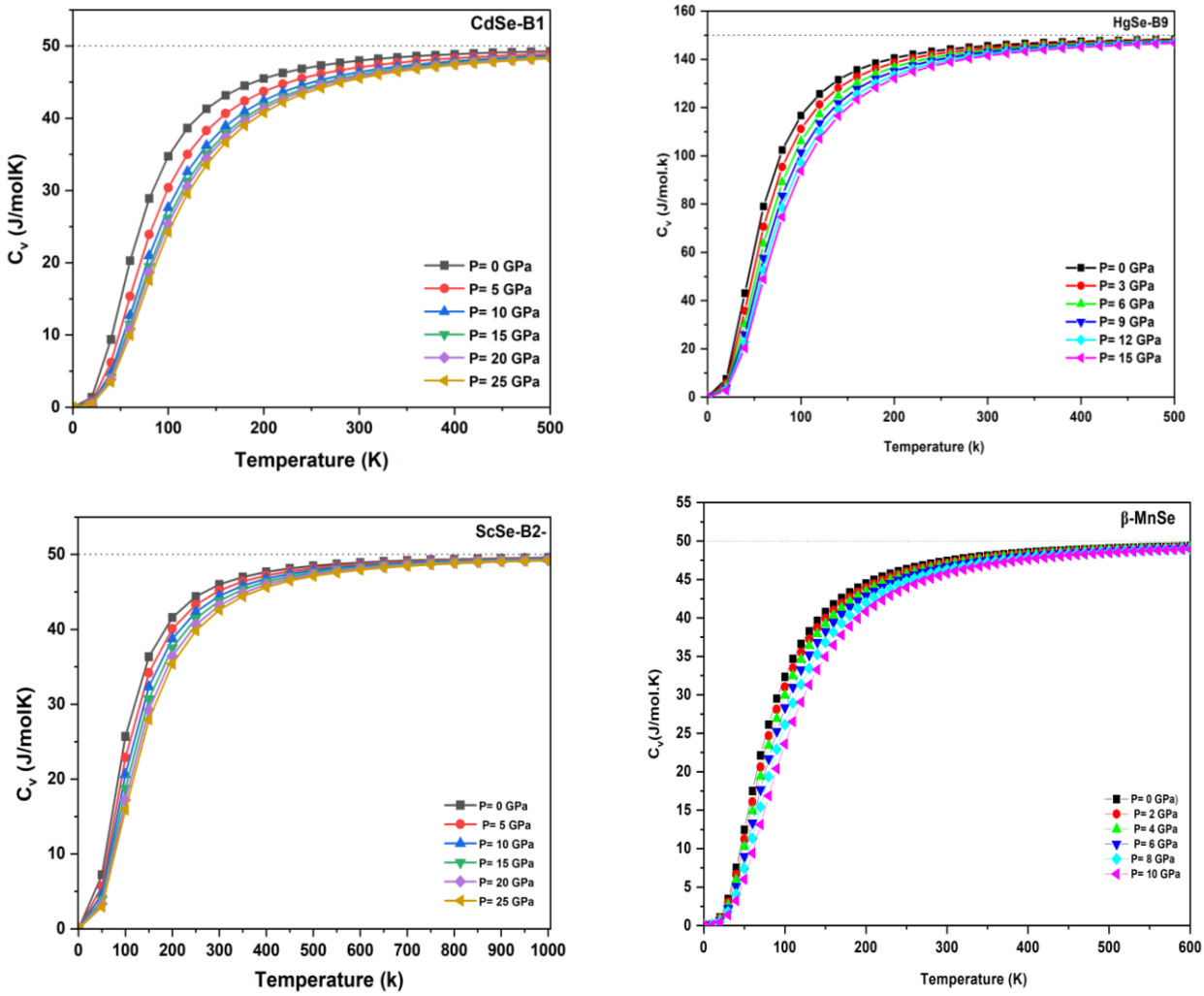

Figure III- 71: Variation of the heat capacity at constant volume C_V at different pressures of CdSe, HgSe, ScSe and MnSe as a function of temperature.

References

[1] A. L. Edwards and H. G. Drickamer, Phys. Rev. **122**, 1149 (1961).

[2] R. J. Nelmes and M. I. McMahon, in *Semiconductors and Semimetals*, Vol. 54 (Elsevier, 1998), pp. 145–246.

[3] M. Von Truchseß, A. Pfeuffer-Jeschke, C. R. Becker, G. Landwehr, and E. Batke, Phys. Rev. B **61**, 1666 (2000).

[4] F. El Haj Hassan, B. Al Shafaay, H. Meradji, S. Ghemid, H. Belkhir, and M. Korek, Phys. Scr. **84**, 065601 (2011).

[5] J. P. Dismukes and J. G. White, Inorg. Chem. **3**, 1220 (1964).

[6] F. Hulliger and G. W. Hull, Solid State Commun. **8**, 1379 (1970).

[7] A. Maachou, H. Aboura, B. Amrani, R. Khenata, S. Bin Omran, and D. Varshney, Comput. Mater. Sci. **50**, 3123 (2011).

[8] P. Bhardwaj and S. Singh, Procedia Comput. Sci. **57**, 160 (2015).

[9] A. A. Ahmad, S. Mahmoud, B. Alshafaay, R. Halabi, and F. El Haj Hassan, Indian J. Phys. **93**, 1129 (2019).

[10] V. Thanigaimani and M. A. Angadi, Thin Solid Films **245**, 146 (1994).

[11] M. D. Segall, P. J. D. Lindan, M. J. Probert, C. J. Pickard, P. J. Hasnip, S. J. Clark, and M. C. Payne, J. Phys. Condens. Matter **14**, 2717 (2002).

[12] J. P. Perdew, A. Ruzsinszky, G. I. Csonka, O. A. Vydrov, G. E. Scuseria, L. A. Constantin, X. Zhou, and K. Burke, Phys. Rev. Lett. **100**, 136406 (2008).

[13] A. D. Becke, J. Chem. Phys. **98**, 5648 (1993).

[14] F. D. Murnaghan, Proc. Natl. Acad. Sci. **30**, 244 (1944).

[15] A. Otero-de-la-Roza, D. Abbasi-Pérez, and V. Luaña, Comput. Phys. Commun. **182**, 2232 (2011).

[16] Landolt-Börnstein, O. Madelung, M. Schulz, and H. Weiss, *Semiconductors* (Springer Verlag, Berlin Heidelberg New York, 1982).

[17] A. Svane, P. Strange, W. M. Temmerman, Z. Szotek, H. Winter, and L. Petit, Phys. Status Solidi B **223**, 105 (2001).

[18] L. Guo, S. Zhang, W. Feng, G. Hu, and W. Li, J. Alloys Compd. **579**, 583 (2013).

[19] O. Madelung, U. Rössler, and M. Schulz, editors , *II-VI and I-VII Compounds; Semimagnetic Compounds*, Vol. 41B (Springer-Verlag, Berlin/Heidelberg, 1999).

[20] S. Adachi, *Properties of Semiconductor Alloys: Group-IV, III–V and II–VI Semiconductors*, 1st ed. (Wiley, 2009).

[21] B. Benabdelkrim, T. Ghaitaoui, B. Amrani, A. E. Ghaitaoui, and I. Arbaoui, Phys. Solid State **66**, 139 (2024).

[22] I. Duz, S. Ozdemir Kart, I. Erdem, and V. Kuzucu, Curr. Appl. Phys. **18**, 424 (2018).

[23] Pavas, N. Munjal, A. D. Majumdar, U. Kamboj, and A. Kumar, J. Phys. Conf. Ser. **1531**, 012047 (2020).

[24] J. B. C. Efrem D'Sa, P. A. Bhobe, K. R. Priolkar, A. Das, P. S. R. Krishna, P. R. Sarode, and R. B. Prabhu, Pramana **63**, 227 (2004).

[25] W. Zhou, S. Wu, and S. Li, J. Magn. Magn. Mater. **395**, 166 (2015).

[26] P. Amiri, S. J. Hashemifar, and H. Akbarzadeh, Phys. Rev. B **83**, 165424 (2011).

[27] R. Ksouri, R. Maizi, I. Djaghout, A.-G. Boudjahem, and M. Derdare, Russ. J. Inorg. Chem. **67**, 193 (2022).

[28] N. A. Noor and A. Shaukat, Int. J. Mod. Phys. B **26**, 1250168 (2012).

[29] J. N. Wickham, A. B. Herhold, and A. P. Alivisatos, Phys. Rev. Lett. **84**, 923 (2000).

[30] N. Benkhettou, D. Rached, B. Soudini, and M. Driz, Phys. Status Solidi B **241**, 101 (2004).

[31] B. Al Shafaay, F. El Haj Hassan, and M. Korek, Comput. Mater. Sci. **83**, 107 (2014).

[32] Y. Zhao, W. Shi, Q. Zhang, J. Wang, J. Ma, and T. Gao, Adv. Condens. Matter Phys. **2024**, 5538895 (2024).

[33] A. M. Ali and M. J. Mohammed, Iraqi J. Phys. **23**, 40 (2025).

[34] D. Christen, *Molecular Constants Mostly from Microwave, Molecular Beam, and Sub-Doppler Laser Spectroscopy: Paramagnetic Diatomic Molecules (Radicals), Part 2*, Vol. 29E2 (Springer Berlin Heidelberg, Berlin, Heidelberg, 2021).

[35] P. Bhardwaj and S. Singh, Phys. Solid State **58**, 2081 (2016).

[36] C. Wang, L. Gao, R. Wang, B. Ming, G. Guo, and H. Yan, Phys. Lett. A **384**, 126373 (2020).

[37] D. Shrivastava and S. P. Sanyal, Comput. Condens. Matter **21**, e00418 (2019).

[38] S. K. Yadav, S. Dahal, R. Khadka, B. Guragain, P. Pokharel, P. Oli, and D. Adhikari, Eng. Rep. **7**, e13115 (2025).

[39] A. H. Reshak, I. V. Kityk, R. Khenata, and S. Auluck, J. Alloys Compd. **509**, 6737 (2011).

[40] E. Deligoz, K. Colakoglu, and Y. Ciftci, Phys. B Condens. Matter **373**, 124 (2006).

[41] K. Ichino, Y. Wu, Y. Kawakami, S. Fujita, and S. Fujita, J. Cryst. Growth **117**, 527 (1992).

[42] W. H. Strehlow and E. L. Cook, J. Phys. Chem. Ref. Data **2**, 163 (1973).

[43] N. E. H. Habibes, A. Boukortt, S. Meskine, A. Benbedra, Y. Mamouni, and H. Bennacer, ECS J. Solid State Sci. Technol. **13**, 013013 (2024).

[44] B. Al Shafaay, F. El Haj Hassan, and M. Korek, Comput. Mater. Sci. **83**, 107 (2014).

[45] A. Khaldi, N. Bouarissa, H. Ghodbane, and L. Tabourot, Phys. B Condens. Matter **553**, 6 (2019).

[46] C. Loschen, J. Carrasco, K. M. Neyman, and F. Illas, Phys. Rev. B **75**, 035115 (2007).

[47] I. Khan, I. Ahmad, H. A. R. Aliabad, and M. Maqbool, .

[48] M. Zafar, M. Shakil, S. Ahmed, M. Raza-ur-rehman Hashmi, M. A. Choudhary, and Naeem-ur-Rehman, Sol. Energy **158**, 63 (2017).

[49] F. Virot, R. Hayn, M. Richter, and J. Van Den Brink, Phys. Rev. Lett. **111**, 146803 (2013).

[50] N. Ullah, G. Murtaza, R. Khenata, K. M. Wong, and Z. A. Alahmed, Phase Transit. **87**, 571 (2014).

[51] Md. A. Rahman, Md. Z. Rahaman, and Md. A. Rahman, Int. J. Mod. Phys. B **30**, 1650199 (2016).

[52] H. Ehrenreich and M. H. Cohen, Phys. Rev. **115**, 786 (1959).

[53] M. W. Lee and H. D. Drew, Solid State Commun. **62**, 825 (1987).

[54] B. Bonello and B. Fernandez, J. Phys. Chem. Solids **54**, 209 (1993).

[55] A. Manabe, A. Mitsuishi, and H. Yoshinaga, Jpn. J. Appl. Phys. **6**, 593 (1967).

[56] E. Burstein, M. H. Brodsky, and G. Lucovsky, Int. J. Quantum Chem. **1**, 759 (2009).

[57] N. A. Noor, W. Tahir, F. Aslam, and A. Shaukat, Phys. B Condens. Matter **407**, 943 (2012).

[58] L. Hannachi and N. Bouarissa, Phys. B Condens. Matter **404**, 3650 (2009).

[59] S. Chanda, M. Debbarma, D. Ghosh, B. Debnath, and S. Chattopadhyaya, Bull. Mater. Sci. **45**, 34 (2022).

[60] A. Dal Corso, S. Baroni, R. Resta, and S. De Gironcoli, Phys. Rev. B **47**, 3588 (1993).

[61] M. N. Secuk., M. Aycibin, B. Erdinc, S. E. Gulebaglan, E. K. Dogan, and H. Akkus, **4(1)**, 13 (2014).

[62] F. Boutaiba, A. Zaoui, and M. Ferhat, Superlattices Microstruct. **46**, 823 (2009).

[63] F. Kootstra, P. L. De Boeij, and J. G. Snijders, Phys. Rev. B **62**, 7071 (2000).

[64] N. M. Ravindra, P. Ganapathy, and J. Choi, Infrared Phys. Technol. **50**, 21 (2007).

[65] Y. V. Vorobiev, P. P. Horley, J. Hernández-Borja, H. E. Esparza-Ponce, R. Ramírez-Bon, P. Vorobiev, C. Pérez, and J. González-Hernández, Nanoscale Res. Lett. **7**, 483 (2012).

[66] O. T. Bruhns, *Advanced Mechanics of Solids* (Springer Berlin Heidelberg, Berlin, Heidelberg, 2003).

[67] A. F. Wright, J. Appl. Phys. **82**, 2833 (1997).

[68] B. Mayer, H. Anton, E. Bott, M. Methfessel, J. Sticht, J. Harris, and P. C. Schmidt, Intermetallics **11**, 23 (2003).

[69] Y. O. Ciftci, K. Çolakoglu, E. Deligoz, and H. Ozisik, Mater. Chem. Phys. **108**, 120 (2008).

[70] D. G. Pettifor, Mater. Sci. Technol. **8**, 345 (1992).

[71] S. F. Pugh, Lond. Edinb. Dublin Philos. Mag. J. Sci. **45**, 823 (1954).

[72] S. Ouendadji, S. Ghemid, H. Meradji, and F. E. H. Hassan, Comput. Mater. Sci. **48**, 206 (2010).

[73] F. Benkabou, H. Aourag, and M. Certier, Mater. Chem. Phys. **66**, 10 (2000).

[74] A. Lehoczky, D. A. Nelson, and C. R. Whitsett, Phys. Rev. **188**, 1069 (1969).

[75] P. J. Ford, A. J. Miller, G. A. Saunders, Y. K. Yogurtcu, J. K. Furdyna, and M. Jaczynski, J. Phys. C Solid State Phys. **15**, 657 (1982).

[76] M. Abu-Jafar, R. Dayton-Oxland, R. Jaradat, A. A. Mousa, and R. Khenata, Phase Transit. **93**, 773 (2020).

[77] I. N. Frantsevich, F. F. Voronov, and S. A. Bakuta, *Handbook on Elastic Constants and Moduli of Elasticity for Metals and Nonmetals* (Naukova Dumka, Kiev, 1982).

[78] O. N. Senkov and D. B. Miracle, Sci. Rep. **11**, 4531 (2021).

[79] G. Grimvall, B. Magyari-Köpe, V. Ozoliņš, and K. A. Persson, Rev. Mod. Phys. **84**, 945 (2012).

[80] D. C. Wallace, Phys. Rev. **162**, 776 (1967).

[81] S. Chanda, M. Debbarma, D. Ghosh, B. Debnath, and S. Chattopadhyaya, Bull. Mater. Sci. **45**, 34 (2022).

[82] I. Duz, S. Ozdemir Kart, I. Erdem, and V. Kuzucu, Curr. Appl. Phys. **18**, 424 (2018).

[83] W. C. Yu and P. J. Gielisse, Mater. Res. Bull. **6**, 621 (1971).

[84] N. Benkhettou, D. Rached, B. Soudini, and M. Driz, Phys. Status Solidi B **241**, 101 (2004).

[85] K.-U. Gawlik, L. Kipp, M. Skibowski, N. Orłowski, and R. Manzke, Phys. Rev. Lett. **78**, 3165 (1997).

[86] M. I. McMahon, R. J. Nelmes, H. Liu, and S. A. Belmonte, Phys. Rev. Lett. **77**, 1781 (1996).

[87] N. Kumar, S. Kesari, S. N. Krylova, R. Rao, N. V. Surovtsev, D. V. Ishchenko, S. V. Pryanichnikov, T. E. Govorkova, S. B. Bobin, A. T. Lonchakov, V. A. Golyashov, and O. E. Tereshchenko, J. Phys. Chem. Solids **207**, 112977 (2025).

[88] S. Biering and P. Schwerdtfeger, J. Chem. Phys. **137**, 034705 (2012).

[89] S. Radescu, A. Mujica, and R. J. Needs, Phys. Rev. B **80**, 144110 (2009).

[90] W. Lee and A. M. Smith, Nat. Synth. **3**, 1243 (2024).

[91] M. I. McMahon, N. G. Wright, D. R. Allan, and R. J. Nelmes, Phys. Rev. B **53**, 2163 (1996).

[92] G. V. Sin$rquot$ko and N. A. Smirnov, J. Phys. Condens. Matter **14**, 6989 (2002).

[93] R. M. Murray, B. C. Forbes, and R. D. Heyding, Can. J. Chem. **50**, 4059 (1972).

[94] H. J. Hou, J. W. Yang, F. Hu, S. R. Zhang, and S. X. Yang, (n.d.).

[95] Y. Wu, Y. Duan, X. Wang, M. Peng, L. Shen, and H. Qi, Mater. Today Commun. **33**, 104651 (2022).

[96] E. Rabani, J. Chem. Phys. **116**, 258 (2002).

[97] Gusev A. I. and Sadovnikov S. I., Phys. Solid State **64**, 659 (2022).

General Conclusion

This work aimed to investigate the structural, electronic, optical, elastic, vibrational, and thermodynamic properties of transition metal Selenides, specifically, CdSe, HgSe, ScSe and MnSe under zero and hydrostatic pressures. Various crystal structures were considered, including zinc-blende (B3) and rock-salt (B1) for CdSe, zinc-blende (B3) and cinnabar (trigonal) (B9) for HgSe, NaCl (B1) and CsCl (B2) for ScSe, and zinc-blende (β) and rock-salt (α) for MnSe. The study employed ab initio calculation methods with pseudopotentials and a plane-wave basis, based on density functional theory (DFT), as implemented in the CASTEP code. The exchange-correlation effects were treated within the frameworks of the generalized gradient approximation (GGA) and the B3LYP hybrid functional. The Gibbs2 code, based on Debye's quasi-harmonic model, was used to investigate the thermodynamic properties.

The obtained structural parameters including lattice constants, bulk modulus, and its pressure derivative are in excellent agreement with available experimental and theoretical results, confirming the reliability of the computational framework. The results show that the zinc-blende phase is the most stable configuration for CdSe and HgSe, while the rock-salt phase is the most stable for MnSe and ScSe. Furthermore, all compounds exhibit a decrease in lattice parameters with increasing pressure, as expected under compression.

The electronic properties of CdSe, HgSe, MnSe, and ScSe were examined using both GGA-PBEsol approximations and the hybrid functional B3LYP. The analysis of their electronic structure reveals varied behaviors among the materials studied. CdSe in the B3 phase shows a direct wide band gap, in contrast, the B1 phase of CdSe shows an indirect band gap, while HgSe in the zinc-blende structure has a small direct band gap and shifts to an indirect band gap in the cinnabar phase. ScSe in both NaCl- and CsCl-type structures exhibits metallic character, with no band gap observed. Conversely, Mnse demonstrates semiconducting and spin-polarized traits in both zinc-blende and rock-salt phases, confirming its magnetic and spintronic potential. Pressure-dependent investigations further show that the band gaps of CdSe and HgSe increase linearly with pressure, whereas MnSe presents complex, spin-dependent trends. Overall, the electronic findings align with experimental results and prior theoretical studies.

The optical properties, derived from the dielectric function, refractive index, absorption coefficient, and reflectivity spectra, confirm the semiconducting nature of CdSe and HgSe and the metallic character of ScSe. MnSe exhibits spin-dependent optical responses, emphasising its potential in spintronic and magneto-optical devices. The optical absorption edges shift

towards higher energies under pressure, correlating well with the band gap widening observed in electronic calculations.

The computed elastic constants including the bulk modulus (B), shear modulus (G), and Young's modulus (E) for CdSe, HgSe, ScSe, and MnSe are in good agreement with both experimental data and previous ab initio studies, validating the reliability of the present computational framework.

The ductility and brittleness of these compounds were further examined using Pugh's ratio (B/G), Poisson's ratio (ν), and Cauchy pressure (C_{12}–C_{44}). The B/G ratios obtained for CdSe, HgSe, MnSe, and ScSe in the CsCl (B2) phase exceed the critical value of 1.75, confirming their ductile behavior. These results align with the findings from both the Pettifor and Poisson criteria, reinforcing the classification of CdSe, HgSe, MnSe, and ScSe in the CsCl (B2) phase as ductile. Interestingly, for ScSe in the NaCl (B1) phase, the calculated Cauchy pressure is slightly negative, indicating the presence of directional covalent bonding. This suggests potential localized brittle tendencies along specific crystallographic planes, even though the overall Pugh and Poisson criteria identify ScSe as globally ductile.

The current results also confirm that CdSe (B1 and B3), HgSe (B3), and MnSe (α) maintain mechanical stability under pressure, satisfying all Born stability criteria. In contrast, HgSe in the cinnabar phase (B9), ScSe in both NaCl (B1) and CsCl (B2) structures, and MnSe in the zinc-blende (β) configuration exhibit mechanical instability beyond certain pressure thresholds. Specifically, instability occurs above approximately ~11.34 GPa for HgSe (B9), ~33.91 GPa for ScSe (B1), ~10.44 GPa for ScSe (B2), and ~4.45 GPa for MnSe (β). Beyond these critical pressures, the Born stability conditions are violated, signaling a loss of mechanical stability under increasing pressure.

The dynamical properties of CdSe, HgSe, and ScSe were examined through phonon dispersion calculations. The findings show that no imaginary phonon frequencies occur throughout the Brillouin zone for both structures of CdSe and for HgSe and ScSe in the NaCl (B1) phase. This verifies that the B1 and B3 structures of CdSe, the B3 and B9 structures of HgSe, and the NaCl (B1) structure of ScSe are dynamically stable at zero pressure and under applied pressure. Conversely, the phonon dispersion curves of ScSe in the CsCl (B2) structure display negative frequencies, indicating that this phase is dynamically unstable.

The thermodynamic properties of all compounds were further analyzed using the Gibbs2 code within the quasi-harmonic Debye model. The results show a monotonic increase in the thermal expansion coefficient (α) with rising temperature. This trend becomes more pronounced at high temperatures for CdSe (B3), HgSe (B9), and ScSe (B2), suggesting potential thermodynamic stability of these phases under the studied pressure and temperature conditions. Conversely, CdSe (B1), HgSe (B3), ScSe (B1), and MnSe (B1 and B3) exhibit a similar increasing trend only up to specific critical pressures approximately 10 GPa for CdSe, 1 GPa for HgSe, 20 GPa for ScSe, and 2 GPa for MnSe beyond which instability may occur.

The bulk modulus (B) decreases with increasing temperature for CdSe (B3), HgSe (B9), and ScSe (B2), further supporting their structural stability under the investigated conditions. In contrast, CdSe (B1), HgSe (B3), ScSe (B1), and MnSe (B1 and B3) exhibit an initial decrease in bulk modulus with temperature up to their respective critical pressures, followed by an anomalous increase at higher temperatures and pressures, suggesting possible phase instabilities in these configurations.

Finally, the heat capacity at constant volume (Cv) shows similar temperature-dependent behavior across all studied compounds CdSe, HgSe, ScSe, and MnSe indicating consistent thermodynamic response trends within this family of materials.

Abstract

This work involves a theoretical study using the ab initio method to examine the structural, elastic, electronic, optical, dynamic, and thermodynamic properties of CdSe and MnSe in both zinc-blende and rock-salt structures, HgSe in zinc-blende and cinnabar phases, and ScSe in both NaCl and CsCl types at zero and under hydrostatic pressure. We used first-principles pseudopotential plane-wave calculations, as implemented in the CASTEP code. The generalized gradient approximation (GGA-PBEsol) was employed for the exchange-correlation (XC) potential to calculate structural properties. The results obtained are consistent with available experimental and theoretical data. The B3LYP hybrid functional was used to estimate the electronic structure. Thermodynamic properties of the materials were determined using the Gibbs2 code. The results of this study indicate that CdSe and HgSe are stable in the zinc-blende structure; however, MnSe and ScSe are stable in the rock-salt phase. We provide a detailed analysis of how key optical properties such as the dielectric function, refractive index, and reflectivity change with energy, and we discuss what these trends imply. Additionally, our work clarifies how several thermodynamic variables, like the bulk modulus, heat capacity, and thermal expansion coefficient, depend on temperature and pressure, offering forecasts and in-depth discussion. Moreover, the electronic properties show that both CdSe and HgSe have a direct bandgap in the zinc-blende structure; however, both GGA and B3LYP approximations clearly show the existence of an indirect bandgap. Our calculations also reveal that the ScSe compound is metallic. Conversely, the bandgap calculation for MnSe indicates a semiconducting nature in both rock-salt and zinc-blende phases for both spin polarization channels.

Key words: pseudo potential, structural properties, electronic properties, elastic properties, dynamic properties, optical properties, Transition metal selenides.

Résumé

Le travail consiste en une étude théorique utilisant la méthode ab initio pour examiner les propriétés structurelles, élastiques, électroniques, optiques, dynamiques et thermodynamiques du CdSe et du MnSe dans les structures de zinc blende et de sel gemme, du HgSe dans les phases de zinc blende et de cinabre, et du ScSe à pression zéro et sous pression hydrostatique. Nous avons utilisé les premiers principes des ondes planes pseudo-potentielles, comme implémentés dans le code CASTEP. L'approximation du gradient généralisé (GGA-PBEsol) a été utilisée pour le potentiel d'échange-corrélation (XC) afin de calculer les propriétés structurelles. Les résultats obtenus sont conformes aux données expérimentales et théoriques disponibles. La fonctionnelle hybride B3LYP a été utilisée pour estimer la structure électronique. Les propriétés thermodynamiques des matériaux ont été déterminées à l'aide du code Gibbs2.

Les résultats de cette étude indiquent que le CdSe et le HgSe sont stables dans le mélange de zinc ; cependant, les structures de MnSe et ScSe sont stables dans la structure du sel gemme. Nous fournissons une analyse détaillée de la façon dont les propriétés optiques clés telles que la fonction diélectrique, l'indice de réfraction et la réflectivité changent avec l'énergie, et nous discutons de ce que signifient ces tendances. De plus, notre travail clarifie comment plusieurs variables thermodynamiques, comme le module d'élasticité, la capacité thermique et le coefficient de dilatation thermique, dépendent de la température et de la pression, offrant des prévisions et une discussion approfondie. En outre, les propriétés électroniques montrent que le CdSe et le HgSe ont tous deux une bande interdite directe dans la structure du blende de zinc ; cependant, l'approximation GGA et B3LYP montrent clairement l'existence d'une bande interdite indirecte. De plus, nos calculs montrent clairement que le composé ScSe est métallique. Inversement, notre calcul de la bande interdite de MnSe met en évidence une nature semi-conductrice dans les phases du sel gemme et de la blende de zinc pour les deux canaux de polarisation de spin.

Mots Clés : pseudo potentiel, propriétés structurelles, propriétés électroniques, propriétés élastiques, propriétés dynamiques, propriétés optiques, selenides de métaux de transition.

ملخص:

يتضمن العمل دراسة نظرية باستخدام الطريقة الأولية لفحص الخواص الهيكلية والمرونية والإلكترونية والبصرية والديناميكية والديناميكية الحرارية لـ CdSe وMnSe في كل من هياكل مزيج الزنك والملح الصخري، وHgSe في مرحلتي مزيج الزنك والزنجفر، وScSe عند ضغط صفر وتحت الضغط الهيدروستاتيكي. استخدمنا المبادئ الأولى للموجات المستوية مع تقريب الكمون الزائف ، كما تم تنفيذها في كود CASTEP. تم استخدام تقريب التدرج المعمم (GGA-PBEsol) ذو كمون الارتباط التبادلي (XC) لحساب الخصائص الهيكلية. وتتوافق النتائج التي تم الحصول عليها مع البيانات التجريبية والنظرية المتاحة. تم استخدام الدالية الهجينة B3LYP لحساب البنية الإلكترونية. تم وصف الخواص الديناميكية الحرارية للمواد باستخدام كود Gibbs2.

تشير نتائج هذه الدراسة إلى أن CdSe وHgSe مستقران في مزيج الزنك؛ ومع ذلك، فإن هياكل MnSe وScSe مستقرة في بنية الملح الصخري. قدمنا تحليلاً مفصلاً لكيفية تغير الخصائص البصرية الرئيسية مثل وظيفة العزل الكهربائي، ومعامل الانكسار، والانعكاسية مع الطاقة، وناقشنا ما تعنيه هذه الاتجاهات. بالإضافة إلى ذلك، يوضح عملنا كيف تعتمد العديد من المتغيرات الديناميكية الحرارية، مثل معامل الحجم، والسعة الحرارية، ومعامل التمدد الحراري، على درجة الحرارة والضغط، مما يوفر توقعات ومناقشة متعمقة. علاوة على ذلك، تظهر الخصائص الإلكترونية أن كلا من CdSe وHgSe لهما فجوة نطاق مباشرة في بنية مزيج الزنك؛ ومع ذلك، يُظهر تقريب كل من GGA وB3LYP بوضوح وجود فجوة نطاق غير مباشرة. بالإضافة إلى ذلك، تظهر حساباتنا بوضوح أن مركب ScSe معدني. على العكس من ذلك، فإن حسابنا لفجوة نطاق MnSe يدل على طبيعة شبه موصلة في كل من مرحلتي الملح الصخري ومزيج الزنك لكلا قناتي اللف الذاتي.

الكلمات المفتاحية: الكمون الزائف ، الخصائص الهيكلية، الخصائص الإلكترونية، الخصائص المرونية، الخصائص الديناميكية، الخصائص البصرية، سيلينيدات المعادن الانتقالية.